Eindhoven University of Technology

MASTER

Analysis and optimization of large patch-antenna arrays

Dirks, R.

Award date:
2005

Link to publication

Disclaimer
This document contains a student thesis (bachelor's or master's), as authored by a student at Eindhoven University of Technology. Student theses are made available in the TU/e repository upon obtaining the required degree. The grade received is not published on the document as presented in the repository. The required complexity or quality of research of student theses may vary by program, and the required minimum study period may vary in duration.

General rights
Copyright and moral rights for the publications made accessible in the public portal are retained by the authors and/or other copyright owners and it is a condition of accessing publications that users recognise and abide by the legal requirements associated with these rights.

- Users may download and print one copy of any publication from the public portal for the purpose of private study or research.
- You may not further distribute the material or use it for any profit-making activity or commercial gain

TU/e technische universiteit eindhoven

Faculty of Electrical Engineering
Division Telecommunication Technology and Electromagnetics
Chair of Electromagnetics

Analysis and Optimization of Large Patch-Antenna Arrays

by R. Dirks

EM-2-05

October, 2005

Report of Master's project performed at
TU/e, Electromagnetics Section

Supervisor:
Dr.ir. M.C. van Beurden (TU/e)
Prof.dr. A.G. Tijhuis (TU/e)

Copyright © 2002
All rights reserved.
No part of this report may be reproduced by any means, or transmitted, or translated into a machine language without the written permission of the Electromagnetics Section, TTE Division, Faculty of Electrical Engineering, Eindhoven University of Technology.

The Faculty of Electrical Engineering of the Eindhoven University of Technology disclaims all responsibility for the contents of traineeship and graduation reports.

Summary

In this report, an infinite-array model is employed to model a large patch-antenna array. Its mathematical formulation employs the symmetries and periodicity of the model, which keep it compact and efficient. Furthermore, a conjugate gradient scheme, viz., CGFFT is employed, which reduces the computational load drastically. When the two are put together a relatively fast simulation tool becomes available, which is used in conjunction with a gradient-based-optimization scheme to make a first attempt in automating the design process of a patch-antenna array or more generally an antenna. The presented results show that the optimization of this relatively simple model already poses quite some challenges. One of those challenges is the existence of (multiple) local optima, which can be partially avoided by choosing the objective function wisely and by employing the periodicity of some of the design parameters. Furthermore, a performance comparison is made between two gradient-based-optimization schemes, viz., NPSOL and L-BFGS-B, where the latter seems to outperform the first for the optimization problems tackled in this report.

Contents

Chapter 1

Introduction

Nowadays wireless applications of all sorts and sizes have become a common occurrence in many modern societies around the globe. The applications, ranging from electronic id-tags, cellular phones, to radar, are in a sense an extension of the human senses. They allow us to detect things under normally difficult or even impossible circumstances for a human. A nice example is the detection and tracking of ships or airplanes under foggy

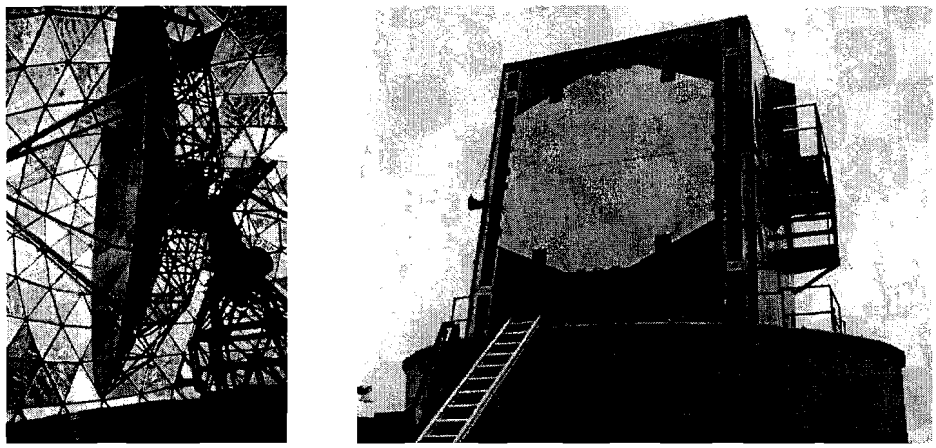

(a) (b)

Figure 1.1: Two antennas of weather-radar systems, in (a) a parabolic reflector antenna of the National Severe Storms Laboratory (NSSL) and in (b) a phased-array antenna of the National Oceanic & Atmospheric Administration (NOAA). Source: www.photolib.noaa.gov

conditions or even beyond the horizon, made possible by the introduction of sophisticated radar systems. For each application a specific set of design specifications can be formulated, which includes things like size, weight, cost, and various application-dependent demands. This set will indicate a ballpark for the design constraints for the radiating element of the wireless application, the antenna. These constraints are often contradic-

tory, i.e., improving on one property deteriorates other properties. Given a number of design constraints achieving the best possible solution can be a real challenge. This is easily illustrated, by considering the design constraints of a radar system, as depicted in Figure 1.1, which involves (among many others) high directivity, and a short scan time, for the lowest achievable manufacturing cost. The high directivity could be achieved by enlarging the effective surface area of the antenna. Traditionally this would mean a larger parabolic reflector, but increasing its size and consequently the weight will make it a lot more difficult to mechanically scan its surroundings in a short time. Note that the word 'difficult' is in this case synonymous with 'expensive', and consequently the costs will increase as well. The introduction of phased-array antennas made it possible to scan electronically, which decreases the 'long' scan times dramatically. The downside however is a dramatic increase in complexity of the overal system and in cost.

However, finding an appropriate solution for the entire radar system is beyond the scope of this report. Instead the report will only consider the radiating elements of the phased-array-radar system, which is in this case a patch-antenna array. A schematic 3D view of a patch-antenna array is depicted in Figure 1.2.

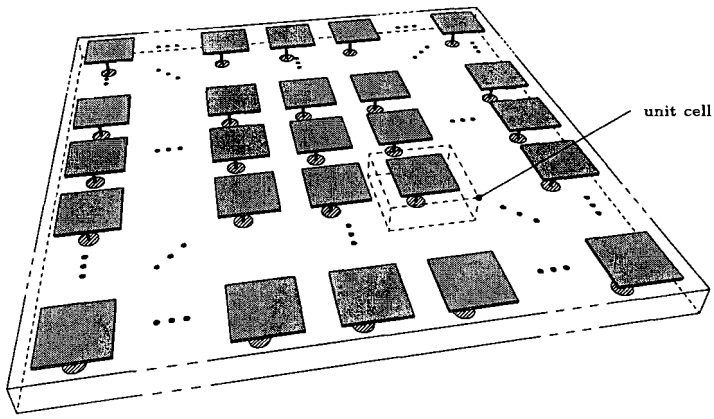

Figure 1.2: A schematic 3D view of a large patch-antenna array.

A large portion of the design process of an antenna is occupied by the optimization of its characteristic behavior, where optimization means trying to find the optimal parameters (length and width of the patch, material properties, etc.) for which the given design constraints are met. Traditionally this would mean performing some calculations, while employing a simple model, constructing a prototype, measuring its characteristic behavior, determining the deviation from the goal, adjusting the parameters and start all over again by constructing another prototype and so on and so forth, knowing that it will take at least 10 or 20 runs before one could talk about reaching some kind of optimum. Needless to say, the optimization process can be both a time and money con-

suming part of the design process. A first step in automating the optimization process would be the introduction of computer simulations, which will partially dispose of the use for prototypes and consequently allows for a much faster and cost effective design parameter evaluation. This has become possible thanks to various breakthroughs in the field of electromagnetics, e.g., the development of Krylov's iterative techniques, the conjugate gradient scheme (CGFFT) [16] and [17], and the fast multipole method (FMM) [7], together with an ever growing increase in computing power. It is nowadays possible to create and simulate some fairly accurate mathematical models of practical antenna designs within a reasonable amount of time. Together with the widespread availability of powerful search algorithms [15], the automation of the optimization process comes within reach. Unfortunately, the optimization process has some nasty properties, which make it hard to tackle. One of these properties is the existence of multiple local and/or global optima. As mentioned earlier, the time it takes to evaluate a parameter set has become reasonably short by the use of computer simulations, but if multiplied by the number of attempts required to let the search algorithm converge it will still take a lot of time. For instance if the number of attempts is about a hundred, which is a rather optimistic amount, every minute it takes to evaluate a set of parameters will become several hours. Consequently, the amount of time required to fulfill the optimization process will, depending on the complexity of electromagnetic problem, still be considerably large. If a gradient-based search algorithm is employed a considerable amount of time can be saved by considering the adjoint problem [6]. Note that this approach was also followed in [3, Section 5.1], and by many others.

Only large antenna arrays are considered in this report, meaning that they have a large number of antenna elements, e.g., 15×15 elements or more. Furthermore, the considered antenna array is composed of a dielectric layer, which is sandwiched between a ground plane on one side and metallic patches on the other side. The metallic patches are organized in a two-dimensional uniform array. Note that the presence of the ground plane allows for the separate evaluation of the radiating elements and the rest of the radar system. The array is excited by probes penetrating the ground plane, which are not connected to the patches. A cross-section of this configuration is depicted schematically in Figure 1.3. The model employed to simulate the behavior of the large patch-antenna array is known as the infinite-array model. The model assumes that the array is infinite in its extent and will therefore neglect various edge effects, which are certain to arise in the actual array [2]. A more extensive discussion of the model is presented in Chapter 2. The mathematical formulation of the model will incorporate excitation of the model by means of dipoles situated underneath the patches and excitation by an incident plane wave. The derived expressions for the generated far field, will allow for a first attempt in automating the optimization process. The infinite-array model will be optimized for two different optimization goals, viz., the radiated power and circular polarization, while considering only a small number of design parameters. Afterwards the results are analyzed.

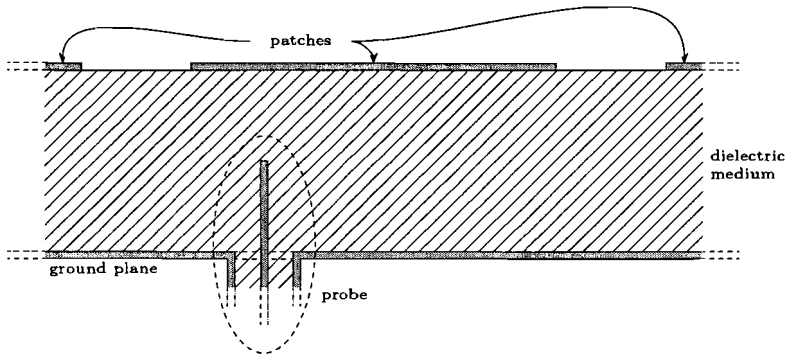

Figure 1.3: A cross-section of the very large patch antenna array.

In Chapter 2, the infinite-array model is formulated mathematically. In Chapter 3, the appropriate expressions are derived for both excitation cases. The first case involves an incident plane wave. The second case involves the excitation by means of one or more probes situated underneath the patches. A expression for the radiated far field is derived in Chapter 4, which is considered a good measure of the antennas performance under operating conditions. In Chapter 5, the optimization goals are set, the optimization of the model is attempted for several configurations, and the results are analyzed. Conclusions and recommendation are given in Chapter 6.

Chapter 2

Geometry and Formulation

2.1 Geometry

One of the first steps in solving a problem is the generation of a model, which is a way of reducing the complexity of the problem, in order to obtain a problem that is (hopefully) still manageable. Reducing the complexity of the problem is of course not without consequence. The model shall in return for obtaining an easier problem not account for several (minor) details. In effect, the obtained answer can only approximate the true solution. The very large patch-antenna array, as shown in Figure 1.2, is a finite two-dimensional

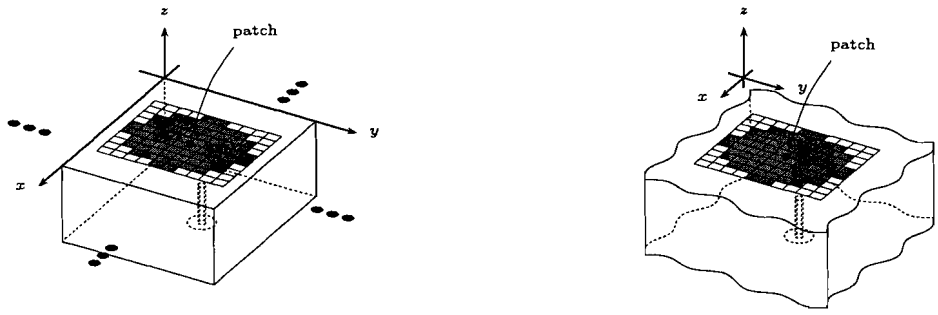

Figure 2.1: Two configurations, where (a) depicts a unit cell of the infinite-array model and (b) depicts the same cell, but now positioned in a infinite dielectric medium, the so-called single-cell configuration.

and uniform array. A large number of patches with identical but arbitrary shape cover its upper surface and they reside on top of a dielectric medium. In turn, a metal sheet the so-called ground plane backs the dielectric medium. Probes positioned underneath the patches penetrate the ground plane but do not connect to the patches. Within the whole structure a unit cell can be identified which is repeated many times and is marked by the dashed box in Figure 1.2. The so-called infinite-array model is used to model the

electromagnetic behavior of the very large patch-antenna array. As the name of the model already denotes, it is the infinite continuation of the unit cell as depicted in Figure 2.1a. This unit cell models the unit cell previously identified in the real array. Because of the model's infinite extent, it will neglect various edge effects, which are certain to arise in the real array. The advantage of using this model is that the calculations to simulate the infinite array reduce to the ones needed for the simulation of a unit cell positioned in an infinite dielectric medium, which will be referred to as a single cell, as depicted in Figure 2.1b. Where as a finite array model requires approximately the same amount of calculations times the size of the array, e.g. an array of $15 \times 15 = 225$ elements requires roughly 225 times the amount of calculations. The previous example clearly shows that application of the infinite-array model will dramatically reduce the total calculation time.

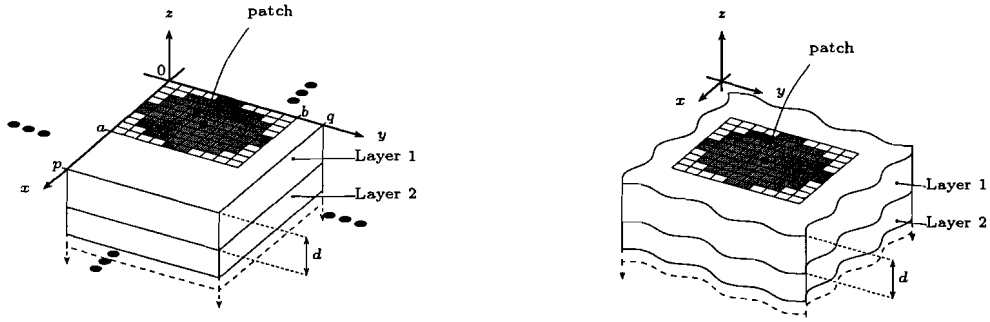

Figure 2.2: Two layered configurations; (a) depicts a unit cell of the infinite-array model and (b) the single-cell configuration.

The model consists of two parts. The first part models the layered structure; the second part models the excitation, which will be discussed in the first section of Chapter 3. The model approach for the layered structure is a more general one than needed to model the array. As a matter of fact the model could simulate a frequency-selective surface (FSS), which is a property that will be exploited to test the far-field derivation of Chapter 4 against already published data. While considering a single cell as depicted in Figure 2.2a, the layered structure is composed of two half spaces. The half space, $z < 0$, is characterized by a stratified medium. The half space, $z > 0$, is considered homogeneous. The patches partially cover the interface at $z = 0$ with a period equal to p and q, which denote the maximum cell dimensions for the x- and y-direction, respectively. Although the patches depicted in Figure 1.2 are rectangular a patch is allowed to have an arbitrary shape that will fit on a uniform rectangular mesh, although the patch is restricted to fit within the area $a \times b$, where a and b denote the maximum dimensions for the x- and y-direction, respectively. Note that $0 < a < p$ and $0 < b < q$ must hold. Considering the metallic surfaces infinitely thin and perfectly conducting will allow the enforcement of their presence by satisfying the appropriate boundary conditions. With this model, a

single layer with thickness d and two reflection coefficients defined at $z = -d$ will describe the half space containing the stratified medium. The two reflection coefficients $R^e_{1,2}$ and $R^h_{1,2}$ will account for the interaction between layer one and the rest of the layers. The superscript ^{e} and ^{h} denote the E- and H-polarization contributions, respectively.
Note that throughout Sections 2, 3 and 4 the layered structure denotes the single-cell situation, as depicted in Figure 2.2b. In Section 5, the infinite-array situation is considered, in order to put its periodicity property to use, which allows for a reduction of the number of calculations.

2.2 Transmission-line equations

The point of departure are Maxwell's equations in the frequency domain assuming linear isotropic media and an $\exp(j\omega t)$ time dependence, which will be suppressed throughout this report.

$$\boldsymbol{\nabla} \times \boldsymbol{H} = j\omega\varepsilon \boldsymbol{E} + \boldsymbol{J}\,, \tag{2.1a}$$
$$\boldsymbol{\nabla} \times \boldsymbol{E} = -j\omega\mu \boldsymbol{H}\,, \tag{2.1b}$$

where $\boldsymbol{E}$ and $\boldsymbol{H}$ denote the electric and magnetic field, respectively. The dielectric medium below the patches is modeled as a stratified medium. As a consequence ε and μ will only depend on the z-coordinate, i.e., $\varepsilon(\boldsymbol{r}) = \varepsilon(z)$ and $\mu(\boldsymbol{r}) = \mu(z)$. The transverse spatial Fourier transformation is defined as

$$\hat{\boldsymbol{F}}(\boldsymbol{k}_T, z, \omega) = \int_{-\infty}^{\infty}\int_{-\infty}^{\infty} \boldsymbol{F}(\boldsymbol{r}, \omega) \exp(j\,\boldsymbol{k}_T \cdot \boldsymbol{r}_T)\, dx\, dy\,, \tag{2.2a}$$

$$\boldsymbol{F}(\boldsymbol{r}, \omega) = \frac{1}{4\pi^2} \int_{-\infty}^{\infty}\int_{-\infty}^{\infty} \hat{\boldsymbol{F}}(\boldsymbol{k}_T, z, \omega) \exp(-j\,\boldsymbol{k}_T \cdot \boldsymbol{r}_T)\, dk_x\, dk_y\,, \tag{2.2b}$$

where $\boldsymbol{k}_T = k_x \boldsymbol{u}_x + k_y \boldsymbol{u}_y$ and $\boldsymbol{r}_T = x\,\boldsymbol{u}_x + y\,\boldsymbol{u}_y$. Applying this to Eqs. (2.1a) and (2.1b) together with the decomposition $\hat{\boldsymbol{E}} = \hat{\boldsymbol{E}}_T + \hat{E}_z \boldsymbol{u}_z$, $\hat{\boldsymbol{H}} = \hat{\boldsymbol{H}}_T + \hat{H}_z \boldsymbol{u}_z$ and $\hat{\boldsymbol{J}} = \hat{\boldsymbol{J}}_T + \hat{J}_z \boldsymbol{u}_z$, results in a set of equations, which can be separated into longitudinal and transverse parts, i.e.,

$$-j\,\boldsymbol{k}_T \times \hat{\boldsymbol{H}}_T = j\omega\varepsilon(z)\hat{E}_z \boldsymbol{u}_z + \hat{J}_z \boldsymbol{u}_z\,, \tag{2.3a}$$
$$j\,\boldsymbol{k}_T \times \hat{\boldsymbol{E}}_T = j\omega\mu(z)\hat{H}_z \boldsymbol{u}_z\,, \tag{2.3b}$$

and

$$-j\,\boldsymbol{k}_T \times \hat{H}_z \boldsymbol{u}_z + \boldsymbol{u}_z \times \partial_z \hat{\boldsymbol{H}}_T = j\omega\varepsilon(z)\hat{\boldsymbol{E}}_T + \hat{\boldsymbol{J}}_T\,, \tag{2.3c}$$
$$-j\,\boldsymbol{k}_T \times \hat{E}_z \boldsymbol{u}_z + \boldsymbol{u}_z \times \partial_z \hat{\boldsymbol{E}}_T = -j\omega\mu(z)\hat{\boldsymbol{H}}_T\,. \tag{2.3d}$$

The substitution of Eq. (2.3a) and Eq. (2.3b) in Eq. (2.3c) and Eq. (2.3d) leads to the elimination of the longitudinal electromagnetic field components, viz.

$$\frac{k_T^2}{j\omega\mu(z)}\,\boldsymbol{u}_k \times (\boldsymbol{u}_k \times \hat{\boldsymbol{E}}_T) + \boldsymbol{u}_z \times \partial_z \hat{\boldsymbol{H}}_T = j\omega\varepsilon(z)\hat{\boldsymbol{E}}_T + \hat{\boldsymbol{J}}_T\,, \tag{2.4a}$$

$$\frac{-k_T^2}{j\omega\varepsilon(z)}\,\boldsymbol{u}_k \times (\boldsymbol{u}_k \times \hat{\boldsymbol{H}}_T) + \boldsymbol{u}_z \times \partial_z \hat{\boldsymbol{E}}_T = -j\omega\mu(z)\hat{\boldsymbol{H}}_T + (\boldsymbol{u}_z \times \boldsymbol{u}_k)\frac{k_T}{\omega\varepsilon(z)}\hat{J}_z\,, \tag{2.4b}$$

where $k_T^2 = |\boldsymbol{k}_T|^2 = k_x^2 + k_y^2$ and $\boldsymbol{u}_k = \boldsymbol{k}_T/k_T$. Note that this set of equations could also be expressed in terms of $\hat{\boldsymbol{B}}_z$ and $\hat{\boldsymbol{D}}_z$. Subsequently the equations are split in E- and H-polarization contributions by using the following decomposition:

$$\hat{\boldsymbol{E}}_T = j\boldsymbol{u}_k V^e(z) - \boldsymbol{u}_z \times j\boldsymbol{u}_k V^h(z)\,, \tag{2.5a}$$

$$\hat{\boldsymbol{H}}_T = j\boldsymbol{u}_k I^h(z) + \boldsymbol{u}_z \times j\boldsymbol{u}_k I^e(z)\,, \tag{2.5b}$$

where the V^e, I^e and V^h, I^h correspond to E- and H-polarization contributions of the electromagnetic field. After substitution Eqs. (2.4a) and (2.4b) can be split into:

$$\partial_z I^h = -\frac{\gamma^2}{j\omega\mu}\,V^h - (\boldsymbol{u}_z \times j\boldsymbol{u}_k)\cdot\hat{\boldsymbol{J}}_T\,, \tag{2.6a}$$

$$\partial_z V^h = -j\omega\mu I^h\,, \tag{2.6b}$$

and

$$\partial_z I^e = -j\omega\varepsilon V^e + j\boldsymbol{u}_k\cdot\hat{\boldsymbol{J}}_T\,, \tag{2.6c}$$

$$\partial_z V^e = -\frac{\gamma^2}{j\omega\varepsilon}\,I^e + \frac{k_T}{j\omega\varepsilon}\hat{J}_z\,, \tag{2.6d}$$

where $\gamma = \sqrt{k_T^2 - \omega^2\varepsilon\mu}$ and ε, μ, γ are all functions of z. The infinite-array model has only metallic patches at $z = 0$, therefore the electric current density $\boldsymbol{J}$ reduces to an electric surface current density $\boldsymbol{J}_{\mathcal{S}}$ which resides at $z = 0$. As a consequence $\hat{\boldsymbol{J}}_T = \hat{\boldsymbol{J}}_{\mathcal{S}}\,\delta(z)$ and $\hat{J}_z = 0$. After substitution Eqs. (2.6a) through (2.6d) reduce to:

$$\partial_z I^h = -\frac{\gamma^2}{j\omega\mu}\,V^h - (\boldsymbol{u}_z \times j\boldsymbol{u}_k)\cdot\hat{\boldsymbol{J}}_{\mathcal{S}}\,\delta(z)\,, \tag{2.7a}$$

$$\partial_z V^h = -j\omega\mu I^h\,, \tag{2.7b}$$

and

$$\partial_z I^e = -j\omega\varepsilon V^e + j\boldsymbol{u}_k\cdot\hat{\boldsymbol{J}}_{\mathcal{S}}\,\delta(z)\,, \tag{2.7c}$$

$$\partial_z V^e = -\frac{\gamma^2}{j\omega\varepsilon}\,I^e\,, \tag{2.7d}$$

where $\gamma = \sqrt{k_T^2 - \omega^2\varepsilon\mu}$ and ε, μ, γ are all functions of z.

2.3 Stratified media

The mathematical result of the preceding section, i.e., Eqs. (2.7a) through (2.7d) hold generally for isotropic layered media and describes the transverse components of the fields, which are related to the longitudinal components through Eqs. (2.3a) and (2.3b) and therefore they effectively describe the entire electromagnetic field. So solving the field problem for the electric field becomes equivalent to finding a solution for V^e and V^h at $z = 0$. The layers of the stratified medium are chosen to be piecewise homogeneous, as stated in Section 2.1. Therefore the permittivity and permeability of layer i will reduce to $\varepsilon_i(z) = \varepsilon_i$, $\mu_i(z) = \mu_i$ and the following expressions are obtained for V^e, which are valid for the half plane $z > 0$ and layer one, respectively, i.e.,

$$\partial_z^2 V_0^e(z) - \gamma_0^2 V_0^e(z) = 0 \quad \text{for} \quad z > 0\,, \tag{2.8a}$$
$$\partial_z^2 V_1^e(z) - \gamma_1^2 V_1^e(z) = 0 \quad \text{for} \quad -d < z < 0\,, \tag{2.8b}$$

where $\gamma_i = \sqrt{k_T^2 - \omega^2 \varepsilon_i \mu_i}$, $i \in \{0, 1\}$. Note that the positive solution of the square root or principal square root is chosen, i.e., $\Re\{\gamma_i\} \geq 0$ for $i \in \{0, 1\}$. Consequently $\Im\{\gamma_i\} \geq 0$ is chosen to ensure that the solution propagates or decays in the proper direction again for $i \in \{0, 1\}$. Eqs. (2.8a) and (2.8b) have the general solution:

$$V_0^e(z) = V_{0,-}^e \exp(\gamma_0 z) + V_{0,+}^e \exp(-\gamma_0 z)\,, \tag{2.9a}$$
$$V_1^e(z) = V_{1,-}^e \exp(\gamma_1 z) + V_{1,+}^e \exp[-\gamma_1 (z + d)]\,, \tag{2.9b}$$

where $V_{i,-}^e$ and $V_{i,+}^e$ denote the amplitudes in layer i of the downward and upward traveling solutions, respectively. The scattered electromagnetic field, excited by the electric surface current density at $z = 0$, must remain finite in the far field and therefore only a decaying or propagating field solution in the positive z-direction is allowed. Consequently, $V_{0,-}^e$ must be equal to zero. This is known as the radiation condition. Substituting Eq. (2.7c) in Eq. (2.7d) reveals that the second derivative of $V^e(z)$ with respect to z must result in a delta pulse, therefore $V^e(z)$ must contain a kink at $z = 0$, which ensures that $V^e(z)$ will be continuous at the interface $z = 0$, as it should be agreement with the boundary condition for the tangential part of the electric field as dictated by the Maxwell's equations. Therefore at the boundary $z = 0$, the condition

$$V_{0,+}^e = V_{1,-}^e + V_{1,+}^e \exp(-\gamma_1 d) \tag{2.10}$$

holds. Due to the electric surface current density on the patch, the tangential component of the magnetic field (and thus I^e) will be discontinuous at $z = 0$, i.e.,

$$\boldsymbol{n} \times \hat{\boldsymbol{H}}_0 - \boldsymbol{n} \times \hat{\boldsymbol{H}}_1 = \hat{\boldsymbol{J}}_S\,, \tag{2.11}$$

where $\hat{\boldsymbol{H}}_0$ and $\hat{\boldsymbol{H}}_1$ denote the magnetic field close to the interface at $z = 0^+$ and $z = 0^-$, respectively, $\boldsymbol{n}$ denotes the normal of the surface $\mathcal{P}$, which in this case coincides with $\boldsymbol{u}_z$.

$\hat{\boldsymbol{J}}_{\mathcal{S}}$ denotes in this case the electric surface current density residing at the surface $\mathcal{P}$. The substitution of Eq. (2.5b) in Eq. (2.11) results in,

$$j(\boldsymbol{u}_z \times j\boldsymbol{u}_k)\left[I^h(0^+) - I^h(0^-)\right] - j\boldsymbol{u}_k\left[I^e(0^+) - I^e(0^-)\right] = \hat{\boldsymbol{J}}_{\mathcal{S}}\,, \tag{2.12}$$

which can be split into terms for $\boldsymbol{u}_k$ and $\boldsymbol{u}_z \times \boldsymbol{u}_k$. The proposed separation of terms results in:

$$I^e(0^+) - I^e(0^-) = j\boldsymbol{u}_k \cdot \hat{\boldsymbol{J}}_{\mathcal{S}}\,, \tag{2.13a}$$

$$I^h(0^+) - I^h(0^-) = -(\boldsymbol{u}_z \times j\boldsymbol{u}_k) \cdot \hat{\boldsymbol{J}}_{\mathcal{S}}\,. \tag{2.13b}$$

The interaction between layer one and all the rest of the layers underneath layer one is characterized by two reflection coefficients $R^e_{1,2}$ and $R^h_{1,2}$ defined at $z = -d$. The E- and H-polarization contributions are denoted by the superscripts ^{e} and ^{h}, respectively. Both can be defined as the ratio between the scattered and the incident field at the interface $z = -d$, i.e.,

$$R^e_{1,2} = \left.\frac{V^e_{1,+}\exp\left[-\gamma_1\left(z+d\right)\right]}{V^e_{1,-}\exp\left(\gamma_1 z\right)}\right|_{z=-d} = \frac{V^e_{1,+}}{V^e_{1,-}}\exp\left(\gamma_1 d\right). \tag{2.14}$$

By interchanging the superscripts ^{e} and ^{h}, an equation is found for $R^h_{1,2}$, which denotes the H-polarization reflection coefficient. It is now possible to write the following for the transverse field components at $z = 0$:

$$\begin{aligned} V^e_1(z=0) &= \left\{V^e_{1,+}\exp\left[-\gamma_1\left(z+d\right)\right] + V^e_{1,-}\exp\left(\gamma_1 z\right)\right\}\big|_{z=0} \\ &= V^e_{1,+}\exp\left(-\gamma_1 d\right) + V^e_{1,-} \\ &= R^e_{1,2}V^e_{1,-}\exp\left(-\gamma_1 d\right)\exp\left(-\gamma_1 d\right) + V^e_{1,-} \\ &= V^e_{1,-}\left[1 + R^e_{1,2}\exp\left(-2\gamma_1 d\right)\right]\,. \end{aligned} \tag{2.15}$$

Again, by interchanging the superscripts ^{e} and ^{h} reveals the H-polarization counterpart. Reusing Eq. (2.7d) and taking the limit as z approaches 0 from below yields the following relation between $I^e(0^-)$, $V^e_{1,-}$, and $V^e_{1,+}$:

$$\begin{aligned} \partial_z V^e &= -\frac{\gamma^2}{j\omega\varepsilon}I^e && \Rightarrow \\ \lim_{z\uparrow 0}\partial_z V^e &= -\lim_{z\uparrow 0}\frac{\gamma^2}{j\omega\varepsilon}I^e && \Rightarrow \\ \gamma_1\left[V^e_{1,-} - V^e_{1,+}\exp\left(-\gamma_1 d\right)\right] &= -\frac{{\gamma_1}^2}{j\omega\varepsilon_1}I^e(0^-) && \Rightarrow \\ -\frac{j\omega\varepsilon_1}{\gamma_1}\left[V^e_{1,-} - V^e_{1,+}\exp\left(-\gamma_1 d\right)\right] &= I^e(0^-)\,. \end{aligned} \tag{2.16}$$

By using Eq. (2.7d) and taking this time the limit as z approaches 0 from above yields the following relation between $I^e(0^+)$, and $V^e_{0,+}$:

$$\frac{j\omega\varepsilon_0}{\gamma_0}V^e_{0,+} = I^e(0^+)\,. \tag{2.17}$$

The substitution of Eqs. (2.16) and (2.17) in Eq. (2.13a) yields:

$$\frac{j\omega\varepsilon_0}{\gamma_0}V^e_{0,+} + \frac{j\omega\varepsilon_1}{\gamma_1}\left[V^e_{1,-} - V^e_{1,+}\exp\left(-\gamma_1 d\right)\right] = j\boldsymbol{u}_k \cdot \hat{\boldsymbol{J}}_S\,. \tag{2.18}$$

Together with Eq. (2.10) and Eq. (2.14) it is possible to eliminate $V^e_{1,-}$ and $V^e_{1,+}$ and the following relation between $V^e_{0,+}$ and $\hat{\boldsymbol{J}}_S$ is found:

$$V^e_{0,+} = \underbrace{\frac{\gamma_0\gamma_1\left[1 + R^e_{1,2}\exp\left(-2\gamma_1 d\right)\right]}{j\omega\left\{\varepsilon_0\gamma_1\left[1 + R^e_{1,2}\exp\left(-2\gamma_1 d\right)\right] + \varepsilon_1\gamma_0\left[1 - R^e_{1,2}\exp\left(-2\gamma_1 d\right)\right]\right\}}}_{=A(k_T)} j\boldsymbol{u}_k \cdot \hat{\boldsymbol{J}}_S\,. \tag{2.19}$$

In a similar fashion a relation between $V^h_{0,+}$ and $\hat{\boldsymbol{J}}_S$ is found, i.e.,

$$V^h_{0,+} = -\underbrace{\frac{j\omega\mu_0\mu_1\left[1 + R^h_{1,2}\exp\left(-2\gamma_1 d\right)\right]}{\mu_1\gamma_0\left[1 + R^h_{1,2}\exp\left(-2\gamma_1 d\right)\right] + \mu_0\gamma_1\left[1 - R^h_{1,2}\exp\left(-2\gamma_1 d\right)\right]}}_{=B(k_T)} \left(\boldsymbol{u}_z \times j\boldsymbol{u}_k\right) \cdot \hat{\boldsymbol{J}}_S\,. \tag{2.20}$$

Substituting Eqs. (2.19) and (2.20) in Eq. (2.5a) results in a expression for $\hat{\boldsymbol{E}}^s_T$ at $z = 0$,

$$\hat{\boldsymbol{E}}^s_T\left(\boldsymbol{k}_T, 0\right) = -\frac{\boldsymbol{k}_T}{k_T^2}\left[A\left(k_T\right) - B\left(k_T\right)\right]\left(\boldsymbol{k}_T \cdot \hat{\boldsymbol{J}}_S\right) - B\left(k_T\right)\hat{\boldsymbol{J}}_S\,, \tag{2.21}$$

where the superscript ^{s} denotes the scattered field, which is, in this case, the electric field due to the induced surface current density on the patch. By applying Eq. (2.2b) a relation between $\boldsymbol{E}^s_T$ and $\boldsymbol{J}_S$ can be obtained, i.e.,

$$\begin{aligned}
\boldsymbol{E}^s_T\left(\boldsymbol{r}_T, 0\right) =& \frac{1}{4\pi^2}\int_{-\infty}^{\infty}\int_{-\infty}^{\infty}\hat{\boldsymbol{E}}^s_T\left(\boldsymbol{k}_T, 0\right)\exp\left(-j\boldsymbol{k}_T \cdot \boldsymbol{r}_T\right)d\boldsymbol{k}_T \\
=& -\frac{1}{4\pi^2}\int_{-\infty}^{\infty}\int_{-\infty}^{\infty}\left\{\frac{\boldsymbol{k}_T}{k_T^2}\left[A(k_T) - B(k_T)\right]\left(\boldsymbol{k}_T \cdot \hat{\boldsymbol{J}}_S\right)\right\}\exp\left(-j\boldsymbol{k}_T \cdot \boldsymbol{r}_T\right)d\boldsymbol{k}_T \\
& - \frac{1}{4\pi^2}\int_{-\infty}^{\infty}\int_{-\infty}^{\infty}B\left(\boldsymbol{k}_T\right)\hat{\boldsymbol{J}}_S\exp\left(-j\boldsymbol{k}_T \cdot \boldsymbol{r}_T\right)d\boldsymbol{k}_T
\end{aligned} \tag{2.22a}$$

Using the fact that multiplying by $j\boldsymbol{k}_T$ in the spectral domain corresponds to applying $\boldsymbol{\nabla}_T = \partial_x\boldsymbol{u}_x + \partial_y\boldsymbol{u}_y$ in the spatial domain reduces the previous equation to:

$$\begin{aligned}
\boldsymbol{E}^s_T\left(\boldsymbol{r}_T, 0\right) =& \boldsymbol{\nabla}_T\boldsymbol{\nabla}_T \cdot \iint_{\mathcal{P}} G_1\left(\boldsymbol{r}_T - \boldsymbol{r}'_T\right)\boldsymbol{J}_S\left(\boldsymbol{r}'_T\right)d\boldsymbol{r}'_T \\
& - \iint_{\mathcal{P}} G_2\left(\boldsymbol{r}_T - \boldsymbol{r}'_T\right)\boldsymbol{J}_S\left(\boldsymbol{r}'_T\right)d\boldsymbol{r}'_T\,,
\end{aligned} \tag{2.22b}$$

where $\boldsymbol{r}_T \in \mathbb{R}^2$ and $\mathcal{P}$ is the surface where the surface current density resides.

$$G_1 = \frac{1}{4\pi^2} \int_{-\infty}^{\infty} \int_{-\infty}^{\infty} \frac{1}{{k_T}^2} \left[A\left(k_T\right) - B\left(k_T\right)\right] \exp\left(-j\boldsymbol{k}_T \cdot \boldsymbol{r}_T\right) dk_x \, dk_y \,, \tag{2.23a}$$

$$G_2 = \frac{1}{4\pi^2} \int_{-\infty}^{\infty} \int_{-\infty}^{\infty} B\left(k_T\right) \exp\left(-j\boldsymbol{k}_T \cdot \boldsymbol{r}_T\right) dk_x \, dk_y \,. \tag{2.23b}$$

The total transverse electric field $\boldsymbol{E}_T$ consists of two parts namely, the scattered field, which is excited by the electric surface current density and the incident field, which refers to the field that would be excited by the electromagnetic source if there would be no metallization present, i.e.,

$$\boldsymbol{E}_T = \boldsymbol{E}_T^s + \boldsymbol{E}_T^i \,. \tag{2.24}$$

On the metallic patch the boundary condition $\boldsymbol{E}_T = \boldsymbol{0}$ must hold and therefore:

$$\boldsymbol{E}_T^i = -\boldsymbol{E}_T^s \,, \qquad \text{for} \quad z = 0;\, \boldsymbol{r}_T \in \mathcal{P} \tag{2.25}$$

which effectively relates the incident field $\boldsymbol{E}_T^i$ and the electric surface current density $\boldsymbol{J}_S$.

2.4 Reflection coefficients

The previously introduced reflection coefficients $R_{1,2}^e$ and $R_{1,2}^h$ remain to be determined. To do so, certain assumptions need to be made about the interface at $z = -d$ and/or about the medium present underneath layer one. The following cases are considered.

- The interface at $z = -d$ consists of a perfectly conducting metallization, occupying the entire x-y-plane.
- The half space underneath layer one is homogeneous.
- The half space underneath layer one consists of multiple piecewise-homogeneous layers.
- The half space underneath layer one has continuously varying material properties along the z-axis, but is constant for any x-y-plane.

For the first assumption the reflection coefficients $R_{1,2}^e$ and $R_{1,2}^h$ are equal to -1. With the second assumption it is possible to express the reflection coefficients in terms of the material properties. To find the appropriate expressions, consider the situation depicted in Figure 2.3, where $V_{1,-}^e$, $V_{2,-}^e$ and $V_{1,+}^e$ denote the amplitudes of the downward and upward traveling wave solutions in the appropriate layers. Note that of course the same situation

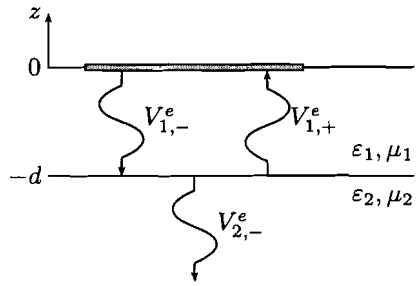

Figure 2.3: Transverse fields situation, with a homogeneous half space at $z < -d$

holds for the H-polarization contribution denoted with the superscript ^{h}. Reusing the same derivation as for Eqs. (2.16) and (2.17) the following two relations are found:

$$-\frac{j\omega\varepsilon_1}{\gamma_1}\left[V^e_{1,-}\exp\left(-\gamma_1 d\right) - V^e_{1,+}\right] = I^e\left(-d^+\right)\,, \tag{2.26a}$$

$$-\frac{j\omega\varepsilon_2}{\gamma_2}V^e_{2,-} = I^e\left(-d^-\right)\,. \tag{2.26b}$$

The substitution of these relations in Eq. (2.13a) reveals

$$-\frac{j\omega\varepsilon_1}{\gamma_1}\left[V^e_{1,-}\exp\left(-\gamma_1 d\right) - V^e_{1,+}\right] + \frac{j\omega\varepsilon_2}{\gamma_2}V^e_{2,-} = 0\,, \tag{2.27}$$

together with

$$V^e_{2,-} = V_{1,-}\exp\left(-\gamma_1 d\right) + V^e_{1,+}\,, \tag{2.28}$$

which is a direct result from preserving the boundary conditions for transverse electric fields at the interface $z = -d$. The substitution of Eq. (2.28) in Eq. (2.27) and subsequently the substitution of Eq. (2.14) eliminates $V^e_{1,-}$, $V^e_{1,+}$ and $V^e_{2,-}$ and reveals:

$$R^e_{1,2} = \frac{\varepsilon_1\gamma_2 - \varepsilon_2\gamma_1}{\varepsilon_1\gamma_2 + \varepsilon_2\gamma_1}\,. \tag{2.29}$$

In a similar fashion a relation which expresses the reflection coefficient for the H-polarization contribution, is found:

$$R^h_{1,2} = \frac{\mu_2\gamma_1 - \mu_1\gamma_2}{\mu_2\gamma_1 + \mu_1\gamma_2} \tag{2.30}$$

If the half space underneath layer one consist of multiple piecewise homogenous layers the scattering matrix formalism as developed in [12], [14] can be used. It effectively cascades the effects of the multiple layers. The same technique can be used to handle the case of continuously layered media. Several recursive algorithms have been developed in the Electromagnetics group at the University of Technology in Eindhoven for solving the according differential equations numerically [22].

2.5 Periodicity put to good use

Until now the periodicity of the problem has not been used. To do so some tools have to be derived first. As mentioned before in Section 2.1 the model of the array is an extended version of the real problem. If viewed upon as depicted in Figure 2.4 it is clear that the metallization is periodic with respect to the two primitive vectors $p\boldsymbol{u}_x$ and $q\boldsymbol{u}_y$ along the x- and y-direction. From this characteristic a Bravais lattice can be constructed,

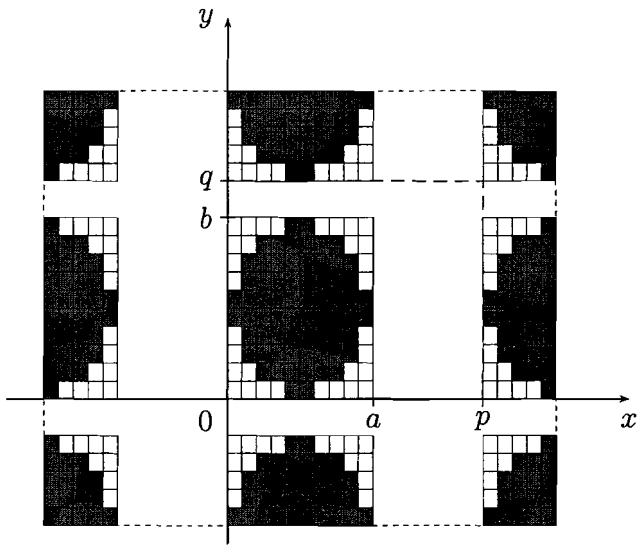

Figure 2.4: Top view of the array model

$$\boldsymbol{R}_{m,n} = mp\boldsymbol{u}_x + nq\boldsymbol{u}_y\,; \quad m,n \in \mathbb{Z}\,, \tag{2.31}$$

and a corresponding translation operator is defined as:

$$T_{m,n} f(\boldsymbol{r}) = f\left(\boldsymbol{r} + \boldsymbol{R}_{m,n}\right)\,. \tag{2.32}$$

When the medium is horizontally stratified, i.e., $\varepsilon(\boldsymbol{r}) = \varepsilon(z)$ and $\mu(\boldsymbol{r}) = \mu(z)$, Maxwell's equations reduce to,

$$\nabla \times \boldsymbol{H} = j\omega\varepsilon(z)\boldsymbol{E} + \boldsymbol{J}\,, \tag{2.33a}$$

$$\nabla \times \boldsymbol{E} = -j\omega\mu(z)\boldsymbol{H}\,. \tag{2.33b}$$

Applying the previously defined translational operator to Eqs. (2.33a) and (2.33b) results in:

$$\nabla \times T_{m,n}\left(\boldsymbol{H}\right) = j\omega\varepsilon\left(z\right) T_{m,n}\left(\boldsymbol{E}\right) + T_{m,n}\left(\boldsymbol{J}\right)\,, \tag{2.34a}$$

$$\nabla \times T_{m,n}\left(\boldsymbol{E}\right) = -j\omega\mu\left(z\right) T_{m,n}\left(\boldsymbol{H}\right)\,. \tag{2.34b}$$

Eqs. (2.34a) and (2.34b) clearly show that Maxwell's equations are invariant with respect to a periodic translation in the x-y-plane when the medium is horizontally stratified. Together with the boundary conditions, which are also invariant with respect to the same discrete translation in the x-y-plane, they form a linear operation, which can be represented by a single linear operator $\mathcal{L}$. This linear operator $\mathcal{L}$ is therefore also invariant with respect to this discrete translation, i.e.,

$$T_{m,n}\left(\mathcal{L}u\right) = \mathcal{L}T_{m,n}(u)\,. \tag{2.35}$$

Now consider the following operator equation,

$$\mathcal{L}u = f\,. \tag{2.36}$$

Assuming $\mathcal{L}^{-1}$ exists and that the forcing function f is quasi periodic, i.e.,

$$T_{m,n}\left(f\right) = f\exp\left[j\left(m\Omega_x + n\Omega_y\right)\right], \tag{2.37}$$

the following nice result is found,

$$\begin{aligned} \mathcal{L}u &= f && \Rightarrow \\ T_{m,n}\left(\mathcal{L}u\right) &= T_{m,n}\left(f\right) && \Rightarrow \\ \mathcal{L}T_{m,n}\left(u\right) &= f\exp\left[j\left(m\Omega_x + n\Omega_y\right)\right] && \Rightarrow \\ T_{m,n}(u) &= u\exp\left[j\left(m\Omega_x + n\Omega_y\right)\right], \end{aligned} \tag{2.38}$$

where Ω_x and Ω_y denote the propagation constants of the forcing function f for the x- and y-directions, respectively. These propagation constants will be examined later on in Chapter 3. Closer examination of Eq. (2.38) shows that u must contain a periodic part denoted by u^P, i.e., $T_{m,n}\left(u^P\right) = u^P$, where the superscript ^{P} denotes the periodicity of u^P. To put it in a nutshell a periodic system will react quasi periodic when it is excited by a quasi-periodic forcing function. For both excitation cases, i.e., the dipole and plane-wave excitation, the forcing function is quasi periodic. This means that for both cases the electric surface current density $\boldsymbol{J}_S$ and hence the scattered field $\boldsymbol{E}^s$, will be quasi periodic. Applying the previously derived property to the electric surface current density $\boldsymbol{J}_S(\boldsymbol{r}_T)$ results in:

$$\boldsymbol{J}_S(\boldsymbol{r}_T + \boldsymbol{R}_{m,n}) = \boldsymbol{J}_S^P(\boldsymbol{r}_T)\exp\left(-j\boldsymbol{k}_T^i\cdot\boldsymbol{R}_{m,n}\right), \tag{2.39}$$

where $\boldsymbol{k}_T^i = \Omega_x\boldsymbol{u}_x + \Omega_y\boldsymbol{u}_y$ and $\boldsymbol{J}_S^P(\boldsymbol{r}_T) = \boldsymbol{J}_S^P(\boldsymbol{r}_T + \boldsymbol{R}_{m,n})$. A similar relation can be derived for the scattered field.

The fact that the response will be quasi periodic when the system is excited by an quasi periodic function justifies the single-cell analysis as can be shown by the following analysis. The analysis starts out with Eq. (2.22b), which is rewritten in the following manner by combining the two Green's functions into one and by splitting up the integrals, i.e.,

$$\begin{aligned}\boldsymbol{E}_T^s(z=0) &= \iint_{\mathcal{P}} \boldsymbol{G}_{12}\left(\boldsymbol{r}_T - \boldsymbol{r}_T'\right)\cdot \boldsymbol{J}_{\mathcal{S}}\left(\boldsymbol{r}_T'\right)\, d\boldsymbol{r}_T' \\ &= \sum_m \sum_n \iint_{\mathcal{P}_{m,n}} \boldsymbol{G}_{12}\left(\boldsymbol{r}_T - \boldsymbol{r}_T'\right)\cdot \boldsymbol{J}_{\mathcal{S}}\left(\boldsymbol{r}_T'\right)\, d\boldsymbol{r}_T' \\ &= \sum_m \sum_n \iint_{\mathcal{P}_{0,0}} \boldsymbol{G}_{12}\left(\boldsymbol{r}_T - \boldsymbol{r}_T' - \boldsymbol{R}_{m,n}\right)\cdot \boldsymbol{J}_{\mathcal{S}}\left(\boldsymbol{r}_T' + \boldsymbol{R}_{m,n}\right)\, d\boldsymbol{r}_T' ,\end{aligned} \tag{2.40}$$

where $m, n \in \mathbb{Z}$ and $\mathcal{P}_{0,0}$ or more general $\mathcal{P}_{m,n}$ denotes a surface area that covers a unit cell or in other words cover a single period of the infinite-array model. It is now possible to use the quasi periodicity of electric surface current density, $\boldsymbol{J}_{\mathcal{S}}$, to relate the current density of the 'center' patch, $\boldsymbol{J}_{\mathcal{S}}^0$, to the scattered electric field by substituting Eq. (2.39), i.e.,

$$\boldsymbol{E}_T^s(z=0) = \sum_m \sum_n \iint_{\mathcal{P}_{0,0}} \boldsymbol{G}_{12}\left(\boldsymbol{r}_T - \boldsymbol{r}_T' - \boldsymbol{R}_{m,n}\right)\cdot \boldsymbol{J}_{\mathcal{S}}^0\left(\boldsymbol{r}_T'\right)\exp\left(-j\boldsymbol{k}_T^i\cdot\boldsymbol{R}_{m,n}\right) d\boldsymbol{r}_T' . \tag{2.41}$$

Although the equation above is not a very convenient one it already justifies the single-cell analysis. Employing the fact that $\boldsymbol{J}_{\mathcal{S}}^0$ can only attain non-zero values at the 'center' patch restores the convolutional structure, i.e.,

$$\boldsymbol{E}_T^s(z=0) = \sum_m \sum_n \int_{-\infty}^{\infty}\int_{-\infty}^{\infty} \boldsymbol{G}_{12}\left(\boldsymbol{r}_T - \boldsymbol{r}_T' - \boldsymbol{R}_{m,n}\right)\cdot \boldsymbol{J}_{\mathcal{S}}^0\left(\boldsymbol{r}_T'\right)\exp\left(-j\boldsymbol{k}_T^i\cdot\boldsymbol{R}_{m,n}\right) d\boldsymbol{r}_T' , \tag{2.42}$$

where $\boldsymbol{k}_T^i = \Omega_x\boldsymbol{u}_x + \Omega_y\boldsymbol{u}_y$. Interchanging m and n with $-m$ and $-n$, respectively, yields

$$\begin{aligned}\boldsymbol{E}_T^s(z=0) &= \sum_m \sum_n \left(\boldsymbol{G}_{12} * \boldsymbol{J}_{\mathcal{S}}^0\right)\left(\boldsymbol{r}_T - \boldsymbol{R}_{m,n}\right)\exp\left(-j\boldsymbol{k}_T^i\cdot\boldsymbol{R}_{m,n}\right) \\ &= \sum_m \sum_n \left(\boldsymbol{G}_{12} * \boldsymbol{J}_{\mathcal{S}}^0\right)\left(\boldsymbol{r}_T + \boldsymbol{R}_{m,n}\right)\exp\left(j\boldsymbol{k}_T^i\cdot\boldsymbol{R}_{m,n}\right) .\end{aligned} \tag{2.43}$$

Note that the equation above can be identified as a Poisson summation formula like the equation below, which is derived in detail in Section A.1.

$$\frac{1}{p\,q}\sum_{m'}\sum_{n'} \hat{\Psi}\left(\frac{2\pi m'}{p}\boldsymbol{u}_x + \frac{2\pi n'}{q}\boldsymbol{u}_y\right) = \sum_m \sum_n \psi\left(mp\boldsymbol{u}_x + nq\boldsymbol{u}_y\right) , \tag{2.44}$$

where,

$$\hat{\Psi}\left(\frac{2\pi m'}{p}\boldsymbol{u}_x+\frac{2\pi n'}{q}\boldsymbol{u}_y\right)=\int_{-\infty}^{\infty}\int_{-\infty}^{\infty}\psi(\boldsymbol{r}_T)\exp\left[j\left(\frac{2\pi m'}{p}\boldsymbol{u}_x+\frac{2\pi n'}{q}\boldsymbol{u}_y\right)\cdot\boldsymbol{r}_T\right]d\boldsymbol{r}_T\,, \quad (2.45)$$

is the sampled version of the Fourier transform for a continuous function ψ as previously defined in Eq. (2.2a). Employing the Poisson summation formula reduces Eq. (2.43) to

$$\boldsymbol{E}_T^s\left(z=0\right)=\frac{1}{p\,q}\sum_m\sum_n\hat{\boldsymbol{G}}_{12}\left(\boldsymbol{k}_T^{m,n}\right)\cdot\hat{\boldsymbol{J}}_S^0\left(\boldsymbol{k}_T^{m,n}\right)\exp\left(-j\boldsymbol{k}_T^{m,n}\cdot\boldsymbol{r}_T\right), \quad (2.46)$$

which shows that the scattered field due to the surface-current density on the patches comprises so-called Floquet modes [1]. The subsequent substitution of the equation above yields

$$\begin{aligned}\boldsymbol{E}_T^i\left(z=0\right)&=-\frac{1}{p\,q}\sum_m\sum_n\hat{\boldsymbol{G}}_{12}\left(\boldsymbol{k}_T^{m,n}\right)\cdot\hat{\boldsymbol{J}}_S^0\left(\boldsymbol{k}_T^{m,n}\right)\exp\left(-j\boldsymbol{k}_T^{m,n}\cdot\boldsymbol{r}_T\right)\\&=\frac{1}{p\,q}\sum_m\sum_n\left[\boldsymbol{k}_T^{m,n}\hat{G}_1\left(\boldsymbol{k}_T^{m,n}\cdot\hat{\boldsymbol{J}}_S^0\right)+\hat{G}_2\hat{\boldsymbol{J}}_S^0\right]\exp\left(-j\boldsymbol{k}_T^{m,n}\cdot\boldsymbol{r}_T\right),\end{aligned} \quad (2.47)$$

where $\hat{G}_1$, $\hat{G}_2$ and $\hat{\boldsymbol{J}}_S^0$ are all functions of $\boldsymbol{k}_T^{m,n}$ and $\boldsymbol{k}_T^{m,n}=(2\pi m/p)\boldsymbol{u}_x+(2\pi n/q)\boldsymbol{u}_y+\boldsymbol{k}_T^i$. The final result shows that the solution for the electric surface current density distribution of a single patch only relies on the tangential part of the incident electric field.

Chapter 3

Excitation

3.1 Modeling issues

In practice the patch-antenna array can be excited by all sorts of electromagnetic sources, e.g., other antennas, probes, or open ends of waveguides situated underneath the patches. The effects of the different sources can be roughly divided into two categories according to their distance, measured in wavelengths, to the patch-antenna array. Sources positioned 'nearby' shall impress a fairly complex electromagnetic field distribution at the surface of the patches. On the other hand, the field distribution induced by a source positioned 'far away' will be almost the same as if the array were excited by an incident plane wave.

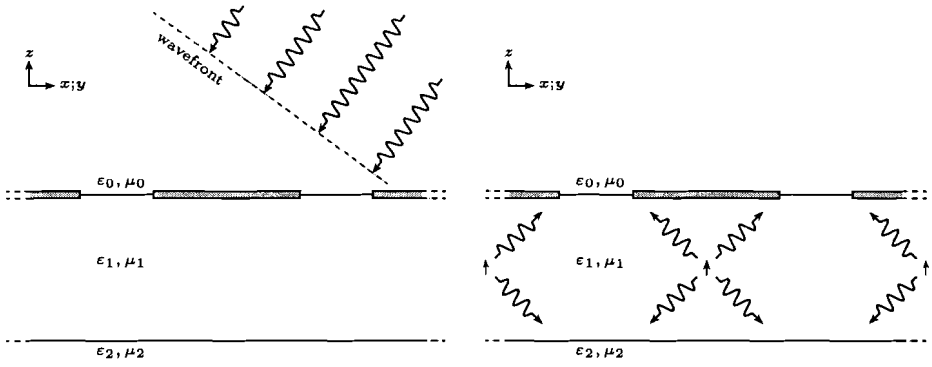

Figure 3.1: Two excitation models: (a) incident plane-wave, and (b) small electric dipoles situated underneath the patches.

This report is restricted to two cases of excitation, where each of the cases represents one of the two categories. The two excitation cases are: excitation by an incident plane wave and excitation by one or more probes situated underneath each patch of the ar-

ray. Modeling the first case is almost trivial, for the second case some trade offs have to be made. A practical example of a probe is the stripped end of a coaxial cable, which penetrates the ground plane. The probe has various characteristics, e.g. the length and thickness of the inner conductor, the diameter of the cable, the permittivity of the insulation material, the conductivity of the metal, and so on and so forth. All these details make something as simple as a probe already a fairly complex part to model accurately. In this report no attempt will be made to model the probe as accurately as possible, instead a simple model will be employed. Examination of a probe reveals that the tip of the inner conductor and its aperture are the parts that will radiate most of the electromagnetic energy. A model, which takes these parts of the probe into account, will most likely have an electromagnetic behavior, which includes the most significant electromagnetic properties of the probe. For reasons of (even more) simplicity the radiation from the aperture is neglected at first, but could always be added to the model as an equivalent magnetic current density residing at the aperture, which is frequently called a magnetic-frill source, for more details on this topic see [19]. Consequently, only the tip of the inner conductor of the probe is taken into account. It is modeled as a small electric dipole, which has no physical dimensions. In turn, this is equivalent to an electric current source, which is confined to a single point in space. Note that in case of multiple probes per patch the total excitation field is determined by superimposing the fields due to the individual probes. The two excitation models, viz. an incident plane wave and a small electric dipole situated underneath each patch of the array are depicted in Figure 3.1. The number of probes and their (relative) position underneath a patch are assumed to be identical for each unit cell of the array. This assumption ensures the periodicity of the infinite-array model.

In Section 2.5 Eq. (2.47) a relation between the incident electric field and the surface current density on the patch has been established. Before any attempt can be made to solve this equation numerically, an expression has to be derived, which relates the electromagnetic source to the field that excites the patches. This expression, which is often called a forcing function, indicated by f, has to be derived for each of the excitation cases (Section 3.2 and Section 3.3). Both forcing functions will be quasi periodic and as a consequence both will have the following property,

$$T_{m,n} f(\boldsymbol{r}) = f^P(\boldsymbol{r}) \exp\left(j\, \boldsymbol{k}_T^i \cdot \boldsymbol{R}_{m,n}\right) \tag{3.1}$$

where $f^P(\boldsymbol{r})$ denotes the periodic part of the forcing function and $\boldsymbol{k}_T^i = \Omega_x \boldsymbol{u}_x + \Omega_y \boldsymbol{u}_y$. The periodic part of the forcing function is determined, while utilizing the same single-cell analysis as used earlier to establish the relation between the tangential part of the electric field and the surface current density residing at the patch. As a consequence, a number of equations from Section 2.2 and Section 2.3 are reused in this chapter.

The basic principle behind the derivation of both forcing functions is the observation that the total electromagnetic field is a superposition of two fields, viz. the field induced by

the surface current density residing at the patch, i.e., the scattered field, and the field induced by the electromagnetic source in the presence of the same media, but in absence of the patches, i.e., the incident field. Note that the latter field will excite the patch. This approach is also followed in [21], [19], and references herein. The described decomposition is depicted in Figure 3.2. Note that for the sake of clarity the interaction between layer one and two is not depicted in the figure.

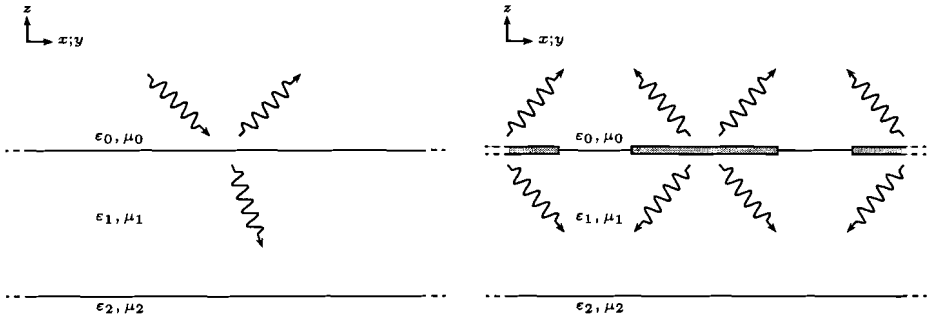

(a) (b)

Figure 3.2: Superposition of two fields. (a) The field due to the source (incident plane-wave case) in absence of the patches and (b) the scattered field due to the current density on the patch.

3.2 Plane-wave excitation

The forcing function for the incident plane wave case and its derivation are split into E- and H-polarization contributions. Revisiting the decomposition of the fields, as proposed in Eq. (2.5), justifies this. Afterwards, the derived expressions are added. Before any derivation is made, the source, which in this case is an incident plane wave, has to be characterized. An incident plane wave is defined by its angle of arrival (θ^i,ϕ^i), polarization and frequency, while assuming that the incident plane wave originates from the upper half space, i.e. $z > 0$. The incident plane wave can be represented in $\boldsymbol{k}$-space by a single mode, viz., the $(0,0)$-mode. As a consequence the $(0,0)$-mode will have a tangential wave-vector $\boldsymbol{k}_T$ equal to the tangential wave-vector $\boldsymbol{k}_T^i$ impressed by the incident plane wave, where $\boldsymbol{k}_T^i = \Omega_x^i \boldsymbol{u}_x + \Omega_y^i \boldsymbol{u}_y$. From the angle of arrival and the incident plane wave's frequency Ω_x^i and Ω_y^i can be distilled, which will define the phase variation of the quasi periodic forcing function at the surface, $z = 0$, of the infinite array for the x- and y-direction, respectively. If θ^i and ϕ^i are defined according to Figure 3.3, the following relation is found for Ω_x and Ω_y,

$$\Omega_x^i = -k_0 \sin\left(\theta^i\right) \cos\left(\phi^i\right), \tag{3.2a}$$

$$\Omega_y^i = -k_0 \sin\left(\theta^i\right) \sin\left(\phi^i\right), \tag{3.2b}$$

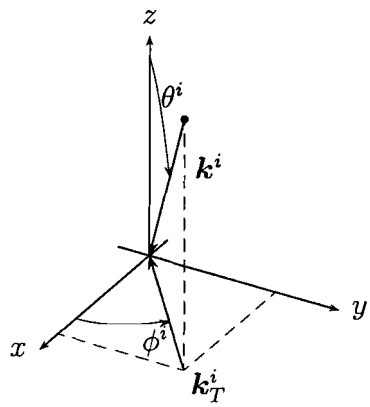

Figure 3.3: Angle of arrival definition.

where $k_0 = \omega\sqrt{\varepsilon_0\mu_0}$ denotes the propagation constant for the upper half space. The model will allow for all possible polarization configurations, because the incident field is defined by the complex amplitudes of the $\boldsymbol{u}_k$ and $\boldsymbol{u}_z \times \boldsymbol{u}_k$ terms.

The same single-cell analysis, as explained in Chapter 2, can now be used to derive the periodic part of the forcing function. The derivation of the E-polarization contribution of the forcing function starts by identifying the source term in Eq. (2.9). The incident plane wave is assumed to originate from somewhere in the upper half space $z > 0$. Consequently, $V^e_{0,-}$ is identified as the complex amplitude of the E-polarization contribution of the incident plane wave. As mentioned before, during this derivation the same media will be considered, but now in absence of the patches. The appropriate boundary conditions at $z = 0$ are therefore,

$$\boldsymbol{u}_z \times \boldsymbol{E}_0 - \boldsymbol{u}_z \times \boldsymbol{E}_1 = \boldsymbol{0}\,, \tag{3.3a}$$

$$\boldsymbol{u}_z \times \boldsymbol{H}_0 - \boldsymbol{u}_z \times \boldsymbol{H}_1 = \boldsymbol{0}\,, \tag{3.3b}$$

where $\{\boldsymbol{E}_0, \boldsymbol{H}_0\}$ and $\{\boldsymbol{E}_1, \boldsymbol{H}_1\}$ denote the electromagnetic field close to the interface at $z = 0^+$ and $z = 0^-$, respectively. The boundary condition Eq. (3.3a) is rewritten by employing the spatial Fourier transformation as defined in Eq. (2.2a) together with the decomposition as defined in Eq. (2.5a), i.e.,

$$\boldsymbol{u}_z \times j\,\boldsymbol{u}_k V_0^e\left(0^+\right) + j\,\boldsymbol{u}_k V_0^h\left(0^+\right) - \boldsymbol{u}_z \times j\,\boldsymbol{u}_k V_1^e\left(0^-\right) - j\,\boldsymbol{u}_k V_1^h\left(0^-\right) = \boldsymbol{0}\,. \tag{3.4}$$

The equation above can now be separated into terms with $\boldsymbol{u}_z \times \boldsymbol{u}_k$ or $\boldsymbol{u}_k$. Note that this is also a separation of the E- and H-polarization contributions denoted by the superscripts ^{e} and ^{h}, respectively. For the magnetic field boundary condition Eqs. (2.13a) and (2.13b) can be reused with the additional condition that $\hat{\boldsymbol{J}}_S$ is equal to zero owing to the absence

of the patches. As a consequence, the boundary conditions for E-polarization reduce to:

$$V_0^e\left(0^+\right) - V_1^e\left(0^-\right) = 0\,, \tag{3.5a}$$

$$I_0^e\left(0^+\right) - I_1^e\left(0^-\right) = 0\,. \tag{3.5b}$$

Note that if the superscript ^{e} is interchanged with ^{h} the boundary conditions for the H-polarization contribution are obtained. The substitution of Eqs. (2.9a) and (2.9b) in the boundary condition given in Eq. (3.5a), while using Eq. (2.15), establishes the following relation between $V_{0,+}^e$, $V_{0,-}^e$, and $V_{1,-}^e$.

$$V_{0,-}^e + V_{0,+}^e = V_{1,-}^e\left[1 + R_{1,2}^e \exp\left(-2\gamma_1 d\right)\right]\,, \tag{3.6}$$

where $\gamma_1 = \sqrt{\left(k_T^i\right)^2 - k_1^2}$, $k_T^i = |\boldsymbol{k}_T^i|$, $k_1^2 = \omega^2\varepsilon_1\mu_1$, and $R_{1,2}^e = R_{1,2}^e(\gamma_1)$. Employing the magnetic-field boundary conditions in a similar fashion yields,

$$\frac{j\omega\varepsilon_0}{\gamma_0}\left(V_{0,+}^e - V_{0,-}^e\right) = \frac{j\omega\varepsilon_1}{\gamma_1} V_{1,-}^e\left[R_{1,2}^e \exp\left(-\gamma_1 d\right) - 1\right]\,. \tag{3.7}$$

Combining Eq. (3.6) and Eq. (3.7), while using Eq. (2.15) yields,

$$V_1^e(z=0) = \frac{2\varepsilon_0\gamma_1 V_{0,-}^e\left[1 + R_{1,2}^e \exp\left(-2\gamma_1 d\right)\right]}{\gamma_1\varepsilon_0\left[1 + R_{1,2}^e \exp\left(-2\gamma_1 d\right)\right] + \gamma_0\varepsilon_1\left[1 - R_{1,2}^e \exp\left(-2\gamma_1 d\right)\right]}\,, \tag{3.8a}$$

which relates the $\boldsymbol{u}_k$ component of the incident electric field, $V_{0,-}^e$, to the E-polarization contribution of the tangential electric field, V_1^e at $z = 0$. The H-polarization contribution is derived analogously and its result is,

$$V_1^h(z=0) = \frac{2\gamma_0\mu_1 V_{0,-}^h\left[1 + R_{1,2}^h \exp\left(-2\gamma_1 d\right)\right]}{\gamma_0\mu_1\left[1 + R_{1,2}^h \exp\left(-2\gamma_1 d\right)\right] + \gamma_1\mu_0\left[1 - R_{1,2}^h \exp\left(-2\gamma_1 d\right)\right]}\,. \tag{3.8b}$$

Substitution of Eq. (3.8) in Eq. (2.5a) yields the spatial-Fourier transform of the forcing function $\boldsymbol{E}_T^i(z=0)$, i.e.,

$$\begin{aligned}\hat{\boldsymbol{E}}_T^i(z=0) = &\frac{2\varepsilon_0\gamma_1 V_{0,-}^e\left[1 + R_{1,2}^e \exp\left(-2\gamma_1 d\right)\right]}{\gamma_1\varepsilon_0\left[1 + R_{1,2}^e \exp\left(-2\gamma_1 d\right)\right] + \gamma_0\varepsilon_1\left[1 - R_{1,2}^e \exp\left(-2\gamma_1 d\right)\right]}\, j\boldsymbol{u}_k - \\ &\frac{2\gamma_0\mu_1 V_{0,-}^h\left[1 + R_{1,2}^h \exp\left(-2\gamma_1 d\right)\right]}{\gamma_0\mu_1\left[1 + R_{1,2}^h \exp\left(-2\gamma_1 d\right)\right] + \gamma_1\mu_0\left[1 - R_{1,2}^h \exp\left(-2\gamma_1 d\right)\right]}\, \boldsymbol{u}_z \times j\boldsymbol{u}_k\,,\end{aligned} \tag{3.9}$$

where $V_{0,-}^e$ and $V_{0,-}^h$ denote the E- and H-polarization contribution of the tangential electric field impressed by the incident plane wave. Exploiting the fact that the incident plane wave can be represented by only one mode, viz., the $(0,0)$-mode, establishes a relation for $\boldsymbol{E}_T^i$ at $z = 0$, i.e.,

$$\boldsymbol{E}_T^i(z=0) = \frac{1}{4\pi^2}\,\hat{\boldsymbol{E}}_T^i(z=0)\exp\left(-j\,\boldsymbol{k}_T^i \cdot \boldsymbol{r}_T\right)\,, \tag{3.10}$$

which concludes the derivation of the forcing function for the plane-wave excitation case.

3.3 Dipole excitation

Similar as for the incident-plane-wave case, the forcing function for the dipole-excitation case and its derivation is split into E- and H-polarization contributions, while employing the decomposition as proposed in Eq. (2.5). Although this time, the two resulting expressions end up to be far less symmetric. The derivation given in this section assumes only one dipole per unit cell, additional dipoles can always be added by employing the superposition principle. The small electric dipole is defined by its current I_z, fictitious length l, position $\boldsymbol{r}$, (radial) frequency ω and a phase factor. Note that the position of the

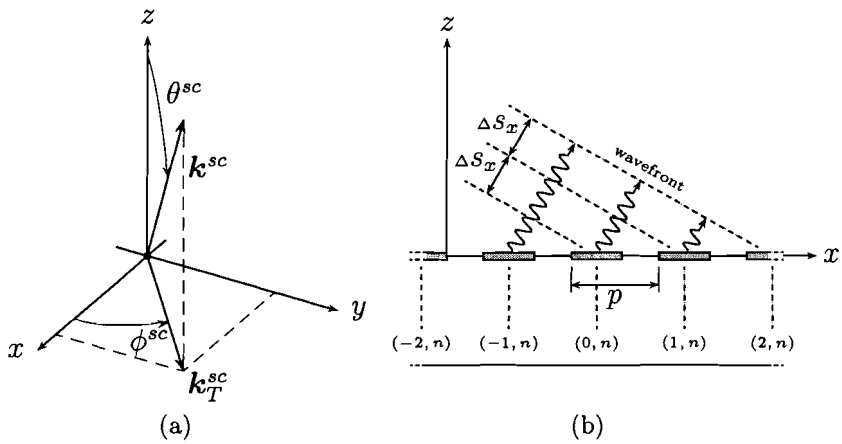

Figure 3.4: (a) Scan angle definition, where the superscript ^{sc} is short for "scan"; (b) Side view of the array, while it scans $(\theta^{sc}, \phi^{sc} = 0)$.

dipole is relative to the unit cell (m, n). The phase factor enables the infinite-array model to scan, or in other words create a single beam in a predetermined direction defined by the scan angle. This goal can be achieved by making sure that the electromagnetic waves, originating from each individual patch, will add up coherently for that direction. This effectively means that the phase of the waves have to be pre-corrected for the difference in covered distance, as depicted in Figure 3.4b. The difference in covered distance for electromagnetic waves originating from neighboring patches can be expressed in terms of scan angle and the period of the infinite-array model, i.e.,

$$\Delta s_x = p \sin(\theta^{sc}) \cos(\phi^{sc}), \tag{3.11a}$$

$$\Delta s_y = q \sin(\theta^{sc}) \sin(\phi^{sc}), \tag{3.11b}$$

for the x- and y-direction, respectively. The phase of an electromagnetic wave is related to the covered distance by the propagation constant of the medium, in this case k_0. Taking the center patch, indicated by $m = 0, n = 0$, as the point of reference, the appropriate

phase angles for a wave originating from patch (m, n) are,

$$\begin{aligned}\varphi_x^{sc} &= m_{\Delta} s_x k_0 \\ &= mp\, k_0 \sin(\theta^{sc}) \cos(\phi^{sc}) \\ &= mp\, \Omega_x^{sc}\,, \end{aligned} \tag{3.12a}$$

$$\begin{aligned}\varphi_y^{sc} &= n_{\Delta} s_y k_0 \\ &= nq\, k_0 \sin(\theta^{sc}) \sin(\phi^{sc}) \\ &= nq\, \Omega_y^{sc}\,, \end{aligned} \tag{3.12b}$$

for the x- and y-direction, respectively. The phase factor of the forcing function can now be written as:

$$\begin{aligned}&\exp(-jmp\,\Omega_x^{sc}) \exp\left(-jnq\,\Omega_y^{sc}\right) = \\ &\exp\left(-j\,\boldsymbol{k}_T^{sc} \cdot \boldsymbol{R}_{m,n}\right),\end{aligned} \tag{3.13}$$

where $\boldsymbol{k}_T^{sc} = \Omega_x^{sc}\boldsymbol{u}_x + \Omega_y^{sc}\boldsymbol{u}_y$. Examination of Eq. (2.39) reveals that, if the forcing function f is quasi periodic then the response of a linear system must also be quasi periodic. Consequently, if the forcing function is quasi periodic, then the field exciting the patch, the electric surface current density residing at the patch, and the scattered field due to the electric surface currents residing at the patches are all quasi periodic and will have the same phase factor. In other words, the derived expression for the phase factor also holds for the forcing function, in this special case. Note that the derived phase factor defines the propagation direction of all of the propagating modes, but only one will match the desired scan angle. In this case the phase factor will achieve this for the $(0, 0)$ mode.

The derivation of the periodic part of the forcing function, f^P, again employs the single-cell analysis. The fact that the small electric dipole has no physical dimensions effectively reduces it to a current source, which is confined to a single point in space. The probe's position is defined by $\boldsymbol{r}_0 = \boldsymbol{r}_{0,T} + z_0\boldsymbol{u}_z$, where $0 < x_0 < p$, $0 < y_0 < q$ and $-d < z_0 < 0$ must hold. The subscript $_0$ denotes that the position is relative to the center patch. The dipole's orientation is aligned with the z-axis, which is, more importantly, perpendicular to the ground plane, as would be the case for the inner conductor of a real probe. Almost any other orientation can be considered impractical, because there would be no room left for the probe's connection to the outside world. Hence the current density is of the form

$$\begin{aligned}\boldsymbol{J}(\boldsymbol{r}) &= \boldsymbol{J}_T(\boldsymbol{r}) + J_z(\boldsymbol{r})\boldsymbol{u}_z \\ &= I_z\, l\, \delta\left(\boldsymbol{r}_T - \boldsymbol{r}_{0,T}\right) \delta(z - z_0)\boldsymbol{u}_z\,,\end{aligned} \tag{3.14}$$

while assuming a vertical dipole, i.e. $\boldsymbol{J}_T(\boldsymbol{r}) = \boldsymbol{0}$. The spatial Fourier transform of $\boldsymbol{J}(\boldsymbol{r})$

is found by employing Eq. (2.2a), i.e.,

$$\begin{aligned}\hat{\boldsymbol{J}}(\boldsymbol{k}_T, z, \omega) &= \int_{-\infty}^{\infty}\int_{-\infty}^{\infty} \boldsymbol{J}(\boldsymbol{r}, \omega) \exp\left(j\,\boldsymbol{k}_T \cdot \boldsymbol{r}_T\right) d\boldsymbol{r}_T \\ &= \int_{-\infty}^{\infty}\int_{-\infty}^{\infty} I_z\, l\, \delta\left(\boldsymbol{r}_T - \boldsymbol{r}_{0,T}\right) \delta(z - z_0) \boldsymbol{u}_z \exp\left(j\,\boldsymbol{k}_T \cdot \boldsymbol{r}_T\right) d\boldsymbol{r}_T \\ &= I_z\, l\, \exp\left(j\,\boldsymbol{k}_T \cdot \boldsymbol{r}_{0,T}\right) \delta(z - z_0) \boldsymbol{u}_z \\ &= \hat{J}_{\mathcal{S},z}\, \delta(z - z_0) \boldsymbol{u}_z\,,\end{aligned} \tag{3.15}$$

where $\hat{J}_{\mathcal{S},z}$ is the z-component of a surface current density and it's orientation is *aligned* with the normal of the surface, $z = z_0$, which is where the surface current density $\hat{J}_{\mathcal{S},z}$ resides. Substitution of Eq. (3.15) in Eq. (2.6) yields

$$\partial_z I^e = -j\omega\varepsilon V^e\,, \tag{3.16a}$$

$$\partial_z V^e = -\frac{\gamma^2}{j\omega\varepsilon}\, I^e + \frac{k_T}{j\omega\varepsilon} \hat{J}_{\mathcal{S},z}\, \delta\left(z - z_0\right)\,, \tag{3.16b}$$

$$\partial_z I^h = -\frac{\gamma^2}{j\omega\mu}\, V^h\,, \tag{3.16c}$$

$$\partial_z V^h = -j\omega\mu I^h\,. \tag{3.16d}$$

Close examination of Eq. (3.16c) and Eq. (3.16d) reveals that these two equations will not yield any solutions that were excited by the source. Consequently, there will be no H-polarization contribution and the analysis can be restricted to the E-polarization contribution. Differentiating Eq. (3.16a) with respect to z and the subsequent substitution of that result in Eq. (3.16b) yields,

$$\partial_z^2 I_1^e - \gamma_1^2 I_1^e = -k_T \hat{J}_{\mathcal{S},z}\, \delta\left(z - z_0\right)\,, \tag{3.17}$$

which holds for layer one. Examination of Eq. (3.17) reveals that the second-order derivative of I_1^e yields a $\delta(z - z_0)$, as a consequence the first-order derivative of I_1^e must yield a step function at $z = z_0$ as does V_1^e, i.e.,

$$\lim_{z \downarrow z_0} \left[V_1^e(z)\right] - \lim_{z \uparrow z_0} \left[V_1^e(z)\right] = \frac{k_T}{j\omega\varepsilon_1} \hat{J}_{\mathcal{S},z}\,, \tag{3.18}$$

which is the boundary condition at the fictitious boundary $z = z_0$ due to the presence of a small electric dipole. The magnetic-field boundary condition is simply,

$$\lim_{z \downarrow z_0} \left[I_1^e(z)\right] - \lim_{z \uparrow z_0} \left[I_1^e(z)\right] = 0\,. \tag{3.19}$$

Dividing layer one into two halves, as depicted in the figure below, makes it possible to

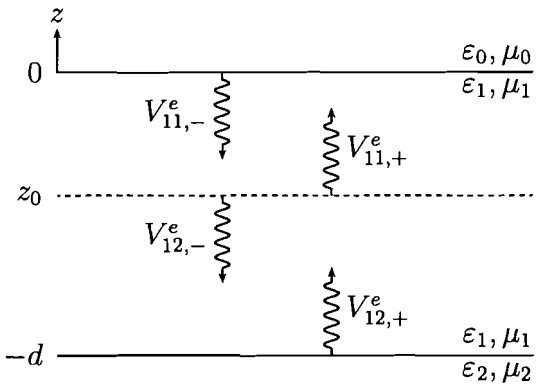

Figure 3.5: Division of layer one into two source-free and piecewise homogeneous halves.

treat the sub-layers as being source free and piecewise homogeneous, while the dipole is treated as a boundary condition at the surface $z = z_0$. The field solutions of the two halves arise from the following two homogeneous differential equations,

$$\partial_z^2 V^e_{11}(z) - \gamma_1^2 V^e_{11}(z) = 0 \quad \text{for} \quad z_0 < z < 0\,, \tag{3.20a}$$

$$\partial_z^2 V^e_{12}(z) - \gamma_1^2 V^e_{12}(z) = 0 \quad \text{for} \quad -d < z < z_0\,, \tag{3.20b}$$

where $\gamma_1 = \sqrt{k_T^2 - \omega\varepsilon_1\mu_1}$. As in Section 2.3 the positive branch of the square root is chosen, i.e., $\Re\{\gamma_1\} \geq 0$ and $\Im\{\gamma_1\} \geq 0$. Note that the equations above are very similar to Eq. (2.8a) and Eq. (2.8b) and have the general solutions:

$$V^e_{11} = V^e_{11,-} \exp(\gamma_1 z) + V^e_{11,+} \exp[-\gamma_1 (z - z_0)]\,, \tag{3.21a}$$

$$V^e_{12} = V^e_{12,-} \exp[\gamma_1 (z - z_0)] + V^e_{12,+} \exp[-\gamma_1 (z + d)]\,, \tag{3.21b}$$

where $V^e_{11,-}$, $V^e_{11,+}$, $V^e_{12,-}$ and $V^e_{12,+}$ are the amplitudes of the upward and downward traveling wave solutions. By employing the magnetic-field boundary condition a relation is established between the wave solutions of the upper and lower sub layers of layer one, i.e.,

$$V^e_{12,-} - V^e_{12,+} \exp[-\gamma_1 (z_0 + d)] = V^e_{11,-} \exp(\gamma_1 z_0) - V^e_{11,+}\,. \tag{3.22}$$

By employing the electric field boundary condition of Eq. (3.18) another relation between the wave solutions of the upper and lower sub layers is established, i.e.,

$$V^e_{11,-} \exp(\gamma_1 z_0) + V^e_{11,+} - V^e_{12,-} - V^e_{12,+} \exp[-\gamma_1 (z_0 + d)] = \frac{k_T}{j\omega\varepsilon_1} \hat{J}_{S,z}\,. \tag{3.23}$$

The interaction of the E-polarization contributions between the half space, $z > 0$, and layer one is characterized by a reflection coefficient, $R^e_{1,0}$. It is defined as the ratio between the scattered and the incident field at the interface $z = 0$, i.e.,

$$R^e_{1,0} = \left.\frac{V^e_{11,-} \exp(\gamma_1 z)}{V^e_{11,+} \exp[-\gamma_1 (z - z_0)]}\right|_{z=0} = \frac{V^e_{11,-}}{V^e_{11,+}} \exp(-\gamma_1 z_0)\,. \tag{3.24}$$

The interaction of the E-polarization contributions between layer one and layer two (and, if present, the rest of the layers) is characterized by another reflection coefficient, viz. $R^e_{1,2}$. It is defined as the ratio between the scattered and the incident field at the interface $z = -d$, i.e.,

$$R^e_{1,2} = \frac{V^e_{12,+}}{V^e_{12,-}} \exp\left[\gamma_1 \left(z_0 + d\right)\right], \tag{3.25}$$

which is in most practical applications equal to -1 due to the ground plane separating layer one and half space below layer one. In Section 2.4 an expression was established, which relates the reflection coefficient, $R^e_{1,2}$, to the material properties of the layer one and layer two. By interchanging the subscript $_2$ to $_0$ a similar expression is obtained for $R^e_{1,0}$, i.e.,

$$R^e_{1,0} = \frac{\varepsilon_1\gamma_0 - \varepsilon_0\gamma_1}{\varepsilon_1\gamma_0 + \varepsilon_0\gamma_1}. \tag{3.26}$$

Rewriting Eq. (3.24) and Eq. (3.25) yields two expressions,

$$V^e_{11,-} = V^e_{11,+} R^e_{1,0} \exp\left(\gamma_1 z_0\right), \tag{3.27a}$$

$$V^e_{12,+} = V^e_{12,-} R^e_{1,2} \exp\left[-\gamma_1 \left(z_0 + d\right)\right]. \tag{3.27b}$$

which effectively relate $V^e_{11,-}$ to $V^e_{11,+}$ and $V^e_{12,+}$ to $V^e_{12,-}$, respectively. By employing these two relations Eq. (3.22) and Eq. (3.23) reduce to,

$$V^e_{11,+}\left[R^e_{1,0}\exp\left(2\gamma_1 z_0\right) + 1\right] - V^e_{12,-}\left\{1 + R^e_{1,2}\exp\left[-2\gamma_1\left(z_0 + d\right)\right]\right\} = \frac{k_T}{j\omega\varepsilon_1}\hat{J}_{S,z}, \tag{3.28a}$$

$$V^e_{12,-}\left\{1 - R^e_{1,2}\exp\left[-2\gamma_1\left(z_0 + d\right)\right]\right\} - V^e_{11,+}\left[R^e_{1,0}\exp\left(2\gamma_1 z_0\right) - 1\right] = 0. \tag{3.28b}$$

Substitution of Eq. (3.28b) in Eq. (3.28a) yields,

$$V^e_{11,+} = \hat{J}_{S,z}\frac{k_T}{j2\omega\varepsilon_1}\frac{1 - R^e_{1,2}\exp\left[-2\gamma_1\left(z_0 + d\right)\right]}{1 - R^e_{1,0}R^e_{1,2}\exp\left(-2\gamma_1 d\right)}. \tag{3.29}$$

By employing once more the relation found in Eq. (3.27a) an expression is found for $V^e_{11,-}$. Substitution of the expression for $V^e_{11,-}$ and Eq. (3.29) in Eq. (3.21a) for $z = 0$ yields

$$V^e_{11}(z=0) = \hat{J}_{S,z}\frac{k_T}{2j\omega\varepsilon_1}\frac{1 - R^e_{1,2}\exp\left[-2\gamma_1\left(z_0 + d\right)\right]}{1 - R^e_{1,0}R^e_{1,2}\exp\left(-2\gamma_1 d\right)}\left(1 + R^e_{1,0}\right)\exp\left(\gamma_1 z_0\right), \tag{3.30}$$

which is proportional to the $\boldsymbol{u}_k$ term of $\hat{\boldsymbol{E}}^i_T$. Substitution of Eq. (3.30) in Eq. (2.5a) yields the spatial-Fourier transform of the forcing function $\boldsymbol{E}^i_T(z=0)$, i.e.,

$$\hat{\boldsymbol{E}}^i_T(z=0) = j\boldsymbol{k}_T\,\hat{J}_{S,z}\frac{1}{2j\omega\varepsilon_1}\frac{1 - R^e_{1,2}\exp\left[-2\gamma_1\left(z_0 + d\right)\right]}{1 - R^e_{1,0}R^e_{1,2}\exp\left(-2\gamma_1 d\right)}\left(1 + R^e_{1,0}\right)\exp\left(\gamma_1 z_0\right). \tag{3.31}$$

By employing the inverse spatial-Fourier transformation, as defined in Eq. (2.2b), the equation above can be written in a convolutional structure, i.e.,

$$\boldsymbol{E}^i_T(z=0) = \boldsymbol{\nabla}_T \iint_{\mathcal{P}} G_3\left(\boldsymbol{r}_T - \boldsymbol{r}'_T\right) J_{S,z}\left(\boldsymbol{r}'_T\right) d\boldsymbol{r}'_T, \tag{3.32}$$

where $\mathcal{P}$ denotes the surface, $z = z_0$, at which the source resides and $G_3(\boldsymbol{r}_T)$ denotes a Green's function, which is defined as,

$$G_3(\boldsymbol{r}_T) = \frac{1}{4\pi^2} \int_{-\infty}^{\infty} \int_{-\infty}^{\infty} \frac{1}{2j\omega\varepsilon_1} \frac{1 - R^e_{1,2} \exp\left[-2\gamma_1 \left(z_0 + d\right)\right]}{1 - R^e_{1,0} R^e_{1,2} \exp\left(-2\gamma_1 d\right)} \left(1 + R^e_{1,0}\right) \exp\left(\gamma_1 z_0\right) \times \exp\left(-j\boldsymbol{k}_T \cdot \boldsymbol{r}_T\right) d\boldsymbol{k}_T \,. \tag{3.33}$$

Note that Eq. (3.32) is a result of the single-cell analysis. However, its convolutional structure allows for the employment of the same analysis as used in Section 2.5, which expands it to a solution for the infinite-array model. This yields,

$$\boldsymbol{E}^i_T(z = 0) = \frac{1}{p\,q} \sum_m \sum_n j\boldsymbol{k}^{m,n}_T \hat{G}_3 \hat{J}^0_{\mathcal{S},z} \exp\left(-j\boldsymbol{k}^{m,n}_T \cdot \boldsymbol{r}_T\right), \tag{3.34}$$

where $\boldsymbol{k}^{m,n}_T = 2\pi m/q\,\boldsymbol{u}_x + 2\pi n/q\,\boldsymbol{u}_y + \boldsymbol{k}^{sc}_T$ and $\hat{J}^0_{\mathcal{S},z} = I_z l \exp\left(j\boldsymbol{k}^{m,n}_T \cdot \boldsymbol{r}_{0,T}\right)$. This concludes the derivation of the forcing function for the dipole-excitation case.

Chapter 4

Far Field

4.1 Field regions

The field radiated by the infinite array can be seen as a superposition of two fields, i.e., a field due to the currents on the patches and a field due to the source in absence of the patches. Note that the exact same superposition was proposed earlier for the entire field in Chapter 3 and is depicted in Figure 3.2. An observer positioned at a large enough distance, R, from the array will experience the remnants of this field, which is often called the far field. This situation is depicted in Figure 4.1 in case of a simple dipole

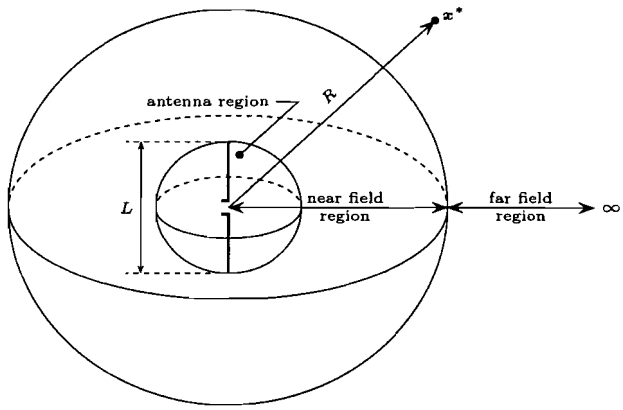

Figure 4.1: The different field regions, in case of a simple dipole antenna with a maximum dimension L and where R denotes the distance from the antenna to the observation point, $\boldsymbol{x}^*$.

antenna. The far field is composed of the same superposition and the expressions that describe them are derived separately in the two remaining sections of this chapter. The properties of the far field are generally considered to be a good measure of the antenna's

performance under operating conditions, which is why they are used as objectives for the optimization tool in Chapter 5. But before the properties of the far field can be utilized one matter remains, viz., the classification of the near and far field regions. As mentioned before, the far field region starts at a large enough distance from the source, but a 'large enough distance' is a somewhat vague measure and in practice a rule-of-thumb is applied, e.g., ten times the wavelength. Another more sophisticated way of classifying the field regions [20] employs the inequality below,

$$R > \frac{2L^2}{\lambda_0}, \tag{4.1}$$

where L denotes the largest physical dimension of the radiating element and λ_0 is the wavelength of the radiated wave. In this case Eq. (4.1) is not meaningful, because of the model's infinite extent in the horizontal plane. Instead the height of the observation point above the surface of the array will be used as a measure of distance, but this does not address the 'large enough' issue. Fortunately, an analytic expression of the radiated field will be available after the derivations made in Section 4.2 and 4.3 of this chapter, which allows for an exact way of identifying the near and far field. The near field will consist of both propagating and evanescent modes. On the other hand, the far field will only consist of propagating modes, because the evanescent modes are attenuated exponentially as the distance between the source and the observation point increases and consequently no significant part will contribute to the far field. An expression for the tangential part of the radiated electric field at $z = 0$ due to the currents on the patches was already derived in Section 2.5. The fact that the radiated field should vanish or propagate in the positive z-direction is used to establish an expression for $\hat{\boldsymbol{E}}_T^s$, which holds for $z \geq 0$, i.e.,

$$\hat{\boldsymbol{E}}_T^s(\boldsymbol{k}_T, z) = \hat{\boldsymbol{E}}_T^s(\boldsymbol{k}_T, 0) \exp\left(-\gamma_0 z\right), \tag{4.2}$$

where $\gamma_0 = \sqrt{k_T^2 - w^2\varepsilon_0\mu_0}$. Substitution of the equation above in Eq. (2.21) and subsequent employment of the same analysis as performed previously in Section 2.5 yields,

$$\boldsymbol{E}_T^s = \frac{1}{p\,q} \sum_m \sum_n \left[\boldsymbol{k}_T^{m,n} \hat{G}_1 \left(\boldsymbol{k}_T^{m,n} \cdot \hat{\boldsymbol{J}}_S^0\right) + \hat{G}_2 \hat{\boldsymbol{J}}_S^0\right] \exp\left(-\gamma_0 z\right) \exp\left(-j\boldsymbol{k}_T^{m,n} \cdot \boldsymbol{r}_T\right) \tag{4.3}$$

where $\hat{G}_1$, $\hat{G}_2$ and γ_0 are functions of $k_T^{m,n}$ and $\hat{\boldsymbol{J}}_S^0$ is a function of $\boldsymbol{k}_T^{m,n}$. Close examination of Eq. (4.3) reveals that $\boldsymbol{E}_T^s$ is composed of an infinite number of so-called Floquet modes. A mode is called a propagating mode if the argument of the exponent, $\exp(-\gamma_0 z)$, is purely imaginary or if it is equal to zero. A mode is called an evanescent mode if the argument is real valued and negative. The denotation becomes obvious when observing the fact that each mode represents a plane wave. Consequently, the following must hold for all propagating modes,

$$\left(k_x^m\right)^2 + \left(k_y^n\right)^2 < \omega^2\varepsilon_0\mu_0, \tag{4.4}$$

which describes a circular area in the $\boldsymbol{k}_T$ domain, with a radius $k_0 = \omega\sqrt{\varepsilon_0\mu_0}$ as depicted in Figure 4.2. In other words, all propagating modes belong to the encircled area. Note

that Eq. (4.4) does not hold for propagating modes for which $\gamma_0 = 0$. As they propagate they move along the surface of the array, which means that their Poynting vector will not have a z-component and as such they will not contribute to the far field. Eq. (2.3)

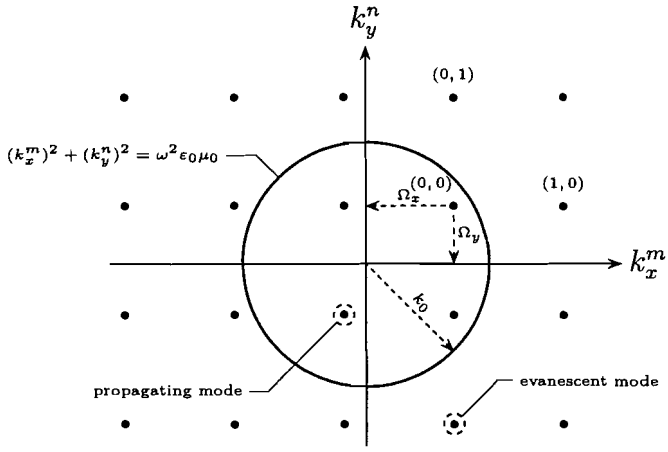

Figure 4.2: Propagating and evanescent modes.

shows that $\hat{\boldsymbol{H}}_T^s$, $\hat{H}_z^s$ and $\hat{E}_z^s$ are proportional to $\hat{\boldsymbol{E}}_T^s$ or proportional to its derivative with respect to z. This effectively means that all the components of the radiated field due to the currents on the patches consist of identical propagating and evanescent modes. Furthermore, the result of Section 2.5 shows that the field exciting the patches, the current distribution at the patches and the field radiated by these currents all have an identical phase variation. Consequently, the radiated field due to the source in absence of the patches has the same phase variation and therefore potentially the same propagating and evanescent modes. In effect the analysis made in this section holds for both parts of the far field and consequently for the far field as a whole. Note that the analysis in this report is restricted to configurations where only a single propagating mode is excited, viz. (0,0)-mode.

4.2 Radiation due to currents on the patches

In this section the situation as depicted in Figure 3.2b is considered, i.e. radiating current distribution on the patches, in absence of the source that excites the current distribution. As in Chapter 2, the analysis is performed for a unit cell positioned in an infinite dielectric medium, as depicted in Figure 2.2b, and subsequently, the periodicity of the array is employed to expand the single-cell solution to a solution for the infinite-array model.

The field that is radiated by the electric surface current density, which resides at the patches, is split into tangential and longitudinal components, i.e.,

$$\boldsymbol{E}^s = \boldsymbol{E}^s_T + E^s_z \boldsymbol{u}_z \,, \tag{4.5a}$$

$$\boldsymbol{H}^s = \boldsymbol{H}^s_T + H^s_z \boldsymbol{u}_z \,. \tag{4.5b}$$

As mentioned before, Eq. (2.3) relates the tangential and longitudinal components to each other. Consequently, the expression for $\boldsymbol{E}^s_T$ in Eq. (4.3) completely characterizes the radiated field due to the currents on the patches. However, very often E^s_r, E^s_θ, and E^s_ϕ are used to describe the far field or one of its properties. By applying a standard coordinate transformation E^s_r, E^s_θ, and E^s_ϕ can be expressed in terms of their Cartesian counterparts E^s_x, E^s_y, and E^s_z, i.e.,

$$E^s_r = E^s_x \sin\theta\cos\phi + E^s_y \sin\theta\sin\phi + E^s_z \cos\theta \,, \tag{4.6a}$$

$$E^s_\theta = E^s_x \cos\theta\cos\phi + E^s_y \cos\theta\sin\phi - E^s_z \sin\theta \,, \tag{4.6b}$$

$$E^s_\phi = -E^s_x \sin\phi + E^s_y \cos\phi \,, \tag{4.6c}$$

where (θ, ϕ) determines the observation angle. Note that the same definitions for θ and ϕ were used as in Chapter 3. The longitudinal component of the field, E^s_z, is still undetermined, but Eq. (2.3a) together with Eq. (2.4b) show that E^s_z and $\boldsymbol{E}^s_T$ are coupled. By reusing the decomposition as proposed in Eq. (2.5b), $\hat{\boldsymbol{H}}^s_T$ can be written in terms of E- and H-polarization contributions, which are denoted by the superscripts ^{e} and ^{h}, respectively, i.e.,

$$\hat{\boldsymbol{H}}^s_T = j\boldsymbol{u}_k I^h(z) + \boldsymbol{u}_z \times j\boldsymbol{u}_k I^e(z) \,. \tag{4.7}$$

Substitution of the equation above in Eq. (2.3a) yields,

$$\hat{E}^s_z = -\hat{J}_z - \frac{k_T}{j\omega\varepsilon} I^e \,. \tag{4.8}$$

Using the fact that the surface current density has no z-component reduces the equation above to,

$$\hat{E}^s_z = -\frac{k_T}{j\omega\varepsilon} I^e \,, \tag{4.9}$$

where I^e can be expressed in terms of $\partial_z V^e$ by applying Eq. (2.7d), i.e.,

$$\hat{E}^s_z = \frac{k_T}{\gamma^2} \partial_z V^e \,, \tag{4.10}$$

where $V^e(z) = V^e_0(z) = V^e_{0,+} \exp(-\gamma_0 z)$ for the half plane $z > 0$. The subsequent substitution of $V^e = V^e_{0,+} \exp(-\gamma_0 z)$ in Eq. (4.10) yields,

$$\hat{E}^s_z = -\frac{k_T}{\gamma_0} V^e_{0,+} \exp(-\gamma_0 z) \,, \tag{4.11}$$

Employing Eq. (2.5a) and Eq. (2.9a) yields,

$$\hat{E}_z^s = \frac{j\,\boldsymbol{k}_T \cdot \hat{\boldsymbol{E}}_T^s}{\gamma_0}\,, \tag{4.12}$$

which effectively establishes a relation between E_z^s and $\boldsymbol{E}_T^s$. For $V_{0,+}^e$ an expression was already obtained in Section 2.3. Substitution of Eq. (2.19) in Eq. (4.11) yields,

$$\hat{E}_z^s(\boldsymbol{k}_T, z) = -\frac{A(k_T)}{\gamma_0}\, j\,\boldsymbol{k}_T \cdot \hat{\boldsymbol{J}}_S \exp\left(-\gamma_0 z\right), \tag{4.13}$$

where $A(k_T)$ is given in Eq. (2.19). By employing the inverse spatial-Fourier transformation, as defined in Eq. (2.2b), the equation above can be written as a convolution, i.e.,

$$E_z^s(\boldsymbol{r}) = \boldsymbol{\nabla}_T \cdot \iint\limits_{\mathcal{P}} G_4\left(\boldsymbol{r}_T - \boldsymbol{r}_T'\right) \boldsymbol{J}_S\left(\boldsymbol{r}_T'\right)\, d\boldsymbol{r}_T'\,, \tag{4.14}$$

where $\mathcal{P}$ denotes the surface at which the surface current density $\boldsymbol{J}_S$ resides and $G_4\left(\boldsymbol{r}_T\right)$ denotes a Green's function, which is defined as,

$$\begin{aligned} G_4\left(\boldsymbol{r}_T\right) &= -\frac{1}{4\pi^2} \int_{-\infty}^{\infty}\int_{-\infty}^{\infty} \frac{A(k_T)}{\gamma_0} \exp\left(-\gamma_0 z\right) \exp\left(-j\boldsymbol{k}_T \cdot \boldsymbol{r}_T\right) d\boldsymbol{k}_T \\ &= -\frac{1}{4\pi^2} \int_{-\infty}^{\infty}\int_{-\infty}^{\infty} \frac{k_T^2 \hat{G}_1 + \hat{G}_2}{\gamma_0} \exp\left(-\gamma_0 z\right) \exp\left(-j\boldsymbol{k}_T \cdot \boldsymbol{r}_T\right) d\boldsymbol{k}_T\,. \end{aligned} \tag{4.15}$$

Note that Eq. (4.14) holds only for the single-cell configuration as depicted in Figure 2.2b. However, its convolutional structure allows for the employment of the analysis as used in Section 2.5. The analysis of Section 2.5 effectively expands the single-cell solution to a solution for the infinite-array model. Employing the analysis yields,

$$E_z^s(\boldsymbol{r}) = -\frac{1}{p\,q} \sum_m \sum_n \frac{\left(k_T^{m,n}\right)^2 \hat{G}_1 + \hat{G}_2}{\gamma_0}\, j\,\boldsymbol{k}_T^{m,n} \cdot \hat{\boldsymbol{J}}_S^0 \exp\left(-\gamma_0 z\right) \exp\left(-j\boldsymbol{k}_T^{m,n} \cdot \boldsymbol{r}_T\right), \tag{4.16}$$

where $\hat{G}_1$, $\hat{G}_2$, and γ_0 are functions of $k_T^{m,n}$ and $\hat{\boldsymbol{J}}_S^0$ is a function of $\boldsymbol{k}_T^{m,n}$. As mentioned in the previous section, only the propagating modes will reach the far-field region. This effectively reduces the sum over all modes, in Eq. (4.3) and Eq. (4.16), to the sum over all propagating modes (p.m.), i.e.,

$$\boldsymbol{E}_T^s(\boldsymbol{r}) = \frac{1}{p\,q} \sum_{\text{p.m.}} \left[\boldsymbol{k}_T^{m,n} \hat{G}_1 \left(\boldsymbol{k}_T^{m,n} \cdot \hat{\boldsymbol{J}}_S^0\right) + \hat{G}_2 \hat{\boldsymbol{J}}_S^0\right] \exp\left(-\gamma_0 z\right) \exp\left(-j\boldsymbol{k}_T^{m,n} \cdot \boldsymbol{r}_T\right), \tag{4.17a}$$

$$E_z^s(\boldsymbol{r}) = -\frac{1}{p\,q} \sum_{\text{p.m.}} \frac{\left(k_T^{m,n}\right)^2 \hat{G}_1 + \hat{G}_2}{j\gamma_0}\, j\,\boldsymbol{k}_T^{m,n} \cdot \hat{\boldsymbol{J}}_S^0 \exp\left(-\gamma_0 z\right) \exp\left(-j\boldsymbol{k}_T^{m,n} \cdot \boldsymbol{r}_T\right). \tag{4.17b}$$

In case of plane-wave excitation the configuration of the infinite-array model is chosen in such a manner that only one propagating mode will be excited. This effectively reduces the sum over all propagating modes to a single mode. As mentioned before in Section 4.1, the far field is composed of a set of plane waves, where each plane wave corresponds to one of the propagating modes. If each plane wave is evaluated in spherical components and the observation angle (θ, ϕ) is chosen to correspond with the propagation direction of the plane wave, then evidently $E_r^s = 0$. This reduces the number of far-field components, which reduces the number of unknowns by one and in turn reduces the computation time needed to evaluate a single configuration.

4.3 The directly scattered field

The situation under consideration in this section is the one depicted in Figure 3.2a for the incident-plane-wave-excitation case, i.e., scattering of the field that is radiated by the source, in absence of the patches. The scattered field $(\boldsymbol{E}^s, \boldsymbol{H}^s)$ denotes the field that is radiated into the half plane $z > 0$. For both excitation cases an expression for the scattered electric field is derived. If needed then the scattered magnetic field can be computed form the obtained scattered electric field components. The scattered electric field is split into tangential and longitudinal field components, i.e.,

$$\boldsymbol{E}^s = \boldsymbol{E}_T^s + E_z^s \boldsymbol{u}_z \,, \tag{4.18}$$

where the longitudinal field component, E_z^s, is related to $\boldsymbol{E}_T^s$ by their spatial-Fourier transforms, see Eq. (4.12). The spatial-Fourier transform of the tangential field component is expressed in E- and H-polarization contributions, by employing Eq. (2.5a) and Eq. (2.9a), i.e.,

$$\hat{\boldsymbol{E}}_T^s(z) = \left(j\boldsymbol{u}_k V_{0,+}^e - \boldsymbol{u}_z \times j\boldsymbol{u}_k V_{0,+}^h\right) \exp\left(-\gamma_0 z\right). \tag{4.19}$$

In Chapter 3 two expressions for the tangential part of the incident electric field, $\boldsymbol{E}_T^i$, are derived, one for each excitation case. For the plane-wave-excitation case an expression for $\hat{\boldsymbol{E}}_T^i$ is given in Eq. (3.9). Closer examination of this equation shows that $\hat{\boldsymbol{E}}_T^i$ consists of the field impressed by the incident plane wave and the reflections due to the presence of the stratified medium. Subsequent employment of Eq. (2.5a) and Eq. (2.9a) establishes the following expression for $\hat{\boldsymbol{E}}_T^i$,

$$\hat{\boldsymbol{E}}_T^i(z=0) = j\boldsymbol{u}_k \left(V_{0,-}^e + V_{0,+}^e\right) - \boldsymbol{u}_z \times j\boldsymbol{u}_k \left(V_{0,-}^h + V_{0,+}^h\right) \,, \tag{4.20}$$

where $V_{0,-}^e$, $V_{0,-}^h$ denote the impressed fields and $V_{0,+^e}$, $V_{0,+}^h$ the scattered fields due to the presence of the stratified medium. Subtraction of the impressed fields results in a expression for the spatial-Fourier transform of the scattered electric field $\hat{\boldsymbol{E}}_T^s$, i.e.,

$$\hat{\boldsymbol{E}}_T^s(z) = \left(j\boldsymbol{u}_k V_{0,-}^e R_{0,1}^e - \boldsymbol{u}_z \times j\boldsymbol{u}_k V_{0,-}^h R_{0,1}^h\right) \exp\left(-\gamma_0 z\right), \tag{4.21}$$

where two new reflection coefficients have been introduced for the E- and H-polarization contribution, viz.,

$$R^e_{0,1} = \frac{\gamma_1\varepsilon_0\left[1 + R^e_{1,2}\exp\left(-2\gamma_1 d\right)\right] - \gamma_0\varepsilon_1\left[1 - R^e_{1,2}\exp\left(-2\gamma_1 d\right)\right]}{\gamma_1\varepsilon_0\left[1 + R^e_{1,2}\exp\left(-2\gamma_1 d\right)\right] + \gamma_0\varepsilon_1\left[1 - R^e_{1,2}\exp\left(-2\gamma_1 d\right)\right]}, \tag{4.22a}$$

$$R^h_{0,1} = \frac{\gamma_0\mu_1\left[1 + R^h_{1,2}\exp\left(-2\gamma_1 d\right)\right] - \gamma_1\mu_0\left[1 - R^h_{1,2}\exp\left(-2\gamma_1 d\right)\right]}{\gamma_0\mu_1\left[1 + R^h_{1,2}\exp\left(-2\gamma_1 d\right)\right] + \gamma_1\mu_0\left[1 - R^h_{1,2}\exp\left(-2\gamma_1 d\right)\right]}. \tag{4.22b}$$

The substitution of Eq. (4.21) in Eq. (4.12) yields an expression for the longitudinal scattered field component, i.e.,

$$\hat{E}^s_z = -\frac{k_T}{\gamma_0} V^e_{0,-} R^e_{0,1}\exp\left(-\gamma_0 z\right). \tag{4.23}$$

Note that $V^e_{0,-}$ and $V^h_{0,-}$ are the $\boldsymbol{u}_k$ and $\boldsymbol{u}_z \times \boldsymbol{u}_k$ components of the incident plane wave and are therefore known. Employing the fact that the incident plane wave will only excite one mode of the infinite-array model establishes a relation for $\boldsymbol{E}^s_T$ and E^s_z, i.e.,

$$\boldsymbol{E}^s_T = \left(j\boldsymbol{u}_k V^e_{0,-} R^e_{0,1} - \boldsymbol{u}_z \times j\boldsymbol{u}_k V^h_{0,-} R^h_{0,1}\right)\exp\left(-\gamma_0 z\right)\exp\left(-j\boldsymbol{k}^i_T \cdot \boldsymbol{r}_T\right), \tag{4.24a}$$

$$E^s_z = -\frac{k^i_T}{\gamma_0} V^e_{0,-} R^e_{0,1}\exp\left(-\gamma_0 z\right)\exp\left(-j\boldsymbol{k}^i_T \cdot \boldsymbol{r}_T\right), \tag{4.24b}$$

where $R^e_{0,1}$, $R^h_{0,1}$, and γ_0 are all functions of k^i_T. Note that the $(0,0)$-mode is always a propagating mode and will therefore contribute to the far field for nearly all situations. Exceptions arise for angles of incidence where the reflection grazes the array's surface. This concludes the derivation of the scattered field due to the source in absence of the patches for the incident-plane-wave-excitation case.

In case of excitation by dipoles situated underneath the patches, the expression for $\hat{\boldsymbol{E}}^i_T$ is given in Eq. (3.31). Closer examination of this equation shows that in this case $\hat{\boldsymbol{E}}^i_T$ denotes the tangential part of the field that is transmitted in the half plane $z > 0$. Employing this fact and subsequently using Eq. (4.2) establishes an expression for the tangential part of the scattered field, i.e.,

$$\hat{\boldsymbol{E}}^s_T(z) = \boldsymbol{u}_k\, \hat{J}_{\mathcal{S},z}\, \hat{G}_3\exp\left(-\gamma_0 z\right), \tag{4.25}$$

where $\hat{G}_3$ is the spatial-Fourier transform of the Green's function, G_3, which was defined previously in Chapter 3 Eq. (3.33). Substitution of Eq. (4.25) in Eq. (4.12) yields,

$$\hat{E}^s_z(z) = \hat{J}_{\mathcal{S},z}\frac{jk_T}{\gamma_0}\hat{G}_3\exp\left(-\gamma_0 z\right). \tag{4.26}$$

The quasi periodicity of the dipole currents enables the use of the analysis as employed in Section 2.5, to expand the single-cell solution, as presented in Eq. (4.25) and Eq. (4.26),

to a solution for the infinite-array model, i.e,

$$\boldsymbol{E}_T^s(\boldsymbol{r}) = -\frac{1}{p\,q}\sum_m\sum_n \boldsymbol{u}_k^{m,n}\,\hat{J}_{S,z}^0\,\hat{G}_3\exp\left(-\gamma_0 z\right)\exp\left(-j\boldsymbol{k}_T^{m,n}\cdot\boldsymbol{r}_T\right), \tag{4.27a}$$

$$E_z^s(\boldsymbol{r}) = \frac{1}{jp\,q}\sum_m\sum_n \hat{J}_{S,z}^0\frac{k_T^{m,n}}{\gamma_0}\,\hat{G}_3\exp\left(-\gamma_0 z\right)\exp\left(-j\boldsymbol{k}_T^{m,n}\cdot\boldsymbol{r}_T\right), \tag{4.27b}$$

where $\hat{G}_3$ and γ_0 are functions of $k_T^{m,n}$ and where $\hat{J}_{S,z}^0 = I_z\,l\exp\left(j\boldsymbol{k}_T^{m,n}\cdot\boldsymbol{r}_{0,T}\right)$. The far field will only consist of propagating modes as mentioned before in Section 4.1. This reduces the summation over all modes (m,n) to a summation over all propagating modes (p.m.), i.e.,

$$\boldsymbol{E}_T^s(\boldsymbol{r}) = -\frac{1}{p\,q}\sum_{\text{p.m.}} \boldsymbol{u}_k^{m,n}\,\hat{J}_{S,z}^0\,\hat{G}_3\exp\left(-\gamma_0 z\right)\exp\left(-j\boldsymbol{k}_T^{m,n}\cdot\boldsymbol{r}_T\right), \tag{4.28a}$$

$$E_z^s(\boldsymbol{r}) = \frac{1}{j\,p\,q}\sum_{\text{p.m.}} \hat{J}_{S,z}^0\frac{k_T^{m,n}}{\gamma_0}\,\hat{G}_3\exp\left(-\gamma_0 z\right)\exp\left(-j\boldsymbol{k}_T^{m,n}\cdot\boldsymbol{r}_T\right), \tag{4.28b}$$

which concludes the derivation of the scattered field due to dipoles situated underneath the surface $z = 0$, while considering the same dielectric medium in absence of the patches.

4.4 Numerical verification

In the previous two sections the two parts that contribute to the far field have been derived. By employing these expressions the far field can be determined for each of the two excitation cases. The simulation data was tested against data obtained from [10] for the plane-wave-excitation case. Note that the obtained data had to be gathered from the figures in the paper due to the lack of data tables. For the dipole excitation no appropriate simulation data was found to test the far field expressions. The methods used in the above paper are similar to the ones employed in this report.

In total the results of five simulations of reflection coefficients were tested against data obtained from the paper. In all the graphs the data points obtained from the paper are denoted by an open bullet (○). The first three simulations determine the reflection coefficient of a frequency-selective surface (FSS) with square patches, while the angle of incidence and the observation angle are both perpendicular to the surface of the array, i.e., $\theta^i = \theta = 0$. The side length of the square patch is 1 cm, the length of the single cell, which is also square, is 2 cm. The three simulations represent three variations of the thickness of the dielectric layer. The first simulation is performed in absence of a dielectric layer, the other two are performed with a single dielectric layer present, which has a thickness, d, equal to 0.1 cm and 0.2 cm, respectively. The material properties of layer one are constant for all three simulations, where $\varepsilon_r = 3.5$ and $\mu_r = 1$.

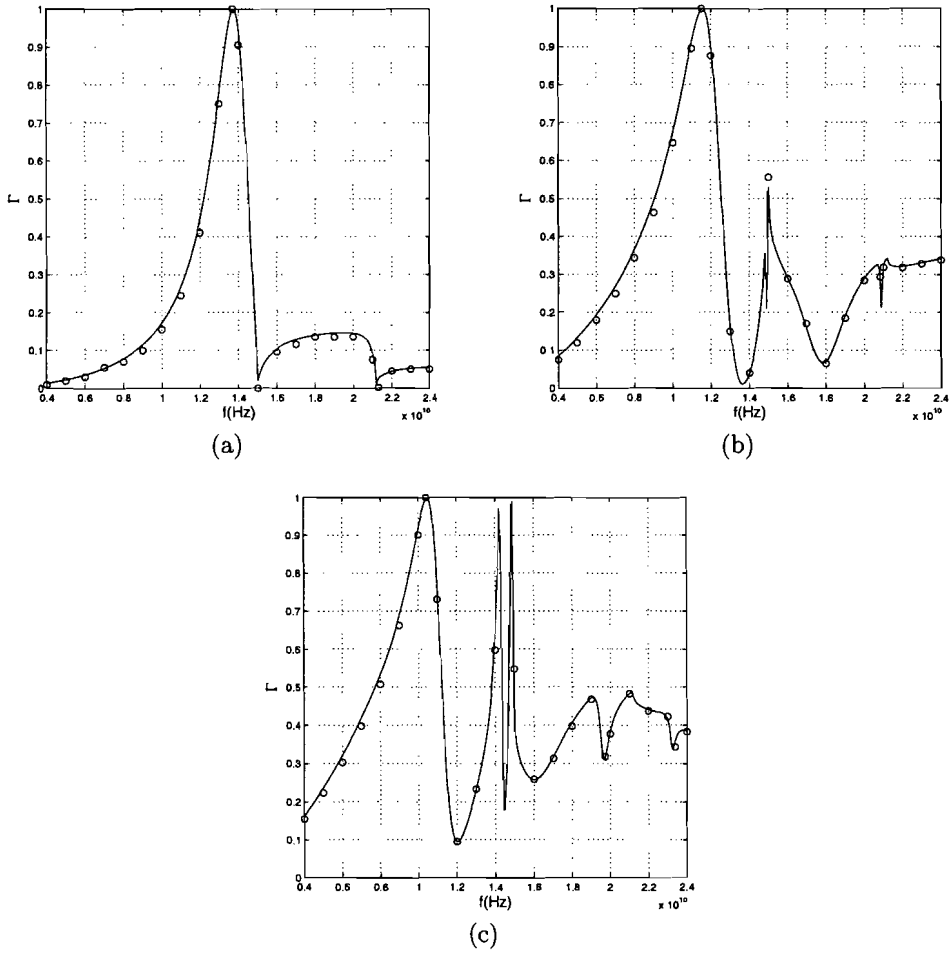

Figure 4.3: Reflection coefficient, Γ, vs. frequency, f, for a frequency-selective surface(FSS) with a dielectric layer thickness (a) $d = 0$ cm, (b) $d = 0.1$ cm and (c) $d = 0.2$ cm

For all three simulations the frequency is swept from 4 to 24 GHz and their results are depicted in Figure 4.3. Note that all three graphs show a good agreement between the two sets of data, with the exception of a few small deviations, which are probably caused by the fact that the data was extracted manually from the figures in the paper.

The other two simulations consider the reflection coefficient of a FSS with circular patches. This poses an extra difficulty, because the patches are modeled by rectangular cells. As a consequence the circular patches can only be approximated. The resulting staircase approximation is depicted in Figure 4.4, where a top view of a unit cell of the FSS is shown for the case of 15×15 square cells. The dimensions of the single cell have been kept the same as for the previous three simulations. The cross section or diameter, D, of the circular patch is 1.25 cm. For both simulations the angle of incidence is swept from $\theta^i = 0°$ to $\theta^i = 90°$, where ϕ^i is kept constant at 0°. The observation angle is

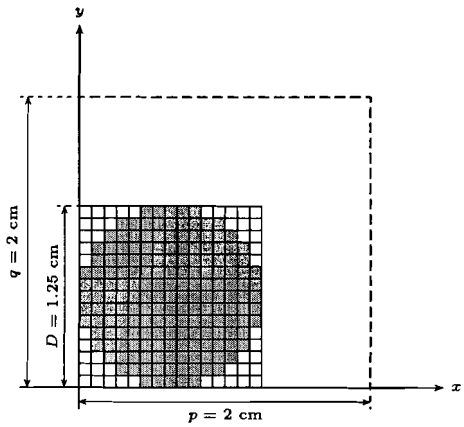

Figure 4.4: Top view of a unit cell with an approximately circular patch (15 × 15 cells), where the light gray denotes the presence of a conductor.

swept synchronously, i.e. ($\theta = \theta^i, \phi = 180°$), which is often referred to as a monostatic setup. The frequency is held constant at 10.4 GHz and the dielectric has a thickness $d = 0.2$ cm and its $\varepsilon_r = 3.5$. The circular patch in the first simulation is excited by an incident transverse-electric (TE) wave, in the second simulation the excitation by an incident transverse-magnetic (TM) wave is considered. For both situations the definitions of the paper [10] were employed. Projection of these field definitions on the surface of the array yields the appropriate expression for the tangential part of the incident electric field, i.e.,

$$\text{TE case:} \quad \boldsymbol{E}_T^i = \boldsymbol{u}_z \times \boldsymbol{u}_k \, E_0 \,, \tag{4.29a}$$

$$\text{TM case:} \quad \boldsymbol{E}_T^i = \boldsymbol{u}_k \, E_0 \cos\left(\theta^i\right) , \tag{4.29b}$$

where E_0 denotes the complex amplitude of the incident electric field. The resulting data is depicted in Figure 4.5a and in Figure 4.5b. Again, both graphs show a good agreement between the two sets of data. Additional simulations with a different number of rectangular cells, which approximate the circular shape of the patch, show that this parameter has quite a bit of influence on the simulation results, as does the number of modes that were employed to construct the Green's functions G_1 and G_2. The influence of both parameters is illustrated in Figure 4.6, where the incident TE-wave case as depicted in Figure 4.5a was recalculated for two variations. The solid line denotes the original situation with 15×15 cells and only 21 modes per dimension, the dashed line denotes the result obtained by increasing the number of modes to 101 per dimension and the dash-dot line denotes the additional increase of the number of rectangular cells to 31×31. Note that both variations should theoretically improve the accuracy of the results. These kinds of problems can probably be avoided by employing of a differently shaped test function that fits the circular shape better.

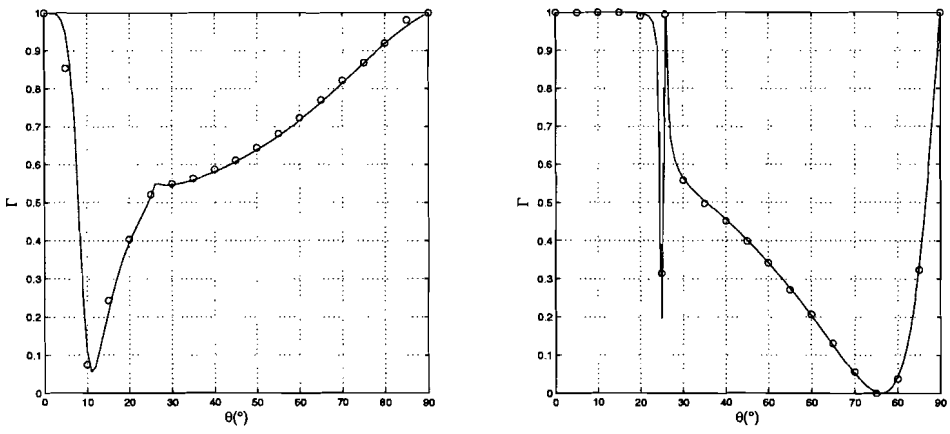

Figure 4.5: Reflection coefficient, Γ, vs. θ^i for a FSS with circular patches excited by (a) an incident TE wave; (b) an incident TM wave.

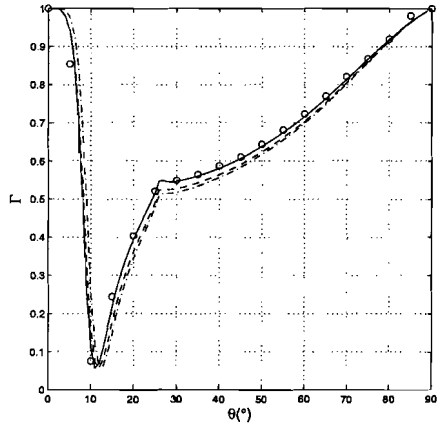

Figure 4.6: Reflection coefficient, Γ, vs. θ^i for a FSS with circular patches excited by an incident TE wave for three configurations, solid line: 15×15 cells and 21 modes per dimension, dashed line: 15×15 cells and 101 modes per dimension, dash-dot line: 31×31 cells and 101 modes per dimension.

Chapter 5

Optimal parameters

5.1 Setting goals

The performance of a patch-antenna array, or more generally an antenna, is related to its application. However for wireless applications that incorporate (patch-) antenna arrays a number of common goals can be identified. Two common goals are: maximum efficiency of the antenna and polarization of the radiated field. Maximum efficiency means the ability of the antenna to radiate as much of the supplied electromagnetic energy as possible for a given frequency range. For a particular application a certain type of polarization can be advantageous, e.g., linear polarization is often applied in radar applications to reduce ground or sea reflections, and circular polarization is applied in satellite communications to enable position-independent radio reception and to reduce the effect of the additional polarization due to raindrops. Naturally, the list with common goals does not end here, but the reader should note that the employment of the infinite-array model excited by small electric dipoles, as described previously, imposes some restrictions. An example would be an expression like: 'a low side lobe level', which loses its meaning due to the infinite extent of the employed model, which forces plane wave solutions.

The electromagnetic behavior of a patch-antenna array can be modified by modifying its design parameters (length and width of the patch, permittivity, probe position, etc.) or even the patch shape. Evaluation of a parameter set will be performed by means of simulation. A comparison of two realizations can be achieved by constructing a measure in the form of a function, the so-called objective function. The objective function will be constructed in such a manner that it will return a value, which reflects the distance between the realized behavior and the desired behavior. Minimizing the objective function will therefore become equivalent to searching for an optimal parameter set. The minimization of a function has been for many years, and still is, an active area of research and as a consequence numerous methods and routines [15] have been developed.

Optimization methods can be crudely divided into gradient and non-gradient based meth-

ods. The gradient-based methods are often (very) sophisticated offsprings of Newton's method. Examples of gradient-based methods are: CGFFT [17], [16], NPSOL (which is part of the NAG Fortran library, E04UFF), and L-BFGS-B [5]. Examples of non-gradient based methods are: Genetic Algorithms (GAs) [9], Particle Swarm Optimization [4], and the Minimax Optimization Method [18]. The gradient-based methods seem to be more efficient, when comparing the results of gradient- and non-gradient-based methods, but at the same time far less robust when it comes to finding a global optimum. A hybrid called: Genetic Algorithm Coupled with Sensitivity analysis (GACS) [11], employs the best of both worlds, i.e., a non-gradient-based method, viz., a Genetic Algorithm, is employed to obtain a starting point for a gradient-based method near a suspected global optimum. Subsequently, a gradient-based method, viz., the steepest-descent method is employed to converge efficiently to the optimum. Although this method seems to be ideal, a lot of fine tuning is required before the method's performance is maximized and a change in the optimization problem will probably mean re-tuning the method all over again. After considering the pros and cons the gradient-based methods were chosen, mainly because of their efficiency and the simple fact that finding a local optimum, which agrees with the constraints, is in a practical sense not less desirable. There are of course drawbacks. One of them is the fact that gradient-based methods can not handle the optimization of non-differentiable problems. The optimization of the patch shape is, in this case, a good example, because the shape is approximated by rectangular cells, see Section 4.4. Changing the patch shape means adding or removing one or more rectangular cells of metallization. The parameter that accounts for the presence and absence of rectangular cells is by definition non-differentiable. This problem can be circumvented by employing a different formulation of the problem, which will not be investigated in this report.

From a long list of gradient-based methods, NPSOL and L-BFGS-B were selected, simply because they were available at the Electromagnetics group at the University of Technology in Eindhoven. Both methods can handle a non-linear, but smooth objective function and (non-)linear constraints (L-BFGS-B can only handle linear constraints), which are based on quadratic programming [8]. As a consequence, these methods will perform well for quadratic problems. For most real life problems the objective function will not be quadratic, but if it is chosen carefully the method will converge more efficiently. Generally the following expression for the radiated power, P_{rad}, holds:

$$P_{\text{rad}} = \iint \boldsymbol{S}(\boldsymbol{r}) \cdot \boldsymbol{u}_r \, r^2 \, d\Omega \,, \tag{5.1}$$

where $\boldsymbol{S}$ denotes the Pointing vector and $d\Omega$ the solid angle. By employing the fact that the model will only radiate plane waves and by expressing the electric field in spherical components the following relation is established:

$$P_{\text{rad}} \sim |\boldsymbol{E}^s|^2 = |E^s_\theta|^2 + |E^s_\phi|^2 \,, \tag{5.2}$$

which shows that the power per radiated plane wave is proportional to the sum of the squares of the field components amplitudes. Multiple plane-wave solutions, i.e., grating

lobes, are in nearly all applications not desirable and therefore designs that give rise to them are avoided by choosing the design parameters such that Eq. (4.4) holds only for the $(0,0)$-mode. An appropriate normalization of the objective function can be achieved by considering the input power, i.e., the power radiated by the small electric dipoles situated underneath the patches. Note that maximizing the expression above equals minus one times the result of minimizing its negative, i.e.,

$$\max(P_{\text{rad}}) = -\min(-P_{\text{rad}})\,. \tag{5.3}$$

The final objective function for maximizing the output power equals:

$$\Psi = -|E_\theta^s|^2 - |E_\phi^s|^2\,, \tag{5.4}$$

which is plotted (normalized) as a function of $|E_\theta|$ and $|E_\phi|$ in Figure 5.1. The figure clearly shows a single optimum when the amplitudes of both parameters reach their maximum.

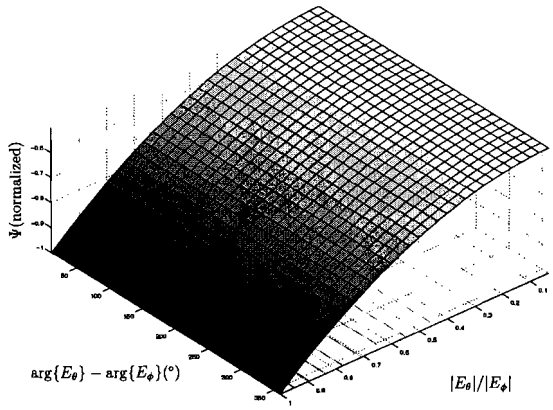

Figure 5.1: The normalized objective function, Ψ, for maximizing the radiated power as a function of $|E_\theta^s|$ and $|E_\phi^s|$, which shows a single optimum when both parameters are at their maximum.

The derivative of the objective function, Ψ, with respect to parameter, p_i, yields:

$$\partial_{p_i}\Psi = -2\Re\left[E_\theta^{s*}\partial_{p_i}E_\theta^s + E_\phi^{s*}\partial_{p_i}E_\phi^s\right]\,, \tag{5.5}$$

where * denotes complex conjugation. Note that this derivative still contains partial derivatives of E_θ^s and E_ϕ^s, which will be obtained in the next section.

The polarization of a plane wave is defined by the complex amplitudes of the θ- and ϕ-components. In general the field is elliptically polarized. Two special cases of elliptical polarization are identified as linear polarization and circular polarization. The linear

polarization case arises when the two components have an identical phase or one has an amplitude equal to zero. The circular polarization case indicates that the field components have a phase difference of exactly $+90°$ or $-90°$ and equal amplitudes. Both polarization cases are depicted in Figure 5.2. This report is restricted to the circular

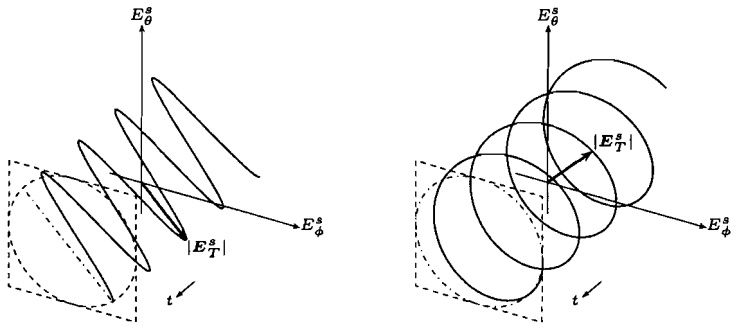

(a) (b)

Figure 5.2: Two types of polarization: (a) linear, where the field components have an equal phase, and (b) circular polarization, where the field components have a phase difference of 90° and equal amplitudes.

polarization case, because optimizing for horizontal or vertical polarization is not much of a challenge, when the horizontal probe position is considered as a design parameter as will be shown briefly in Section 5.3. In contrast, obtaining a suitable objective function for circular polarization proved to be a bit harder. The final expression for the objective function is

$$\Psi = \frac{\left|E_\theta^{s2} + E_\phi^{s2}\right|^2}{\left(|E_\theta^s|^2 + |E_\phi^s|^2\right)^2}, \tag{5.6}$$

which gives rise to two optima, one for each circular polarization case. The numerator of the objective function becomes zero when the two criteria, equal amplitudes and $\pm 90°$ phase difference, are met by employing the fact that the doubled angle of $\pm 90°$ results in a additional minus sign. The denominator simply normalizes the objective function. In Figure 5.3 the objective function is plotted as a function of the field components phase difference and the quotient of their amplitudes. Note that it combines the phase and amplitude constraints in such a manner that both constraints are on a more or less similar scale. Its derivative with respect to a parameter, p_i, yields,

$$\partial_{p_i}\Psi = 4\left\{ \frac{\Re\left[\left(E_\theta^{s2} + E_\phi^{s2}\right)^* \left(E_\theta^s \partial_{p_i} E_\theta^s + E_\phi^s \partial_{p_i} E_\phi^s\right)\right]}{\left(|E_\theta^s|^2 + |E_\phi^s|^2\right)^2} - \frac{\left|E_\theta^{s2} + E_\phi^{s2}\right|^2 \Re\left(E_\theta^{s*} \partial_{p_i} E_\theta^s + E_\phi^{s*} \partial_{p_i} E_\phi^s\right)}{\left(|E_\theta^s|^2 + |E_\phi^s|^2\right)^3} \right\} \tag{5.7}$$

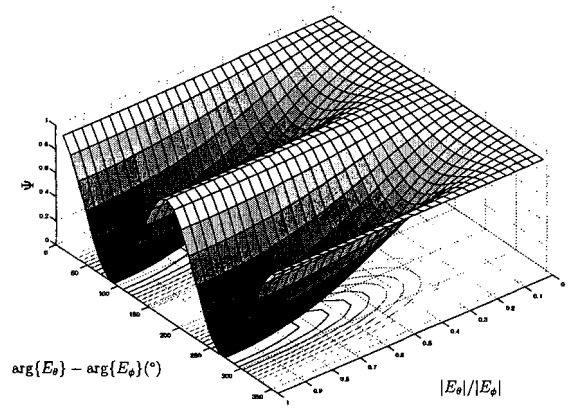

Figure 5.3: The objective function, Ψ, as function of the field components phase difference and the quotient of their amplitudes, which combines both circular polarization case, i.e, $\pm 90°$ phase difference.

Splitting up the two circular polarization cases, i.e., clockwise or counter-clockwise circular polarization gives rise to the following objective function,

$$\Psi = \frac{1}{2} \frac{\left|E_\theta^s \pm j\, E_\phi^s\right|^2}{|E_\theta^s|^2 + |E_\phi^s|^2}, \tag{5.8}$$

where the $\pm$ sign denotes each of the circular polarization cases. The objective function for one of the circular polarization cases is depicted in Figure 5.4, where the minimum of the function coincides with the optimum for one of the circular polarization cases. Its derivative with respect to a parameter, p_i, yields,

$$\begin{aligned} \partial_{p_i}\Psi = & \frac{\Re\left[\left(E_\theta^s \pm j\, E_\phi^s\right)^* \left(\partial_{p_i} E_\theta^s \pm j\, \partial_{p_i} E_\phi^s\right)\right]}{|E_\theta^s|^2 + |E_\phi^s|^2} - \\ & \frac{\left|E_\theta^s \pm j\, E_\phi^s\right|^2 \Re\left(E_\theta^{s*} \partial_{p_i} E_\theta^s + E_\phi^{s*} \partial_{p_i} E_\phi^s\right)}{\left(|E_\theta^s|^2 + |E_\phi^s|^2\right)^2} \end{aligned} \tag{5.9}$$

Note that both the objective functions and their derivatives for the circular polarization cases have a singularity for $|E_\theta^s| = |E_\phi^s| = 0$. This is in fact desirable, because optimal sets that result in small values of $|E_\theta^s|$ and $|E_\phi^s|$ will hardly radiate and will therefore have little practical use.

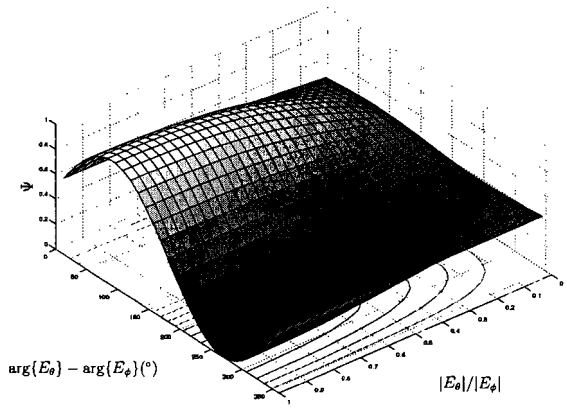

Figure 5.4: The objective function, Ψ, as function of the field components phase difference and the quotient of their amplitudes. Note that minimization of this function optimizes for a single circular polarization case.

5.2 Gradients and adjoint operators

The minimization methods, NPSOL and L-BFGS-B, which were selected in the previous section, require only an objective function and its gradient with respect to the design parameters $p_1, \ldots, p_n$, which are combined in a single vector $\boldsymbol{p}$. Note that NPSOL will also require the gradient of the non-linear constraints, if any are employed. The gradients as determined in the previous section contain derivatives of E_θ^s and E_ϕ^s with respect to the design parameters, which leaves the gradients still undetermined. In Chapter 4 expressions were derived for the scattered electric field, which shows that the scattered electric field can be written as a convolution of a Green's function with the current density on the patches plus the part of the electric field that was radiated directly by the source. As a consequence the scattered electric field, $\boldsymbol{E}^s$, in the direction, $\boldsymbol{u}_\ell$, can be expressed as an inner product of $\boldsymbol{J}_S$ and $\boldsymbol{g}_\ell$, which denotes the Green's function and the spatial derivatives acting on it, plus the directly radiated part $\boldsymbol{E}^s_{\text{source}}$, i.e.,

$$\boldsymbol{u}_\ell \cdot \boldsymbol{E}^s = (\boldsymbol{J}_S, \boldsymbol{g}_\ell) + E^s_{\text{source},\ell}\,, \tag{5.10}$$

where the subscript $_\ell$ denotes for instance the θ-direction. Note that $\boldsymbol{J}_S$, $\boldsymbol{g}_\ell$, and $E^s_{\text{source},\ell}$ are functions of the vector $\boldsymbol{p}$, and that $(\cdot,\cdot)$ denotes a complex inner product or more precisely the $L^2(\partial D)^2$ inner product, where ∂D denotes an area, which in this case, equals the plane $z = 0$ on which the patches reside. As a consequence of this formulation the result from [3, Section 5.1] can be applied instantly, which establishes an expression for the partial derivatives of E_θ^s and E_ϕ^s, with respect to a design parameter p_i by considering

the following two systems

$$L(\boldsymbol{p})\,\boldsymbol{J}_{\mathcal{S}} = \boldsymbol{f}(\boldsymbol{p})\,, \tag{5.11a}$$

$$L(\boldsymbol{p})^{a}\boldsymbol{v}_{\ell} = \boldsymbol{g}_{\ell}(\boldsymbol{p})\,, \tag{5.11b}$$

where $L(\boldsymbol{p})$ contains the Green's functions that relate the electromagnetic field to the currents on the patch, $L(\boldsymbol{p})^{a}$ denotes its adjoint with respect to $(\cdot,\cdot)$ and $\boldsymbol{f}(\boldsymbol{p})$ denotes the forcing vector, which is the discrete version of the forcing function. Subsequent employment of these systems yields:

$$\begin{aligned}\partial_{p_i}E^{s}_{\ell} = (\partial_{p_i}\boldsymbol{f}(\boldsymbol{p}) - [\partial_{p_i}L(\boldsymbol{p})]\boldsymbol{J}_{\mathcal{S}}(\boldsymbol{p}), \boldsymbol{v}_{\ell}(\boldsymbol{p})) + (\boldsymbol{J}_{\mathcal{S}}(\boldsymbol{p}), \partial_{p_i}\boldsymbol{g}_{\ell}(\boldsymbol{p})) + \\ \partial_{p_i}E^{s}_{\text{source},\ell}(\boldsymbol{p})\,,\end{aligned} \tag{5.12}$$

The real beauty of Eq. (5.12) lies in the fact that it takes, in total, only two matrix inversions to determine the vectors $\boldsymbol{v}_{\ell}$ and $\boldsymbol{J}_{\mathcal{S}}$, and they remain unchanged for each of the partial derivatives that construct the gradient with respect to $\boldsymbol{p}$. Consequently, only four matrix inversion are needed to determine $\nabla_{\boldsymbol{p}}E^{s}_{\theta}$ and $\nabla_{\boldsymbol{p}}E^{s}_{\phi}$.

However the result, i.e., Eq. (5.12), still contains a number of unknowns, viz., $\partial_{p_i}\boldsymbol{f}(\boldsymbol{p})$, $\partial_{p_i}L(\boldsymbol{p})$, and $\partial_{p_i}\boldsymbol{g}_{\ell}(\boldsymbol{p})$. These unknowns are composed of Green's functions and linear combinations of them, e.g., $\boldsymbol{f}(\boldsymbol{p})$ contains G_3 as defined in Chapter 3, which means that in the end the partial derivatives of the appropriate Green's functions are needed. It turns out that the partial derivatives of $\hat{G}_1$, $\hat{G}_2$ (as defined in Chapter 2), and $\hat{G}_3$ are the building blocks needed to construct the gradient of the objective function $\Psi(\boldsymbol{p})$. In this report x_0, y_0, z_0, ε_1 and d are considered as design parameters, where x_0 and y_0 denote the horizontal probe position, z_0 denotes the longitudinal position of the probe in layer one, which has a permittivity, ε_1, and thickness, d. Subsequently, linear constraints can be determined for each of the design parameters: $0 < x_0 < p$, $0 < y_0 < q$, $-d < z_0 < 0$, $\varepsilon_1 > \varepsilon_0$, and $d > 0$, which immediately points out a dependence between the parameters z_0 and d. This is easily solved by introducing a relative longitudinal probe position, α_z, which is related to z_0 by the following expression,

$$z_0 = -\alpha_z d\,. \tag{5.13}$$

This new design parameter will replace z_0 during optimization, which ensures that the longitudinal probe position does not violate its constraints when d is updated. The appropriate linear constraints are defined by: $0 < \alpha_z < 1$. Closer examination of $\hat{G}_1$, $\hat{G}_2$, and $\hat{G}_3$ reveals that $\hat{G}_1$ and $\hat{G}_2$ do not depend on the probe position and $\hat{G}_3$ does not depend on the horizontal probe position. This leaves the partial derivatives of $\hat{G}_1$, $\hat{G}_2$, and $\hat{G}_3$ with respect to ε_1 and d, and the partial derivative of $\hat{G}_3$ with respect to α_z to be determined. Consider the decomposition of $\hat{G}_1$ and $\hat{G}_2$,

$$\hat{G}_1 = \frac{1}{k_T^2}\left(\frac{N_A D_B - N_B D_A}{D_A D_B}\right)\,, \tag{5.14a}$$

$$\hat{G}_2 = \frac{N_B}{D_B}\,, \tag{5.14b}$$

where N denotes a numerator and D a denominator, the subscripts $_A$ and $_B$ indicate the two parts of $\hat{G}_1$. The decomposition of Eq. (5.15) clearly shows that finding a derivative for $\hat{G}_1$ creates the parts needed to construct the derivative of $\hat{G}_2$. For the derivative of $\hat{G}_3$ a similar decomposition is employed, i.e.,

$$\hat{G}_3 = N_E \frac{N_F}{D_F} N_G N_H \,. \tag{5.15}$$

The derivatives of $\hat{G}_1$, $\hat{G}_2$, and $\hat{G}_3$ are derived by employing the product and quotient rule for differentiating repeatedly. Subsequently, the partial derivatives of the individual parts $A, \ldots, H$ with respect to the appropriate parameters are obtained. These expressions are presented in Appendix B together with the test results. In the tests, the analytically determined derivative was plotted against its numerical counterpart as a function of k_T. Note that the numerically determined derivative employs a central differences scheme, with a fixed value for the step size, h.

5.3 Numerical results

This section is divided into two parts, where each of the parts presents the results belonging to one of the objectives, viz., maximization of the radiated power and optimization for circular polarization. Furthermore, all results presented in this section were generated while using the same infinite-array configuration, which is given in Table B.1. Any deviations from these values are presented together with the appropriate results.

Starting out with, which seemed the easiest problem, viz., optimizing the radiated power, both optimization routines, NPSOL and L-BFGS-B, were employed. The optimization of the radiated power is attempted for two different scan angles (θ, ϕ), viz., $(45°, 0°)$ and $(45°, 20°)$. The center of the patch is used as a initial horizontal probe position. Analysis of the results revealed that L-BFGS-B outperformed NPSOL, i.e., it required only 14 objective-function evaluations, where as NPSOL required 19. Both routines ended up in a global optimum near the upper right corner of the patch for both scan angles, as can be observed in Table 5.1a and Table 5.1b. The objective function, Ψ, is plotted for both scan angles as a function of the horizontal probe position, which are depicted in Figure 5.5a and Figure 5.5b. Note that the two plots show a very smooth objective function, with only a few optima, which contributes to a smooth convergence of the optimization. In Figure 5.6 the objective function, Ψ, is again plotted as a function of the horizontal probe position for the scan angle $(\theta = 45°, \phi = 0°)$, but now for two different infinite-array configurations, viz. $\varepsilon_1 = 3.5 \cdot \varepsilon_0$, $\alpha_z = 0.25$ and $\varepsilon_1 = 6 \cdot \varepsilon_0$, $\alpha_z = 0.25$. These results together with the previous ones suggest that the position of the optima remain near the corners of the patch for any design parameter variation other than the shape of the patch. This would indicate that the positions of the optima are related to that shape.

	$x_0^*(m)$	$y_0^*(m)$	Ψ	NF	Converged?
NPSOL	$9.311275 \cdot 10^{-3}$	$9.418367 \cdot 10^{-3}$	$-4.067650 \cdot 10^{6}$	19	Yes
L-BFGS-B	$9.311295 \cdot 10^{-3}$	$9.418364 \cdot 10^{-3}$	$-4.067650 \cdot 10^{6}$	14	Yes

(a)

	$x_0^*(m)$	$y_0^*(m)$	Ψ	NF	Converged?
NPSOL	$9.301638 \cdot 10^{-3}$	$9.403709 \cdot 10^{-3}$	$-7.129581 \cdot 10^{6}$	19	Yes
L-BFGS-B	$9.314299 \cdot 10^{-3}$	$9.378452 \cdot 10^{-3}$	$-7.133176 \cdot 10^{6}$	14	Yes

(b)

Table 5.1: The optimization results, while optimizing the radiated power for the scan angles(θ, ϕ): (a) $(45°, 0°)$ and (b) $(45°, 20°)$. Note that NF denotes the number of function evaluations.

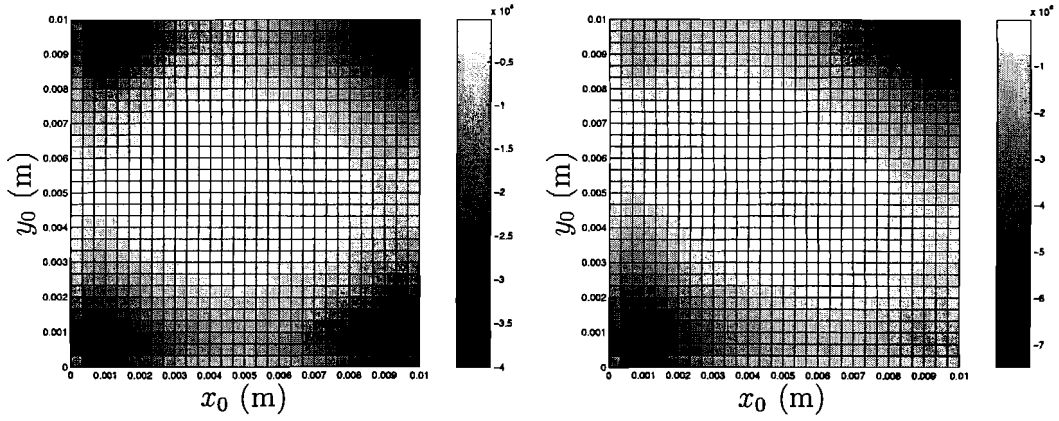

(a) (b)

Figure 5.5: The objective function for maximizing the radiated power plot as a function of the horizontal probe position for two different scan angles (θ, ϕ): (a) $(45°, 0°)$ and (b) $(45°, 20°)$.

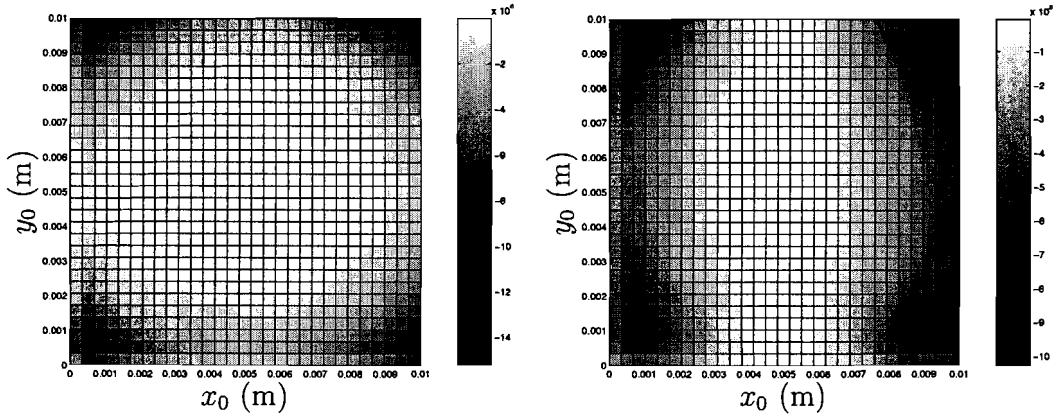

Figure 5.6: The objective function for maximizing the radiated power plot as a function of the horizontal probe position for the scan angle ($\theta = 45°, \phi = 0°$), but now for two different model configurations, viz.(a) $\varepsilon_1 = 3.5 \cdot \varepsilon_0$, $\alpha_z = 0.25$ and (b) $\varepsilon_1 = 6 \cdot \varepsilon_0$, $\alpha_z = 0.25$.

	$x^*(m)$	$y^*(m)$	Ψ	NF	Converged?
NPSOL	$4.630829 \cdot 10^{-3}$	$3.623427 \cdot 10^{-3}$	$8.460895 \cdot 10^{-13}$	21	Yes
L-BFGS-B	$7.027221 \cdot 10^{-3}$	$6.871566 \cdot 10^{-3}$	$2.004203 \cdot 10^{-12}$	6	Yes

Table 5.2: The optimization results, while optimizing for circular polarization for the scan angle ($\theta = 45°, \phi = 0°$), where ($x_0 = 6 \cdot 10^{-3}, y_0 = 6 \cdot 10^{-3}$) is chosen for the initial horizontal probe position. Note that NF denotes the number of function evaluations.

As mentioned earlier in Section 5.1 the optimization for linear polarization, i.e., especially horizontal or vertical polarization will not pose much of a challenge. This observation can be made by examination of the objective function as depicted in Figure 5.7, where the large dark area contains a single optimum near the center of the patch.

In a first attempt to optimize for circular polarization for a scan angle of ($\theta = 45°, \phi = 0°$), ($x_0 = 6 \cdot 10^{-3}, y_0 = 6 \cdot 10^{-3}$) is chosen for the initial horizontal probe position. Furthermore the objective function, which combines both clockwise and counter-clockwise circular polarization, is employed. As with the previous optimization case both search algorithms attempted to solve the optimization problem. The results are summarized in Table 5.3. Note that NPSOL seems to ignore any initial point given to it as depicted in Figure 5.8a for several different initial horizontal probe position, $(3 \cdot 10^{-3}, 8 \cdot 10^{-3})$, $(4 \cdot 10^{-3}, 4 \cdot 10^{-3})$, and $(6 \cdot 10^{-3}, 6 \cdot 10^{-3})$. Note also that NPSOL has found a global optimum, which can not be detected in the objective function plot due to the mesh size. From these results it is also clear that L-BFGS-B outperforms NPSOL with ease and grace, but the seemingly inability to influence the trajectory of NPSOL by choosing a different initial point

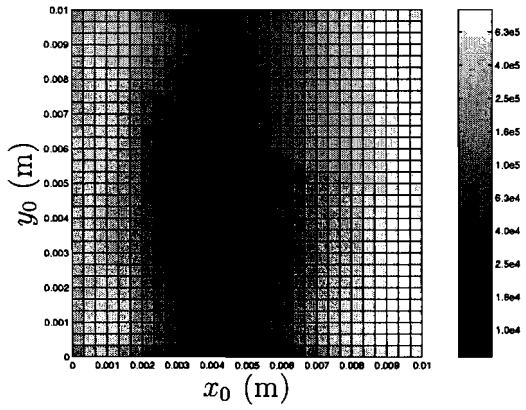

Figure 5.7: The objective function, $|E_\theta|^2$, as function of the horizontal probe position for horizontal polarization for a scan angle of $(\theta = 45°, \phi = 0°)$.

justifies the fact that it was abandoned for the remainder of this report.

Close examination of the objective function plot, as depicted in Figure 5.8a, shows the presence of several local optima. It also shows that the objective function has the same periodicity as the infinite-array model. By employing the periodicity the local optima at the constraints can be avoided as demonstrated by L-BFGS-B in Figure 5.8b, where a stationary point is reached after employing the periodicity of the objective function twice. Although the optimization eventually converged to a global optimum it did show some undesirable behavior after restarting the optimization in the point $(1 \cdot 10^{-2}, 2 \cdot 10^{-2})$. In a attempt to improve on this behavior the other objective function for circular polarization was employed, which distinguishes between clock and counter clockwise circular polarization, as given in Eq. (5.8). Note that the $+j$ variant is employed. This objective function is even smoother then the last one and as a consequence the convergence of the search algorithm will be improved. The results are depicted in Figure 5.9, which show a beautiful convergence of the L-BFGS-B method, which required only 25 objective function evaluations to do so. Note that this represents a very nice improvement when compared to the 40 objective function evaluations, which were required previously.

Although this objective function seems to improve the convergence rate of the search algorithm it does not seem to have any effect on the total number of local optima, which now seem to be divided amongst the clockwise and counter clockwise circular polarization cases. This can be illustrated by comparing Figure 5.8b with Figure 5.9 and Figure 5.10.

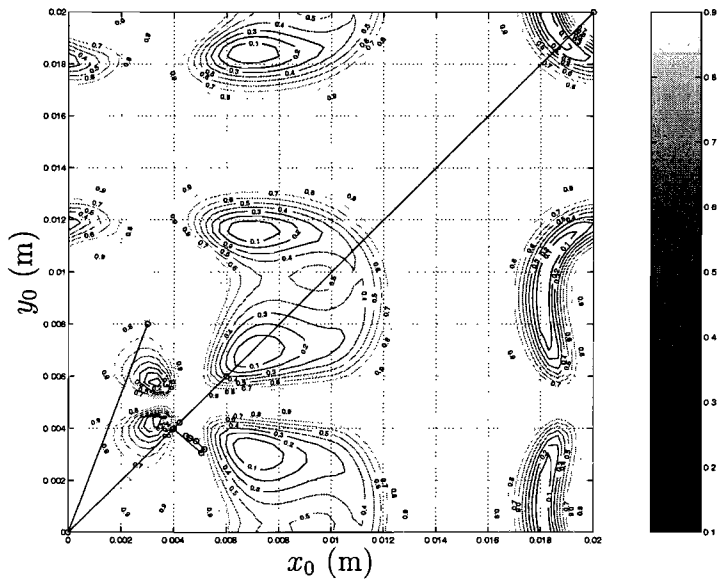

(a)

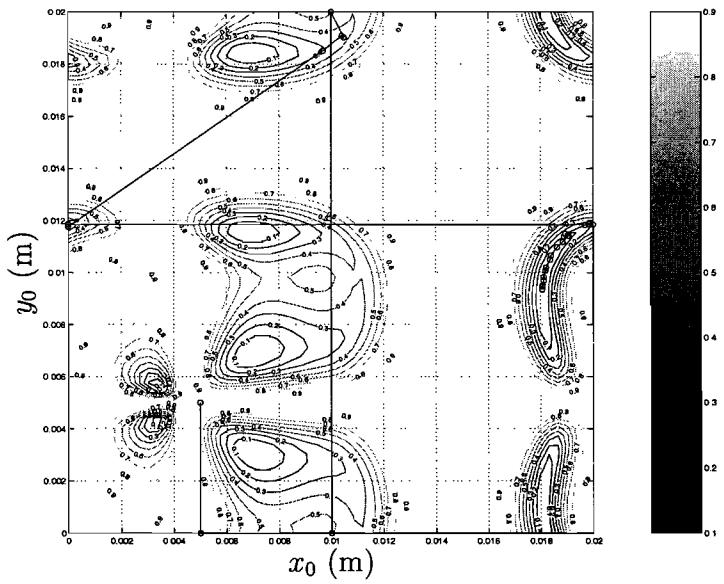

(b)

Figure 5.8: Trajectories followed by (a) the NPSOL method and (b) the L-BFGS-B method, while optimizing for circular polarization for a scan angle of $\theta = 45°, \phi = 0°$. In (a) three different initial points (x_0, y_0): $(3 \cdot 10^{-3}, 8 \cdot 10^{-3})$, $(4 \cdot 10^{-3}, 4 \cdot 10^{-3})$, and $(6 \cdot 10^{-3}, 6 \cdot 10^{-3})$ resulted in identical trajectories and the same stationary point $(4.630829 \cdot 10^{-3}, 3.623427 \cdot 10^{-3})$. In (b) only one initial point $(5 \cdot 10^{-3}, 5 \cdot 10^{-3})$ was considered and after 40 objective function evaluations and the employment of the periodicity of the objective function (twice) the stationary point $(1.806804 \cdot 10^{-2}, 9.347412 \cdot 10^{-3})$ was reached.

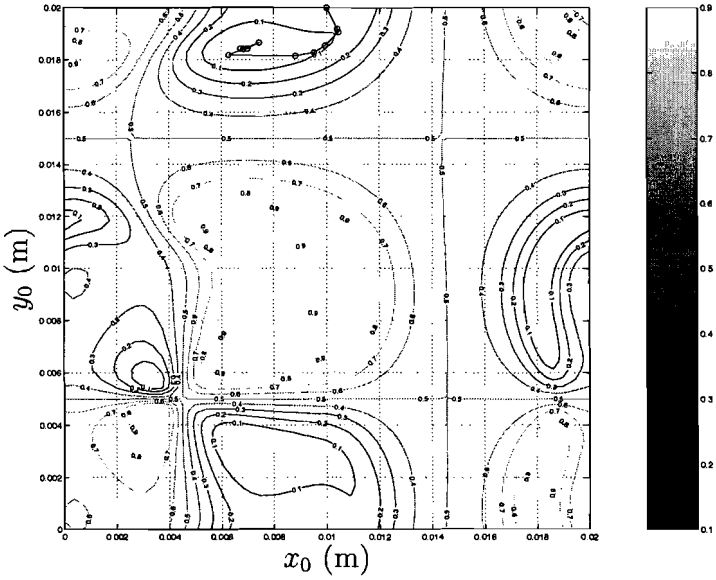

Figure 5.9: Trajectory followed by the L-BFGS-B method, while optimizing for circular polarization for a scan angle of $(\theta = 45°, \phi = 0°)$, where $(x_0 = 1 \cdot 10^{-2}, y_0 = 2 \cdot 10^{-2})$ is the initial point. Note that the objective function is the $+j$ variant of Eq. (5.8). After 25 objective function evaluations a stationary point was reached viz., $(6.857647 \cdot 10^{-3}, 1.841962 \cdot 10^{-2})$.

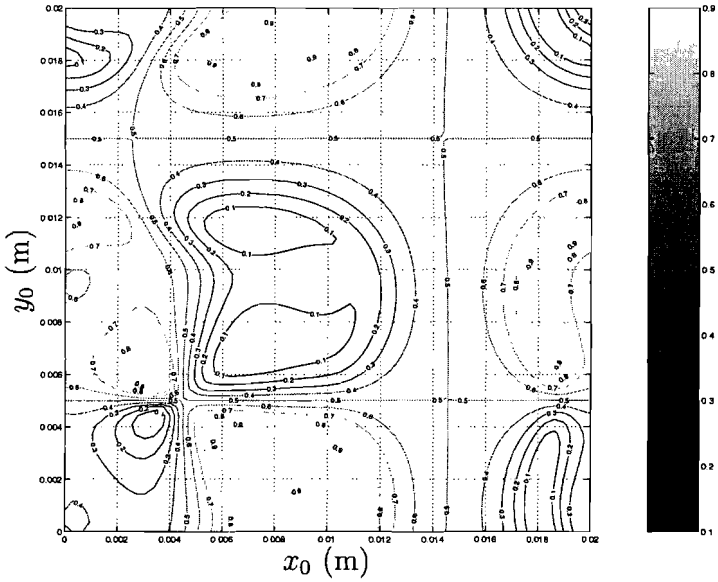

Figure 5.10: The objective function for optimization of circular polarization for a scan angle of $(\theta = 45°, \phi = 0°)$. Note that the objective function is the $-j$ variant of Eq. (5.8).

Chapter 6

Conclusions and Recommendations

In this report large uniform patch-antenna arrays on top of a layered medium are considered. The solution for the current distribution on the patches is obtained by solving the appropriate integral equation numerically, i.e., the application of the method of moments (MoM) in conjunction with CGFFT to solve the resulting system of equations. The fact that large arrays where considered, i.e., an array composing of a large number of patches, is exploited by employing an infinite-array model. However, the employment of the infinite-array model does have consequences, viz. it will neglect the edge effects, which are certain to arise in the real array. The combination of the infinite-array modeling, the employment of MoM and CGFFT gives rise to a efficient simulation tool.

Employing a transverse spatial Fourier transformation on a horizontally layered medium and subsequently expressing the equations in terms of its transverse field components gives rise to a set of second-order differential equations, which can be solved analytically.

The presence (or absence) of the layers beneath the first dielectric layer is accounted for by two reflection coefficients, one for each of the polarization contributions. They allow for a reconfigurable model in terms of the number of layers and their composition.

The subsequent employment of a conjugate gradient scheme based on the CGFFT algorithm reduces the computational load. The reduction is of such a degree that it enables the evaluation of the electromagnetic behavior of the antenna within a reasonable amount of time, while the calculations are performed on a by today's standard normal personal computer (see Table C.1).

In Section 4.4 the model is configured as a frequency-selective surface (FSS). The obtained reflection coefficients closely match the data obtained from [10]. This result increases the confidence that the model and the derivation of the far field expressions are indeed correct.

The optimization method requires the derivative of the employed objective function with respect to the considered design parameters, which are composed of linear and non-linear

combinations of several Green's functions. The derivatives of the Green's functions were derived and successfully tested by employing central differences, with a fixed step size h. It has to be noted that finding a step size, which results in a good approximation of the analytic results, requires some tuning.

The optimization results, when maximizing the radiated power, show that for a number of design-parameter variations the optima for the horizontal probe position remain near the corners of the patch. One possible explanation would be that these optima can be associated with a high input impedance. Subsequent excitation with ideal sources, i.e., a source without a volume or impedance, would result in a strong response of the system. This means that in reality those 'optima' might not radiate, because of the simple fact that the generator will be unable to deliver the power. Another possible explanation would be that the position of the optima are forced by the periodicity of the infinite-array model.

The optimization for circularly polarized plane waves already poses more of a challenge. The optimization process is suddenly troubled with many local optima, where there are nearly no local optima when maximizing the radiated power. This observation can already be made when considering only two parameters, which describe the horizontal probe position. For a more practical optimization problem, the number of design parameters shall be considerably larger. Consequently, the number of local optima shall increase as well. Due to the increase in irregularity of the problem, the number of time-consuming objective-function evaluations required to achieve convergence of the optimization process will increase, unless a better understanding of the underlying mechanisms is developed.

Finally, it can be observed that even for a relatively simple model, i.e., the infinite-array model, the average time needed to perform a optimization very soon becomes hours or even days, while a single objective function evaluation requires only a few minutes. Note that if the search algorithm does not strike gold the first time it will require the same amount of time over and over again until it does.

Upgrading the excitation model to a more realistically modeled source, which will have a finite volume, will allow the source to interact with the rest of the array and vice versa. An additional impedance constraint can then be included when maximizing the radiated power, which will result in design parameters with a more practical application.

The optimization objectives used in this report, viz., maximizing the radiated power and optimizing for circular polarization, were employed separately. However a realization of an antenna that does not radiate efficiently, but does have a nearly perfect circular polarization is in a practical sense meaningless. Trying to combine both objectives is therefore highly recommended. In addition, the optimization for bandwidth could be added for instance by exploiting its relation with the Q-factor [23].

Each design parameter that is added to the optimization process will generally increase

the number of iterations needed to let the optimization process converge and will require the construction of two additional matrices (see Section 5.2), which will have to be reconstructed for each iteration. Evidently, this will slow down the evaluation time and will dramatically increase the total time required to complete the optimization process. Speeding up the calculation time of the matrix elements is therefore recommended. This can be realized by employing the asymptotic behavior of the appropriate Green's functions [13] (and their derivatives) to remove the slowly converging parts of the infinite series that construct them. The slowly converging parts are then calculated separately and finally added to the result of the sped up infinite series. Decreasing the amount of time needed to evaluate the objective function and its derivatives will allow for even more design parameters to be added to the optimization process, while the total time required to complete the optimization remains reasonable. Examples of design parameters that could be added are, the periods p and q of the array the x- and y-direction, the thickness d of the dielectric layer, the length a, and width b of the unit-cell.

Appendix A

Auxiliary Equations and Formulas

A.1 Poisson summation formula

Let $\psi(\boldsymbol{r}_T)$ be a continuous function. Given the following Fourier series,

$$\psi\left(\boldsymbol{r}_T\right) = \sum_m \sum_n \Psi(m,n) \exp\left[-j\left(\frac{2\pi m}{p}\boldsymbol{u}_x + \frac{2\pi n}{q}\boldsymbol{u}_y\right)\cdot \boldsymbol{r}_T\right], \tag{A.1a}$$

$$\Psi(m,n) = \frac{1}{p\,q}\int_0^p \int_0^q \psi\left(\boldsymbol{r}_T\right) \exp\left[-j\left(\frac{2\pi m}{p}\boldsymbol{u}_x + \frac{2\pi n}{q}\boldsymbol{u}_y\right)\cdot \boldsymbol{r}_T\right] d\boldsymbol{r}_T\,, \tag{A.1b}$$

where $m, n \in \mathbb{Z}$, one can write:

$$\psi(\boldsymbol{r}_T) = \frac{1}{p\,q}\sum_m \sum_n \int_0^p \int_0^q \psi(\boldsymbol{r}'_T) \exp\left[j\left(\frac{2\pi m}{p}\boldsymbol{u}_x + \frac{2\pi n}{q}\boldsymbol{u}_y\right)\cdot (\boldsymbol{r}'_T - \boldsymbol{r}_T)\right] d\boldsymbol{r}'_T\,. \tag{A.2}$$

Applying the previous result to a new continuous function $\psi(\boldsymbol{r}_T + \boldsymbol{R}_{m',n'})$ yields,

$$\frac{1}{p\,q}\sum_m \sum_n \int_0^p \int_0^q \exp\left[j\left(\frac{2\pi m}{p}\boldsymbol{u}_x + \frac{2\pi n}{q}\boldsymbol{u}_y\right)\cdot (\boldsymbol{r}'_T - \boldsymbol{r}_T)\right] \times \psi(\boldsymbol{r}'_T + \boldsymbol{R}_{m',n'})\, d\boldsymbol{r}'_T = \psi(\boldsymbol{r}_T + \boldsymbol{R}_{m',n'}) \tag{A.3}$$

Shifting the integral over $\boldsymbol{R}_{m',n'}$ and employing the periodicity of the exponent yields,

$$\frac{1}{p\,q}\sum_m \sum_n \int_{pm'}^{p+pm'} \int_{qn'}^{q+qn'} \exp\left[j\left(\frac{2\pi m}{p}\boldsymbol{u}_x + \frac{2\pi n}{q}\boldsymbol{u}_y\right)\cdot (\boldsymbol{r}'_T - \boldsymbol{r}_T)\right] \times \psi(\boldsymbol{r}'_T)\, d\boldsymbol{r}'_T = \psi(\boldsymbol{r}_T + \boldsymbol{R}_{m',n'})\,. \tag{A.4}$$

Summing up all integral values for all (m', n'), where $m', n' \in \mathbb{Z}$, results in:

$$\frac{1}{p\,q}\sum_{m'}\sum_{n'}\sum_{m}\sum_{n}\int_{pm'}^{p+pm'}\int_{qn'}^{q+qn'}\exp\left[j\left(\frac{2\pi m}{p}\boldsymbol{u}_x+\frac{2\pi n}{q}\boldsymbol{u}_y\right)\cdot(\boldsymbol{r}'_T-\boldsymbol{r}_T)\right]\times \psi(\boldsymbol{r}'_T)\,d\boldsymbol{r}'_T=\sum_{m'}\sum_{n'}\psi(\boldsymbol{r}_T+\boldsymbol{R}_{m',n'})\,. \tag{A.5}$$

It is now possible to make use of the following property:

$$\sum_{m'}\sum_{n'}\int_{pm'}^{p+pm'}\int_{qn'}^{q+qn'}\cdots\,d\boldsymbol{r}'_T=\int_{-\infty}^{\infty}\int_{-\infty}^{\infty}\cdots\,d\boldsymbol{r}'_T\,. \tag{A.6}$$

By employing this property Eq. (A.5) reduces to,

$$\frac{1}{p\,q}\sum_{m}\sum_{n}\int_{-\infty}^{\infty}\int_{-\infty}^{\infty}\exp\left[j\left(\frac{2\pi m}{p}\boldsymbol{u}_x+\frac{2\pi n}{q}\boldsymbol{u}_y\right)\cdot(\boldsymbol{r}'_T-\boldsymbol{r}_T)\right]\psi(\boldsymbol{r}'_T)\,d\boldsymbol{r}'_T= \sum_{m'}\sum_{n'}\psi(\boldsymbol{r}_T+\boldsymbol{R}_{m',n'})\,. \tag{A.7}$$

Setting $\boldsymbol{r}_T=\boldsymbol{0}$ yields,

$$\frac{1}{p\,q}\sum_{m}\sum_{n}\int_{-\infty}^{\infty}\int_{-\infty}^{\infty}\exp\left[j\left(\frac{2\pi m}{p}\boldsymbol{u}_x+\frac{2\pi n}{q}\boldsymbol{u}_y\right)\cdot\boldsymbol{r}'_T\right]\psi(\boldsymbol{r}'_T)\,d\boldsymbol{r}'_T= \sum_{m'}\sum_{n'}\psi(\boldsymbol{R}_{m',n'})\,. \tag{A.8}$$

The double integral, $\int_{-\infty}^{\infty}\int_{-\infty}^{\infty}\cdots\,d\boldsymbol{r}'_T$, is easily identified as the sampled version of the Fourier transform, as previously defined in Eq. (2.2a). The substitution $\boldsymbol{k}_T=(2\pi m/p)\boldsymbol{u}_x+(2\pi n/q)\boldsymbol{u}_y$, where $m, n \in \mathbb{Z}$ samples the vector $\boldsymbol{k}_T$. Employing this knowledge reduces Eq. (A.8) to,

$$\frac{1}{p\,q}\sum_{m}\sum_{n}\hat{\Psi}\left(\frac{2\pi m}{p}\boldsymbol{u}_x+\frac{2\pi n}{q}\boldsymbol{u}_y\right)=\sum_{m'}\sum_{n'}\psi(\boldsymbol{R}_{m',n'})\,, \tag{A.9}$$

which concludes the derivation of the Poisson summation formula.

Appendix B

Green's Function Derivatives.

B.1 Derivatives of $\hat{G}_1$ and $\hat{G}_2$

Employing the same decomposition as presented earlier in Section 5.2, $\hat{G}_1$ and $\hat{G}_2$ can be written as:

$$\hat{G}_1 = \frac{1}{k_T^2}\left(\frac{N_A D_B - N_B D_A}{D_A D_B}\right), \tag{B.1a}$$

$$\hat{G}_2 = \frac{N_B}{D_B}, \tag{B.1b}$$

where N denotes a numerator and D a denominator, the subscripts $_A$ and $_B$ indicate the two parts, $A(k_T)$ and $B(k_T)$ of $\hat{G}_1$ as defined in Section 2.3. Consequently, the derivatives of both Green's functions with respect to ∂_{p_i} can be expressed as:

$$\partial_{p_i}\hat{G}_1 = \frac{1}{k_T^2}\left(\frac{D\,\partial_{p_i}N - N\,\partial_{p_i}D}{(D)^2}\right), \tag{B.2a}$$

$$\partial_{p_i}\hat{G}_2 = \frac{D_B\,\partial_{p_i}N_B - N_B\,\partial_{p_i}D_B}{(D_B)^2}, \tag{B.2b}$$

where

$$N = N_A D_B - N_B D_A, \tag{B.3a}$$

$$D = D_A D_B. \tag{B.3b}$$

For the derivatives of N and D the following expressions are obtained:

$$\partial_{p_i}N = D_B\,\partial_{p_i}N_A + N_A\,\partial_{p_i}D_B - (D_A\,\partial_{p_i}N_B + N_B\,\partial_{p_i}D_A), \tag{B.4a}$$

$$\partial_{p_i}D = D_B\,\partial_{p_i}D_A + D_A\,\partial_{p_i}D_B. \tag{B.4b}$$

The only unknowns left to be determined are: $\partial_{p_i}N_A$, $\partial_{p_i}N_B$, $\partial_{p_i}D_A$, and $\partial_{p_i}D_B$ with respect to ε_1 and d. For the derivatives with respect to ε_1 the following expression were

obtained:

$$\begin{aligned}\partial_{\varepsilon_1} N_A =& \frac{\gamma_0}{j\omega}\left\{(\partial_{\varepsilon_1}\gamma_1)\left[1+R^e_{1,2}\exp\left(-2\gamma_1 d\right)\right]+\right.\\ &\left.\gamma_1\left[(\partial_{\varepsilon_1}R^e_{1,2})\exp\left(-2\gamma_1 d\right)-2dR^e_{1,2}\exp\left(-2\gamma_1 d\right)\partial_{\varepsilon_1}\gamma 1\right]\right\}, \qquad \text{(B.5a)}\\ \partial_{\varepsilon_1} N_B =& j\omega\mu_0\mu_1\left[(\partial_{\varepsilon_1}R^h_{1,2})-2dR^h_{1,2}(\partial_{\varepsilon_1}\gamma_1)\right]\exp\left(-2\gamma_1 d\right), \qquad \text{(B.5b)}\end{aligned}$$

$$\begin{aligned}\partial_{\varepsilon_1} D_A =& \varepsilon_0(\partial_{\varepsilon_1}\gamma_1)\left[1+R^e_{1,2}\exp\left(-2\gamma_1 d\right)\right]+\\ &(\varepsilon_0\gamma_1-\varepsilon_1\gamma_0)\left[(\partial_{\varepsilon_1}R^e_{1,2})-2dR^e_{1,2}\left(\partial_{\varepsilon_1}\gamma_1\right)\right]\exp\left(-2\gamma_1 d\right)+\\ &\gamma_0\left[1-R^e_{1,2}\exp\left(-2\gamma_1 d\right)\right], \qquad \text{(B.5c)}\\ \partial_{\varepsilon_1} D_B =& \left[\mu_0+(2\gamma_1^2\mu_0-2\gamma_1\mu_1\mu_0-\mu_0)R^h_{1,2}\exp\left(-2\gamma_1 d\right)\right]\partial_{\varepsilon_1}\gamma_1+\\ &(\mu_1\gamma_0-\mu_0\gamma_1)(\partial_{\varepsilon_1}R^h_{1,2})\exp\left(-2\gamma 1 d\right). \qquad \text{(B.5d)}\end{aligned}$$

where $\partial_{\varepsilon_1}\gamma_1 = -\omega^2\mu_1/(2\gamma_1)$. This leaves the partial derivatives of $R^e_{1,2}$, $R^h_{1,2}$ with respect to ε_1 to be derived, which was achieved by employing the chain rule for derivatives, i.e.,

$$\partial_{\varepsilon_1} R^e_{1,2} = \frac{\partial R^e_{1,2}}{\partial\gamma_1}\frac{\partial\gamma_1}{\partial\varepsilon_1} = -\frac{\omega^2\mu_1}{2\gamma_1}\,\partial_{\gamma_1}R^e_{1,2}, \qquad \text{(B.6a)}$$

$$\partial_{\varepsilon_1} R^h_{1,2} = \frac{\partial R^h_{1,2}}{\partial\gamma_1}\frac{\partial\gamma_1}{\partial\varepsilon_1} = -\frac{\omega^2\mu_1}{2\gamma_1}\,\partial_{\gamma_1}R^h_{1,2}, \qquad \text{(B.6b)}$$

where the partial derivative of $R^e_{1,2}$, with respect to γ_1 is found by firstly expressing ε_1 in γ_1, defining a numerator and a denominator, obtaining their derivatives and subsequently construct $\partial_{\gamma_1}R^e_{1,2}$, i.e.,

$$R^e_{1,2} = \frac{\varepsilon_1\gamma_2-\varepsilon_2\gamma_1}{\varepsilon_1\gamma_2+\varepsilon_2\gamma_1} = \frac{k_T^2\gamma_2-\gamma_1^2\gamma_2-\gamma_1\omega^2\varepsilon_2\mu_1}{k_T^2\gamma_2-\gamma_1^2\gamma_2+\gamma_1\omega^2\varepsilon_2\mu_1} = \frac{N_{R^e_{1,2}}}{D_{R^e_{1,2}}} \Rightarrow$$

$$\partial_{\gamma_1}R^e_{1,2} = \frac{D_{R^e_{1,2}}\partial_{\gamma_1}N_{R^e_{1,2}} - N_{R^e_{1,2}}\partial_{\gamma_1}D_{R^e_{1,2}}}{\left(D_{R^e_{1,2}}\right)^2}, \text{where} \begin{cases}\partial_{\gamma_1}N_{R^e_{1,2}} = -2\gamma_1\gamma_2-\omega^2\varepsilon_2\mu_1\\ \partial_{\gamma_1}D_{R^e_{1,2}} = -2\gamma_1\gamma_2+\omega^2\varepsilon_2\mu_1\end{cases}. \qquad \text{(B.7)}$$

In a similar way the following expression was obtained for $\partial_{\gamma_1}R^h_{1,2}$:

$$\partial_{\gamma_1}R^h_{1,2} = \frac{2\mu_1\mu_2}{(\mu_2\gamma_1+\mu_1\gamma_2)^2}, \qquad \text{(B.8)}$$

which concludes the derivation of $\partial_{\varepsilon_1}\hat{G}_1$ and $\partial_{\varepsilon_1}\hat{G}_2$. For the derivatives with respect to d, the following expression were obtained:

$$\partial_d N_A = \frac{-2\gamma_1^2\gamma_0}{j\omega} R^e_{1,2} \exp\left(-2\gamma_1 d\right), \tag{B.9a}$$

$$\partial_d N_B = -2j\omega\gamma_1\mu_0\mu_1 R^h_{1,2} \exp\left(-2\gamma_1 d\right), \tag{B.9b}$$

$$\partial_d D_A = \left(-2\gamma_1^2\varepsilon_0 + 2\gamma_0\gamma_1\varepsilon_1\right) R^e_{1,2} \exp\left(-2\gamma_1 d\right), \tag{B.9c}$$

$$\partial_d D_B = \left(-2\gamma_0\gamma_1\mu_1 + 2\gamma_1^2\mu_0\right) R^h_{1,2} \exp\left(-2\gamma_1 d\right), \tag{B.9d}$$

which concludes the derivation of $\partial_d\hat{G}_1$ and $\partial_d\hat{G}_2$. All four derivatives were tested and the results are presented in the last section of this appendix.

B.2 Derivatives of $\hat{G}_3$

Employing the same decomposition as in Section 5.2, $\hat{G}_3$ is written as:

$$\hat{G}_3 = N_E \frac{N_F}{D_F} N_G N_H, \tag{B.10}$$

where N denotes a numerator or simply a part of the equation, which is multiplied with the rest, D denotes a denominator, the subscripts $_E$, $_F$, $_G$, and $_H$ denote the different parts of $\hat{G}_3$. For a derivative of $\hat{G}_3$ with respect to a parameter ∂_{p_i} it holds that,

$$\begin{aligned}\partial_{p_i}\hat{G}_3 = &\left(\partial_{p_i}N_E\right)\frac{N_F}{D_F} N_G N_H + N_E\frac{D_F\partial_{p_i}N_F - N_F\partial_{p_i}D_F}{\left(D_F\right)^2} N_G N_H + \\ &N_E\frac{N_F}{D_F}\left(\partial_{p_i}N_G\right)N_H + N_E\frac{N_F}{D_F} N_G\left(\partial_{p_i}N_H\right)\end{aligned} \tag{B.11}$$

For the derivative of $\hat{G}_3$ with respect to ε_1 the following expressions were obtained,

$$\partial_{\varepsilon_1}N_E = -\frac{1}{2\omega\varepsilon_1^2}, \tag{B.12a}$$

$$\partial_{\varepsilon_1}N_F = \left[\left(\partial_{\varepsilon_1}R^e_{1,2}\right) + R^e_{1,2}\frac{\omega^2(z_0+d)\mu_1}{\gamma_1}\right]\exp\left[-2\gamma_1(z_0+d)\right], \tag{B.12b}$$

$$\partial_{\varepsilon_1}D_F = \left[\left(\partial_{\varepsilon_1}R^e_{1,0}\right)R^e_{1,2} + R^e_{1,0}\left(\partial_{\varepsilon_1}R^e_{1,2}\right) + R^e_{1,0}R^e_{1,2}\frac{\omega^2\mu_1 d}{\gamma_1}\right]\exp\left(-2\gamma_1 d\right), \tag{B.12c}$$

$$\partial_{\varepsilon_1}N_G = \partial_{\varepsilon_1}R^e_{1,0}, \tag{B.12d}$$

$$\partial_{\varepsilon_1}N_H = \frac{\omega^2\mu_1 z_0}{2\gamma_1}\exp\left(\gamma_1 z_0\right). \tag{B.12e}$$

Note that the expression for $\partial_{\varepsilon_1}R^e_{1,2}$, which was obtained in the previous section is reused. For $\partial_{\varepsilon_1}R^e_{1,0}$ an expression is obtained by simply interchanging the subscript $_2$ with $_0$ in

Eq. (B.6a) and Eq. (B.7). Examination of $\hat{G}_3$ shows that only N_F and D_F have a dependence for d and as a consequence, the derivatives of N_E and N_G with respect to d are zero, i.e.,

$$\partial_d N_E = \partial_d N_G = 0\,, \tag{B.13a}$$

$$\partial_d N_F = -\,2\gamma_1\,(1-\alpha_z)\,R^e_{1,2}\exp\left[-2\gamma_1\,(1-\alpha_z)\,d\right], \tag{B.13b}$$

$$\partial_d D_F = -\,2\gamma_1 R^e_{1,0} R^e_{1,2}\exp\left(-2\gamma_1 d\right), \tag{B.13c}$$

$$\partial_d N_H = -\,\gamma_1\alpha_z\exp\left(-\gamma_1\alpha_z d\right), \tag{B.13d}$$

where the d-dependence of z_0 has been employed, viz., $z_0 = -\alpha_z d$, where α_z denotes the relative longitudinal probe position. For $\hat{G}_3$'s derivative with respect to α_z the following expressions were obtained,

$$\partial_{\alpha_z} N_E = \partial_{\alpha_z} D_F = \partial_{\alpha_z} N_G = 0\,, \tag{B.14a}$$

$$\partial_{\alpha_z} N_F = 2\gamma_1 d\, R^e_{1,2}\exp\left[-2\gamma_1(1-\alpha_z)d\right], \tag{B.14b}$$

$$\partial_{\alpha_z} N_H = -\,\gamma_1 d\exp\left(-\gamma_1\alpha_z d\right), \tag{B.14c}$$

which concludes the derivation of $\hat{G}_3$'s derivative with respect to the relative longitudinal probe position, α_z. All three derivatives of $\hat{G}_3$ were tested and the results are presented in the next section.

B.3 Numerical verification

All derivatives of the Green's functions, $\hat{G}_1$, $\hat{G}_2$, and $\hat{G}_3$ were tested against the results produced by a central difference scheme, with a fixed step size, h. The testing was performed separately for the real and imaginary part of the derivatives. The configuration of the patch-antenna array is given in Table B.1, while considering a square patch shape.

Parameter:	Value:	Description:
f	$8 \cdot 10^9$ Hz	The frequency.
p	$2 \cdot 10^{-2}$ m	The length of the unit cell in the x-direction.
q	$2 \cdot 10^{-2}$ m	The length of the unit cell in the y-direction.
a	$1 \cdot 10^{-2}$ m	The length of the patch in the x-direction.
b	$1 \cdot 10^{-2}$ m	The length of the patch in the y-direction.
d	$1 \cdot 10^{-3}$ m	The thickness of layer one.
$\varepsilon_{r,1}$	3.5	The relative permittivity of layer one.
$\mu_{r,1}$	1	The relative permeability of layer one.
$\varepsilon_{r,2}$	1	The relative permittivity of layer two.
$\mu_{r,2}$	1	The relative permeability of layer two.
$M_{\max}$	31	Maximum number of points in the x-direction.
$N_{\max}$	31	Maximum number of points in the y-direction.
x_0	$5 \cdot 10^{-3}$ m	The x-position of the probe.
y_0	$5 \cdot 10^{-3}$ m	The y-position of the probe.
α_z	$5 \cdot 10^{-1}$	The relative longitudinal probe position, $z_0 = -\alpha_z d$, where $0 < \alpha_z < 1$.
$I_z l$	$1 \cdot 10^{-3}$ Am	The product of the current amplitude and fictitious length of the probe.
θ^{sc}	45°	The θ of the scan angle.
ϕ^{sc}	0°	The ϕ of the scan angle.
err	$1 \cdot 10^{-7}$	The maximum allowed relative error for the CGFFT routine.

Table B.1: The patch antenna array configuration.

The test results are found on the following pages, where they show generally a good agreement when comparing the analytical and appropriate numerical obtained derivatives. The used step size, h, is given in the figure caption. Note that the comparison between analytical and numerical results is made on the left and the relative error is depicted on the right.

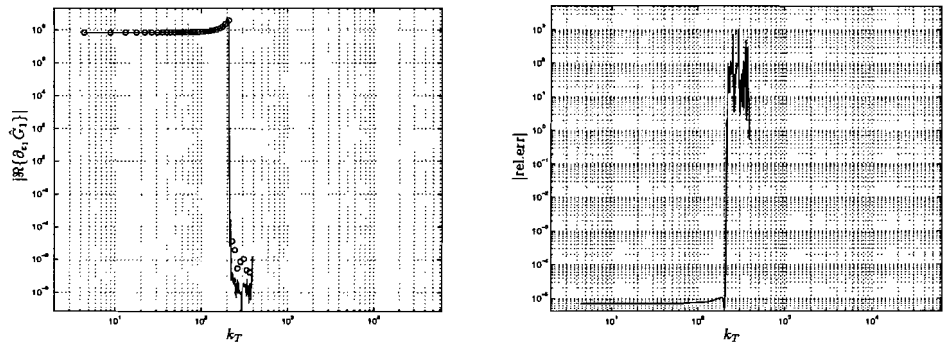

(a) (b)

Figure B.1: A comparison between analytically and numerically evaluated real part of the derivative of G_1 with respect to ε_1 is shown in (a) where both are plotted as a function of k_T. The solid line denotes the analytical results and the open bullets (o) denote the numerical results. The relative error is depicted in (b), again as a function of k_T. Note that a central difference scheme with a fixed step size, $h = 10^{-2}$, was used to produce the numerical results.

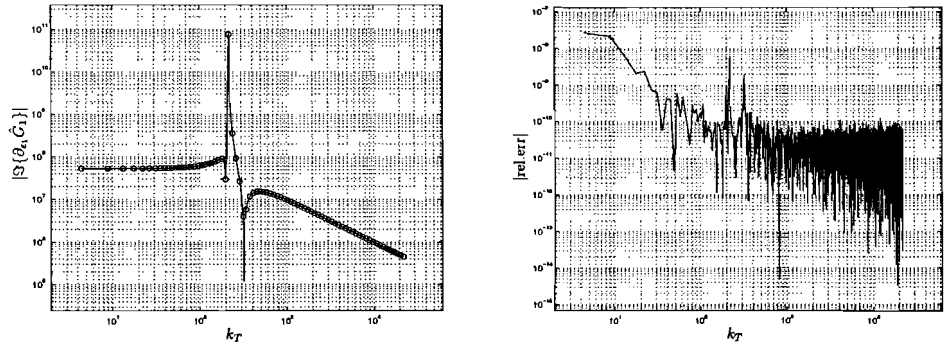

(a) (b)

Figure B.2: A comparison between analytically and numerically evaluated imaginary part of the derivative of G_1 with respect to ε_1 is shown in (a) where both are plotted as a function of k_T. The solid line denotes the analytical results and the open bullets (o) denote the numerical results. The relative error is depicted in (b), again as a function of k_T. Note that a central difference scheme with a fixed step size, $h = 10^{-5}$, was used to produce the numerical results.

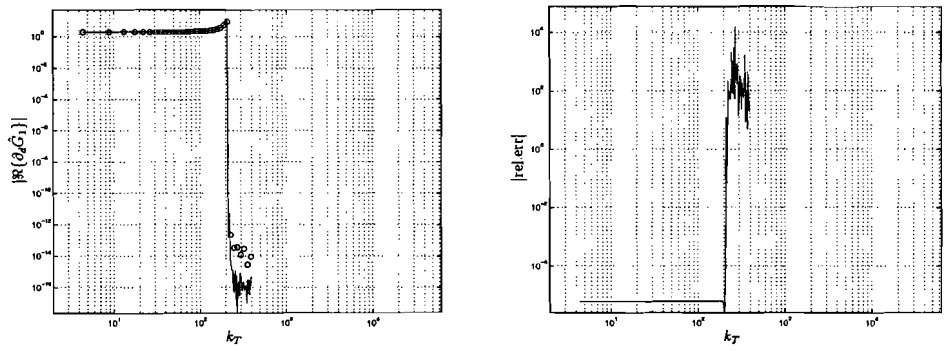

(a) (b)

Figure B.3: A comparison between analytically and numerically evaluated real part of the derivative of G_1 with respect to d is shown in (a) where both are plotted as a function of k_T. The solid line denotes the analytical results and the open bullets (o) denote the numerical results. The relative error is depicted in (b), again as a function of k_T. Note that a central difference scheme with a fixed step size, $h = 10^{-2}$, was used to produce the numerical results.

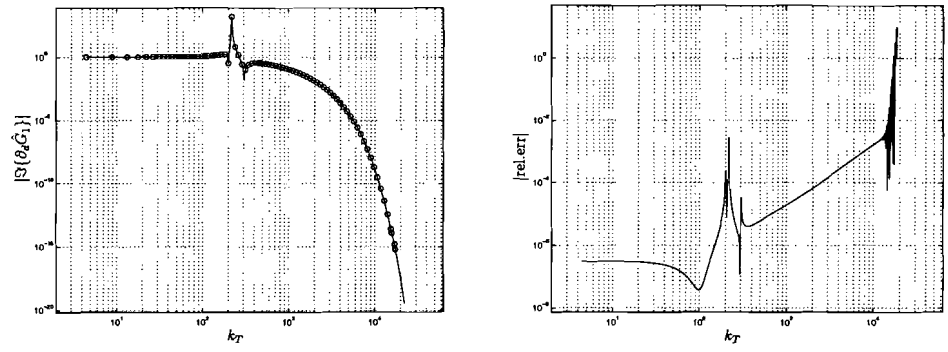

(a) (b)

Figure B.4: A comparison between analytically and numerically evaluated imaginary part of the derivative of G_1 with respect to d is shown in (a) where both are plotted as a function of k_T. The solid line denotes the analytical results and the open bullets (o) denote the numerical results. The relative error is depicted in (b), again as a function of k_T. Note that a central difference scheme with a fixed step size, $h = 10^{-2}$, was used to produce the numerical results.

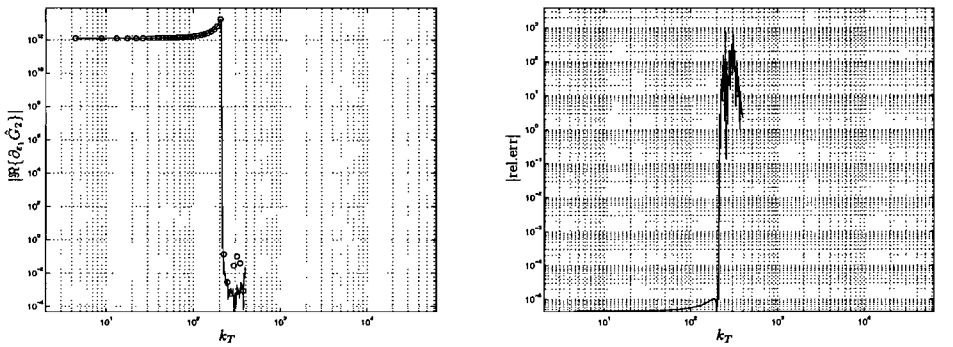

(a) (b)

Figure B.5: A comparison between analytically and numerically evaluated real part of the derivative of G_2 with respect to ε_1 is shown in (a) where both are plotted as a function of k_T. The solid line denotes the analytical results and the open bullets (o) denote the numerical results. The relative error is depicted in (b), again as a function of k_T. Note that a central difference scheme with a fixed step size, $h = 10^{-2}$, was used to produce the numerical results.

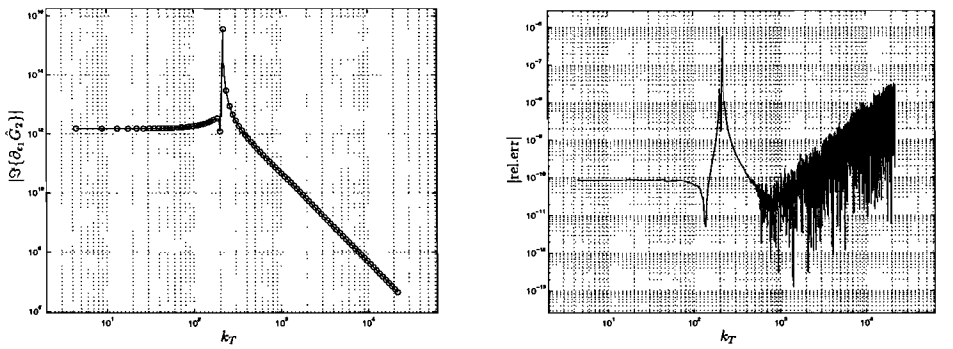

(a) (b)

Figure B.6: A comparison between analytically and numerically evaluated imaginary part of the derivative of G_2 with respect to ε_1 is shown in (a) where both are plotted as a function of k_T. The solid line denotes the analytical results and the open bullets (o) denote the numerical results. The relative error is depicted in (b), again as a function of k_T. Note that a central difference scheme with a fixed step size, $h = 10^{-4}$, was used to produce the numerical results.

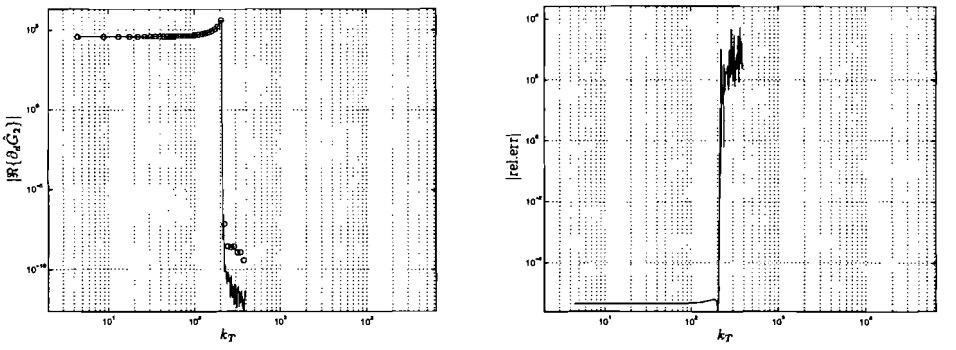

(a) (b)

Figure B.7: A comparison between analytically and numerically evaluated real part of the derivative of G_2 with respect to d is shown in (a) where both are plotted as a function of k_T. The solid line denotes the analytical results and the open bullets (o) denote the numerical results. The relative error is depicted in (b), again as a function of k_T. Note that a central difference scheme with a fixed step size, $h = 10^{-2}$, was used to produce the numerical results.

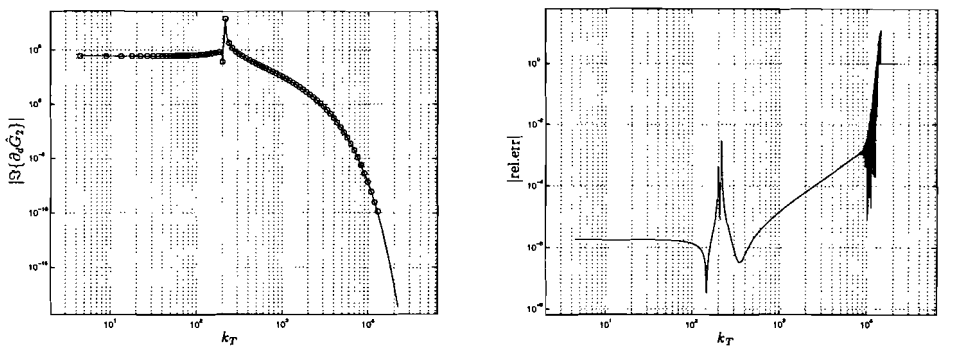

(a) (b)

Figure B.8: A comparison between analytically and numerically evaluated imaginary part of the derivative of G_2 with respect to d is shown in (a) where both are plotted as a function of k_T. The solid line denotes the analytical results and the open bullets (o) denote the numerical results. The relative error is depicted in (b), again as a function of k_T. Note that a central difference scheme with a fixed step size, $h = 10^{-2}$, was used to produce the numerical results.

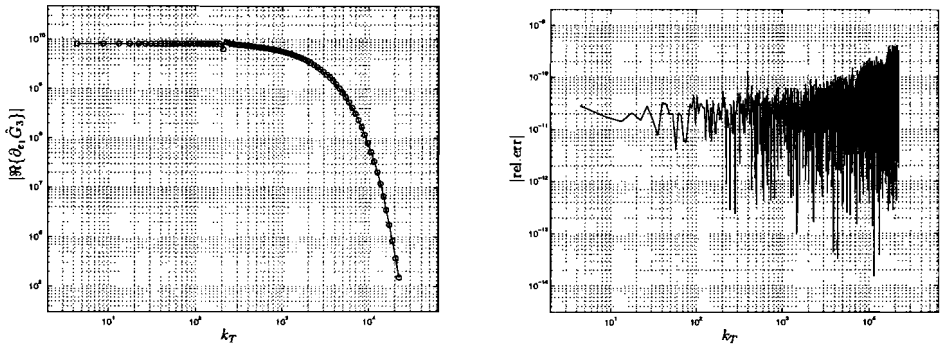

(a) (b)

Figure B.9: A comparison between analytically and numerically evaluated real part of the derivative of G_3 with respect to ε_1 is shown in (a) where both are plotted as a function of k_T. The solid line denotes the analytical results and the open bullets (o) denote the numerical results. The relative error is depicted in (b), again as a function of k_T. Note that a central difference scheme with a fixed step size, $h = 10^{-5}$, was used to produce the numerical results.

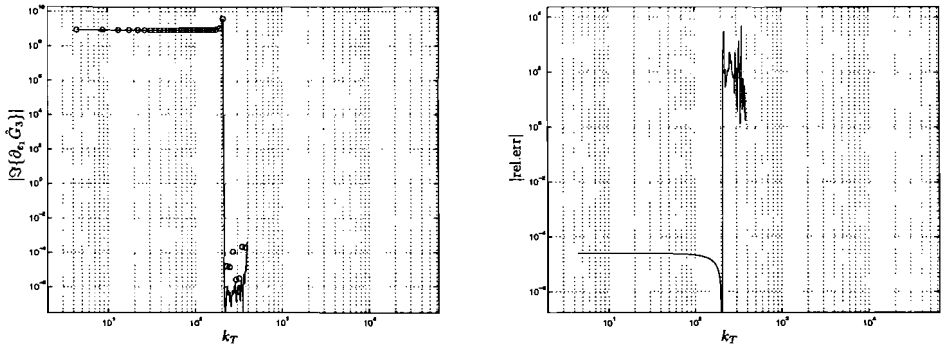

(a) (b)

Figure B.10: A comparison between analytically and numerically evaluated imaginary part of the derivative of G_3 with respect to ε_1 is shown in (a) where both are plotted as a function of k_T. The solid line denotes the analytical results and the open bullets (o) denote the numerical results. The relative error is depicted in (b), again as a function of k_T. Note that a central difference scheme with a fixed step size, $h = 10^{-2}$, was used to produce the numerical results.

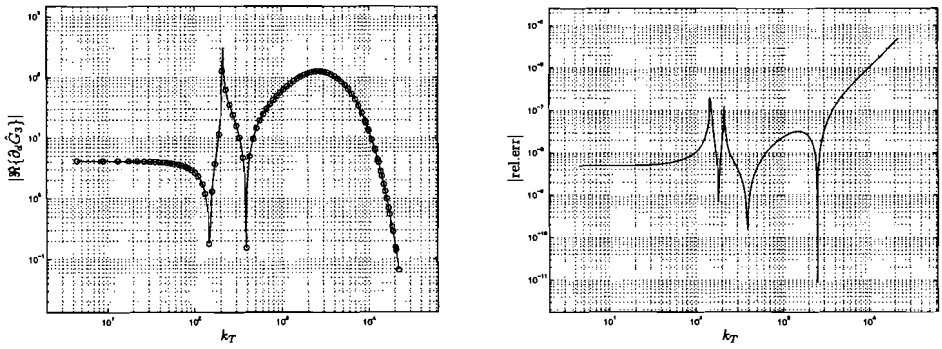

(a) (b)

Figure B.11: A comparison between analytically and numerically evaluated real part of the derivative of G_3 with respect to d is shown in (a) where both are plotted as a function of k_T. The solid line denotes the analytical results and the open bullets (o) denote the numerical results. The relative error is depicted in (b), again as a function of k_T. Note that a central difference scheme with a fixed step size, $h = 10^{-3}$, was used to produce the numerical results.

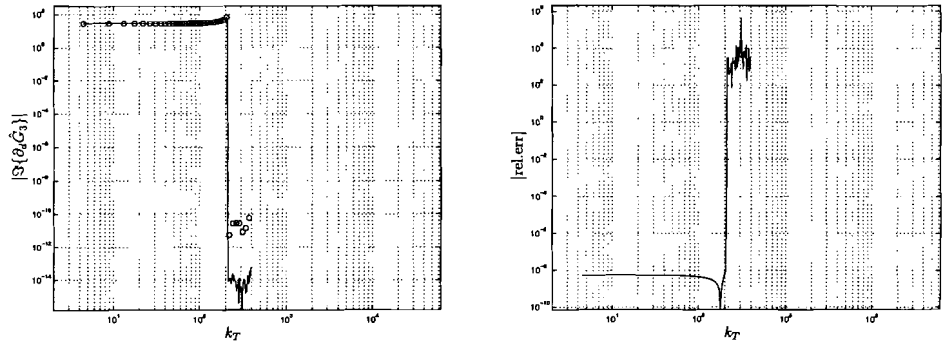

(a) (b)

Figure B.12: A comparison between analytically and numerically evaluated imaginary part of the derivative of G_3 with respect to d is shown in (a) where both are plotted as a function of k_T. The solid line denotes the analytical results and the open bullets (o) denote the numerical results. The relative error is depicted in (b), again as a function of k_T. Note that a central difference scheme with a fixed step size, $h = 10^{-5}$, was used to produce the numerical results.

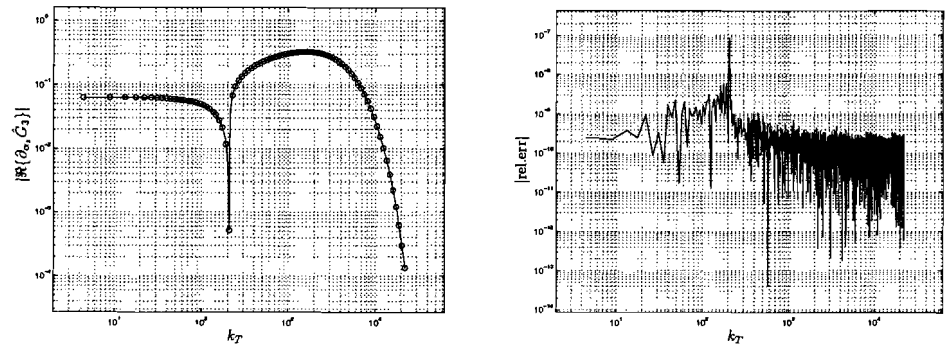

(a) (b)

Figure B.13: A comparison between analytically and numerically evaluated real part of the derivative of G_3 with respect to α_z is shown in (a) where both are plotted as a function of k_T. The solid line denotes the analytical results and the open bullets (o) denote the numerical results. The relative error is depicted in (b), again as a function of k_T. Note that a central difference scheme with a fixed step size, $h = 10^{-5}$, was used to produce the numerical results.

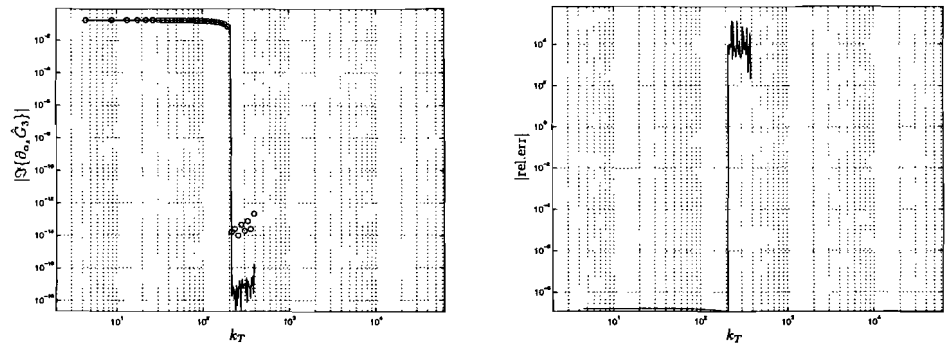

(a) (b)

Figure B.14: A comparison between analytically and numerically evaluated imaginary part of the derivative of G_3 with respect to α_z is shown in (a) where both are plotted as a function of k_T. The solid line denotes the analytical results and the open bullets (o) denote the numerical results. The relative error is depicted in (b), again as a function of k_T. Note that a central difference scheme with a fixed step size, $h = 10^{-3}$, was used to produce the numerical results.

Appendix C

A by today's standard normal PC

C.1 Configuration

Component:	Description:
CPU	AMD Athlon(tm) 64 3200+, 2.2GHz
Internal memory	512MB RAM
Harddisk	Western Digital 120GB, SATA Drive, Max. data transfer 602Mbits/s, Nominal RPM 7200, 8MB Buffer, single NTFS partition
Floppy drive	1.44MB, 3.5 inch
Optical Drive(s)	DVD-ROM: DVD 16x, CD 48x, E-IDE CD-RW: 52x/32x/52x, E-IDE

(a)

Software package:	Description:
Operating System	Microsoft Windows XP, SP2
Compiler	Salford Fortran 95 compiler
Development Environment	Plato 2 IDE
Software Library	NAG Mark 20

(b)

Table C.1: The hardware/software configuration of the personal computer that was used to generate the results presented in this report.

Bibliography

[1] N.W. Ashcroft and N.D. Mermin. *Solid State Physics.* Holt Rinehart and Winston, New York, 1976.

[2] D.J. Bekers. *Finite Antenna arrays: an eigencurrent approach.* PhD thesis, Eindhoven University of Technology, December 2004.

[3] M.C. van Beurden. *Integro-differential equations for electromagnetic scattering.* PhD thesis, Eindhoven University of Technology, September 2003.

[4] D.W. Boeringer and D.H. Werner. Particle swarm optimization versus genetic algorithms for phased array synthesis. *IEEE Transactions on Antennas and Propagation*, 52(3):771–779, May 2004.

[5] P. Lu C. Zhu, R.H. Byrd and J. Nocedal. Algorithm 778: L-BFGS-B: Fortran subroutines for large-scale bound-constrained optimization. *ACM Transactions on Mathematical Software*, 23(4):550–560, December 1997.

[6] Kyung K. Choi E.J. Haug and V. Komkov. *Design Sensitivity Analysis of Structural Systems*, volume 177 of *Mathematics in Science and Engineering.* Academic Press, Inc. (London) Ltd., 24-28 Oval Road, London NW1 7DX, 1986.

[7] N. Engheta, W.D. Murphy, V. Rokhlin, and M.S. Vassiliou. The fast multipole method (FMM) for electromagnetic scattering problems. *IEEE Transactions on Antennas and Propagation*, 40(6):634–641, June 1992.

[8] R. Fletcher. *Practical Methods of Optimization.* A Wiley - Interscience publication. John Wiley & Sons Ltd., second edition edition, 1987.

[9] R.L. Haupt. An introduction to genetic algorithms for electromagnetics. *IEEE Antennas and Propagation Magazine*, 37(2):7–15, April 1995.

[10] J.M. Jin and J.L. Volakis. Electromagnetic scattering by a perfectly conducting patch array on a dielectric slab. *IEEE Transactions on Antennas and Propagation*, 38(4):556–563, April 1990.

[11] Hong-bae Lee Hyun Kyo Jung Kim, Juno and Song yop Hahn. Optimal design technique for waveguide device. *IEEE Transactions on Magnetics*, 32(3):1250–1253, May 1996.

[12] D.Y.K. Ko and J.R. Sambles. Scattering matrix method for propagation of radiation in stratified media: attenuated total reflection studies of liquid crystals. *Journal of the Optical Society of America A Optics and Image Science*, 5(11):1863–1866, November 1988.

[13] B.J. Morsink. *Fast modeling of electromagnetic fields for the design of phased array antennas in radar systems.* PhD thesis, Eindhoven University of Technology, October 2005.

[14] R. Redheffer. On the relation of transmission-line theory to scattering and transfer. *Journal of Mathematics and Physics*, 41:1–14, 1962.

[15] S. Russenschuck. Techniques and applications of mathematical optimization and synthesis. *IEE Colloquium on 'Optimisation and Synthesis of Electromagnetic Fields'*, (1994/212), November 1994.

[16] T.K. Sarkar. *Application of Conjugate Gradient Method to Electromagnetics and Signal Analysis.* Number 5 in PIER, Progress in Electromagnetics Research. Elsevier, 1991.

[17] T.K. Sarkar, E. Arvas, and S.M. Rao. Application of the fast fourier transform and the conjugate gradient method for efficient solution of electromagnetic scattering from both electrically large and small conducting bodies. *Electromagnetics*, 5(2-3): 99–122, 1985.

[18] H. Schjaer-Jocobsen and K. Madsen. Synthesis of nonuniformly spaced arrays using a general nonlinear minimax optimization method. *IEEE Transactions on Antennas and Propagation*, pages 501–506, 1976.

[19] A.B. Smolders. *Microstrip Phased-Array Antennas: A Finite-Array Approach.* PhD thesis, Eindhoven University of Technology, 1984.

[20] A.B. Smolders. Elektromagnetische antennes. Lecture notes for the course: Electromagnetic waves and antennas, Eindhoven University of Technology, February 2000.

[21] A.G. Tijhuis. Plane-wave excitation of two-dimensionally periodic metallized structures in plane-stratified dielectric media. Technical report, Eindhoven University of Technology, January 2002. report of study contract for Thales Naval Nederland B.V.

[22] A.G. Tijhuis and A. Rubio Bretones. Transcient excitation of a layered dielectric medium by a pulsed electric dipole: spectral constituents. *EUROEM*, May 2000.

[23] A.D. Yaghjian and S.R. Best. Impedance, bandwidth, and Q of antennas. *IEEE Transactions on Antennas and Propagation*, 53(4):1298–1324, April 2005.